NUMERICAL SIMULATION OF CHARRING ABLATION COUPLED WITH COMPUTATIONAL FLUID DYNAMICS

A THESIS SUBMITTED TO
THE GRADUATE SCHOOL OF NATURAL AND APPLIED SCIENCES
OF
MIDDLE EAST TECHNICAL UNIVERSITY

BY

ÇETIN OZAN ALANYALIOĞLU

IN PARTIAL FULFILLMENT OF THE REQUIREMENTS
FOR
THE DEGREE OF MASTER OF SCIENCE
IN
AEROSPACE ENGINEERING

MAY 2019

Approval of the thesis:

NUMERICAL SIMULATION OF CHARRING ABLATION COUPLED WITH COMPUTATIONAL FLUID DYNAMICS

submitted by **ÇETIN OZAN ALANYALIOĞLU** in partial fulfillment of the requirements for the degree of **Master of Science in Aerospace Engineering Department, Middle East Technical University** by,

Prof. Dr. Halil Kalıpçılar
Dean, Graduate School of **Natural and Applied Sciences** _____

Prof. Dr. İsmail Hakkı Tuncer
Head of Department, **Aerospace Engineering** _____

Prof. Dr. Yusuf Özyörük
Supervisor, **Aerospace Engineering, METU** _____

Examining Committee Members:

Prof. Dr. İsmail Hakkı TUNCER
Aerospace Engineering, METU _____

Prof. Dr. Yusuf ÖZYÖRÜK
Aerospace Engineering, METU _____

Assoc. Prof. Dr. Sinan EYİ
Aerospace Engineering, METU _____

Assist. Prof. Dr. Sıtkı USLU
Mechanical Engineering, TOBB ETÜ _____

Assist. Prof. Dr. Mustafa KAYA
Aerospace Engineering, AYBU _____

Date:

I hereby declare that all information in this document has been obtained and presented in accordance with academic rules and ethical conduct. I also declare that, as required by these rules and conduct, I have fully cited and referenced all material and results that are not original to this work.

Name, Surname: Çetin Ozan Alanyalıoğlu

Signature :

ABSTRACT

NUMERICAL SIMULATION OF CHARRING ABLATION COUPLED WITH COMPUTATIONAL FLUID DYNAMICS

Alanyalıoğlu, Çetin Ozan
M.S., Department of Aerospace Engineering
Supervisor: Prof. Dr. Yusuf Özyörük

May 2019, 129 pages

Usage of charring ablators as nozzle liners is a common practice in the field of solid rocket motor industry. Among them, silica-phenolic is a commonly employed material due to its excellent insulation capability. During the design of a solid propellant rocket motor employing silica-phenolic as a nozzle liner, it is desired to have an accurate thermal analysis along with throat recession rate estimation, as the interior ballistics of a solid rocket motor is tightly coupled with throat diameter.

This work presents two tools with different levels of fidelity to fulfill these requirements. A one-dimensional tool named as KAYMAK is developed to perform in-depth analysis involving decomposition reactions and pyrolysis gas effects.A built-in simple interior ballistics solver is also included in KAYMAK to serve as a rapid computational tool during earlier phases of design. The governing equations for melting ablation surface energy balance, in-depth charring and pyrolysis flow and injection are implemented in commercial CFD solver FLUENT along with a boundary condition coupled to interior ballistics analysis to perform conjugate, transient analysis of charring ablation for axisymmetrical geometries. A new boundary condition for

inclusion of blowing with source terms has been introduced and validated against analytical results, and shape-change instability found in coupled ablation simulations is studied. Turbulence models used in nozzle heat transfer analysis are examined and compared against commonly used Bartz correlation for nozzle heat transfer.

Validation of KAYMAK is performed with available data found in literature, and FLUENT implementation is verified against results obtained with KAYMAK. A static firing has been conducted with a small scale motor employing a silica-phenolic nozzle insert and results are compared against interior ballistics coupled conjugate analysis performed with FLUENT implementation. Although a large uncertainty is present with the material characterization, promising results are obtained showing that all relevant physics are effectively captured, and it is illustrated that these effects cannot be captured with a lower fidelity analysis done with KAYMAK.

Keywords: ablation, charring, charring ablation, nozzle, solid rocket motor, conjugate analysis, silica-phenolic, interior ballistics

ÖZ

KÖMÜRLEŞEREK AŞINAN YALITIM MALZEMELERİNİN HESAPLAMALI AKIŞKANLAR DİNAMİĞİ İLE EŞZAMANLI NÜMERİK ANALİZİ

Alanyalıoğlu, Çetin Ozan
Yüksek Lisans, Havacılık ve Uzay Mühendisliği Bölümü
Tez Yöneticisi: Prof. Dr. Yusuf Özyörük

Mayıs 2019 , 129 sayfa

Kömürleşerek aşınan yalıtım malzemelerinin lüle yalıtımı olarak kullanılması katı yakıtlı roket motoru endüstrisinde oldukça yaygındır. Bunlar içerisinde, silika-fenolik malzeme sahip olduğu yüksek yalıtım kabiliyeti nedeniyle sıklıkla tercih edilmektedir. Silika-fenolik lüle yalıtımına sahip bir katı yakıtlı roket motorunun tasarım sürecinde, yüksek doğruluklu bir ısıl analiz ve katı yakıtlı roket motoru iç balistiği ile doğrudan ilgili olan lüle boğazı aşınmasına dair verinin mevcudiyeti önemlidir.

Bunların elde edilmesine yönelik olarak bu çalışmada farklı doğruluk seviyelerine sahip iki adet hesaplama aracı geliştirilmiştir. Bunlardan ilki KAYMAK adında bir boyutlu bir analiz aracı olup, malzeme içerisinde meydana gelen kömürleşme reaksiyonlarını ve reaksiyon ürünü gazların etkilerini incelemekte, sahip olduğu basit iç balistik çözücüsünün kullanımı ile eş zamanlı olarak ısıl analiz ve aşınma analizi gerçekleştirme imkanı sağlamaktadır. Eriyerek aşınma için yüzey enerji korunumu, kömürleşme ve reaksiyon ürünü gazların malzeme içerisindeki etkisi ve akış alanına

enjeksiyonunu tanımlayan denklemler basit bir iç balistik sınır koşulunu da içerek şekilde ticari analiz yazılımı FLUENT içerisine uygulanmış ve tamamen eş zamanlı eksenel simetrik bir analiz aracı elde edilmiştir. Reaksiyon ürünü gazların enjeksiyonunun değerlendirilmesine yönelik olarak kaynak terimlerin kullanıldığı yeni bir sınır koşulu uygulanmış ve analitik çözümler ile doğrulanmıştır. Aşınma kaynaklı şekil değişikli içeren hesaplamalı akışkanlar dinamiği analizlerinde görülen kararsızlık irdelenmiştir. Lüle ısıl analizlerinde kullanılan türbülans modelleri ve literatürde sıklıkla kullanılan Bartz ısı transferi korelasyonu karşılaştırılmıştır.

KAYMAK literatürde yer alan veriler ile doğrulanmış, ve FLUENT uygulaması KAYMAK sonuçları ile teyit edilmiştir. Silika-fenolik lüle kartuşu içeren ufak bir katı yakıtlı roket motoru ile statik ateşleme gerçekleştirilmiş ve elde edilen sonuçlar geliştirilen analiz yöntemleri ile karşılaştırılmıştır. Malzeme karakterizasyonuna dair yüksek seviyede belirsizliklerin mevcudiyetine karşın, yakın sonuçlar elde edilmiş ve tüm fiziksel unsurların analiz tarafından yakalanabildiği gösterilmiştir. FLUENT uygulaması ile analiz ortamında modellenen fiziksel unsurların daha basit bir yaklaşım içeren KAYMAK ile elde edilemediği gösterilmiştir.

Anahtar Kelimeler: aşınma, kömürleşme, kömürleşerek aşınma, lüle, katı yakıtlı roket motoru, silika-fenolik, iç balistik

Dedicated to my family

ACKNOWLEDGMENTS

I would like to express my gratitude to Prof. Dr. Yusuf ÖZYÖRÜK for his guidance, interest and faith in this study. Without his support as a supervisor this work would not be possible.

Many thanks to my colleagues in TÜBİTAK-SAGE, especially Berksu ERKAL, Burak SÖĞÜTÇÜ, Caner Ekin KİPER, Esra Yıldar BAŞARAN and Levent Çağatay ÖZ for their support and efforts that aided the preparation of this thesis. And special thanks to Dr. Bülent SÜMER, Chief of Propulsion Systems Division in TÜBİTAK-SAGE for his support and faith on research and development efforts and understanding throughout the development of this thesis and my career.

I am grateful for the care, support, sweetness and patience of my wife Yasemin ALANYALIOĞLU during this period. Each cup of tea and coffee she kindly provided has been my fuel, and she has always managed to motivate me whenever I felt lost and exhausted.

Finally, I would like to thank my family for their support, encouragement and patience during this period. They have always been supportive and understanding throughout my life and I am grateful to have such a family.

TABLE OF CONTENTS

LIST OF TABLES

TABLES

LIST OF FIGURES

FIGURES

LIST OF ABBREVIATIONS

1D	1 Dimensional
2D	2 Dimensional
3D	3 Dimensional
AP	Ammonium Perchlorate
CFD	Computational Fluid Dynamics
DSC	Differential Scanning Calorimeter
KAYMAK	Kömürleşerek Aşınan Yalıtım Malzemeleri Analiz Kodu
SRM	Solid Rocket Motor
TGA	Thermogravimetric Analysis
UDF	User Defined Function
UDM	User Defined Memory
UDS	User Defined Scalar

LIST OF SYMBOLS

a	Burn rate constant
A_b	Burn area
A_t	Nozzle throat area
A_e	Nozzle exit area
A_j	Pre-exponential factor for j'th decomposition reaction
c^*	Characteristic velocity
C_F	Nozzle thrust coefficient
C_h	Stanton number for heat transfer
C_p	Specific heat capacity at constant pressure
D_t	Throat diameter
E_j	Activation energy for j'th decomposition reaction
H and h	Enthalpy
I_{sp}	Specific impulse
k	Thermal conductivity
$\dot{m}$	Mass flow rate
$\dot{m}''$	Mass flux
n	Burn rate exponent
P	Pressure
P_a	Ambient pressure
P_c	Chamber stagnation pressure
P_e	Nozzle exit pressure
R	Specific gas constant
$\dot{s}$	Recession rate or volumetric source term

s	Recession
t	Time
T	Temperature
T_c	Chamber stagnation temperature
u	Axial component of velocity vector
Q^*	Heat of Ablation
$\dot{q}''$	Heat flux
$\mathbf{v}$	Velocity vector
η_{C_F}	Nozzle thrust efficiency
ΔH_f^{298}	Enthalpy of formation at a reference temperature of 298 K.
ϵ	Emissivity
γ	Ratio of specific heats
Γ_M	Mass fraction
Γ_V	Volume fraction
ρ	Density
ρ_p	Propellant density
ρ_0	Initial density for decomposing component
ρ_r	Residual density for decomposing component
ρ_R	Effective reinforcement density
σ	Stefan-Boltzmann constant

CHAPTER 1

INTRODUCTION

This chapter includes fundamental information related to solid rocket motors and charring ablators to provide basis to introduce the motivation of this thesis, without digging deeper into theoretical aspects. Following that, other works in literature are investigated and finally the scope of the thesis is defined.

1.1 Motivation and Problem Definition

Solid rocket motor propulsion systems are perhaps the most common choice for tactical missile systems due to their mechanical simplicity and long shelf life. [8, 9]. In these systems, chemical energy stored in solid propellant is converted to kinetic energy by means of combustion of solid propellant and acceleration of the combustion products through a converging-diverging nozzle to produce useful thrust.

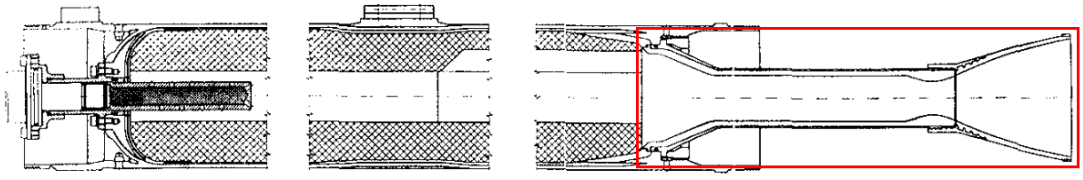

Figure 1.1: Cross section of a tactical air-to-air missile solid rocket motor, nozzle is highlighted. [4]

Among the parts making up a solid rocket motor, nozzle is the most critical in terms of thermal load. In Figure 1.1 a blast tube type nozzle commonly employed in tactical missile systems is illustrated. The heat flux values present in the nozzle of a solid rocket motor are comparable to those of re-entry conditions, exceeding 50 MW/m^2.

Unless necessary measures are taken, severe heating of structural or nearby sensitive components or failure of nozzle is almost certain. A common example of nearby sensitive components is the control actuation systems located adjacent to the tubular part of the nozzle as illustrated in Figure 1.1, assembled by employing a removable exit cone attached to the blast tube section. Hence, thermal management of nozzle poses an important design consideration in solid rocket motor nozzle design.

Almost all solid rocket motor systems are designed for single time usage and face destruction after executing their task, with exceptions such as Space Shuttle Solid Rocket Boosters which are recovered and some parts are refurbished to be used again. As the performance of a propulsion system can be characterized by its thrust-to-weight ratio, a design goal for an optimal SRM is to minimize the mass of non-propellant components, even up to such an extent that some parts exposed to the internal environment of the SRM barely survive until the end of mission and designed accordingly [9]. Hence a critical requirement for nozzle thermal protection is low weight, which is a serious disadvantage for the consideration of heat-sink type solutions.

Another important consideration related to the nozzle is that the operating point of a SRM in terms of pressure is dictated by a balance between the propellant burn area, propellant burn rate, and nozzle throat area. The simplest form of the equation describing this phenomena is given by below equation, under the assumption of Saint-Vielle's Law for burning rate and quasi-steady operation with no total pressure loss or erosive burning inside the chamber.

$$P_c = \left(\rho_p a c^* \frac{A_b}{A_t} \right)^{\frac{1}{1-n}} \tag{1.1}$$

The first two of aforementioned factors determine the rate of gas generation and the latter one limits the mass flow rate of gas leaving the nozzle. Hence, in terms of interior ballistics, it is evident that accounting for the change in throat area during operation is a very important consideration during design. Here, the ratio $\left(\frac{A_b}{A_t}\right)$ is commonly referred to as *Klemmung*, and all other terms appearing in Equation 1.1 can be considered as constant within current consideration. The immediate outcome is that *Klemmung* is the parameter that defines the interior ballistic operating point of a SRM. As the throat area A_t is proportional to the square of throat diameter D_t,

following deduction given by below expression can be made.

$$P_c \propto D_t^{\frac{2}{n-1}} \tag{1.2}$$

The term n appearing in these equations can be interpreted as the pressure sensitivity of the propellant burn rate, and common values for most of the solid propellants lie between 0.3 - 0.6. Hence, for a propellant with $n = 0.5$, a 1% increase in throat diameter approximately corresponds to a 4% loss in chamber pressure. While excessive erosion of the throat can be a serious issue on certain SRM designs, some of them might favor a certain amount of throat erosion to design a lighter nozzle and to control the thrust-time curve by introducing another control parameter, the throat recession rate. For interior ballistics considerations this may pose a serious advantage, as the control of thrust-time curve can only be achieved by means of propellant grain design. In either case, a concrete knowledge about the throat erosion rate is vital.

Everything else being equal, an increase in the throat diameter during firing reduces the performance of the SRM, which is generally measured in terms of I_{sp} as given by below expression,

$$I_{sp} = C_F c^* \tag{1.3}$$

The form of Equation 1.3 is a rather uncommon form to express I_{sp}, which is the thrust produced for unit mass flow rate of propellant, however this form allows to consider the effects of nozzle and combustion separately. The nozzle thrust coefficient, C_F is given by below Equation and the characteristic velocity, c^* is given by Equation 1.5. The value of c^* is relatively insensitive to chamber pressure within practical ranges of operation, as illustrated in Figure 1.3, and dependent on the combustion process of solid propellant.

$$C_F = \eta_{C_F}\gamma\sqrt{\frac{2}{\gamma-1}\left(\frac{2}{\gamma+1}\right)^{\frac{\gamma+1}{\gamma-1}}\left[1-\left(\frac{P_e}{P_c}\right)^{\frac{\gamma-1}{\gamma}}\right]} + \left(\frac{P_e}{P_c}-\frac{P_a}{P_c}\right)\frac{A_e}{A_t} \tag{1.4}$$

$$c^* = \sqrt{\frac{1}{\gamma}\left(\frac{\gamma+1}{2}\right)^{\frac{\gamma+1}{\gamma-1}} RT_c} \tag{1.5}$$

The terms P_c and P_e appearing in Equation 1.4 are also functions of throat area. η_{C_F} is the nozzle thrust efficiency, and includes the effects of various phenomena leading to deviations from remaining terms, $C_{F_{ideal}}$, based on isentropic flow considerations.

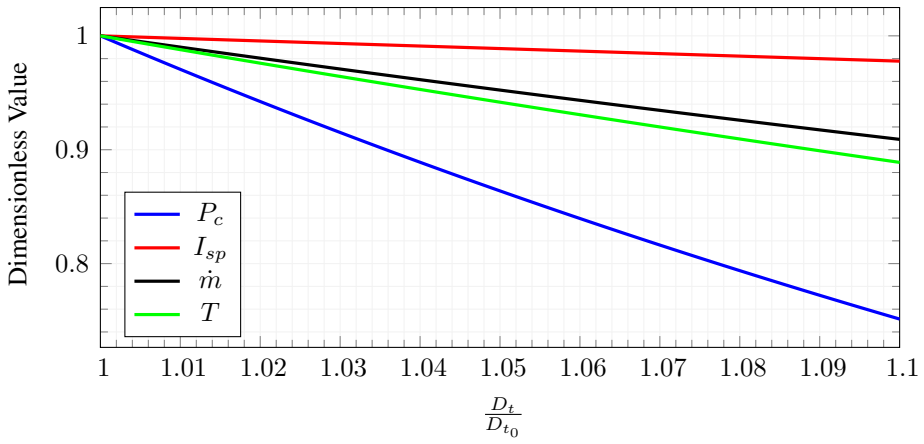

Figure 1.2: Illustration of I_{sp} loss with presence of throat regression, considering constant η_{C_F} and c^* for $n = 0.5$.

These phenomena include divergence losses due to the internal shape of nozzle, losses due to low flow velocity in boundary layer, losses due to chemical kinetics and two phase flow and energy loss due to heat transfer. For a nozzle contour of changing shape, the divergence loss may change significantly during operation, which is related to the amount of gas leaving the nozzle in directions not parallel to nozzle axis. The discussion related to the performance loss is summarized in Figure 1.2, for a case illustrating a 10% increase in throat diameter which is a practical amount. The value of I_{sp} does not decrease as much as P_c; however, for this case an I_{sp} loss of 2% can be expected, which is a considerable amount especially for large SRMs used in space launch applications. Since this 2% loss is analogous to carrying 2% more propellant, the loss in payload carriage capability corresponds to huge amounts of mass considering large amount of solid propellant used in these systems.

Solid propellants used in SRM's can be divided into two main categories as the double base propellants and composite solid propellants. Here, we will restrict our attention to composite solid propellants, which are used for almost all modern tactical missile and launch systems. Composite solid propellants can be further divided into two categories based on their aluminum content as low or not aluminized composite propellants and aluminized solid propellants. The latter ones provide a much higher adiabatic flame temperature and hence higher values of I_{sp}. However they produce large amounts of visible smoke and molten aluminum particles within flow field, hence

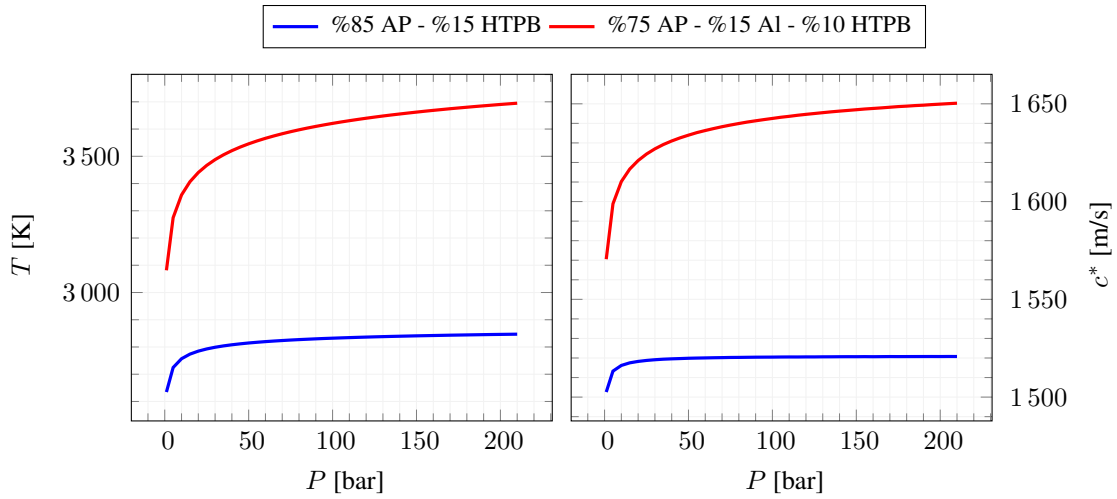

Figure 1.3: Theoretical equilibrium values of T_c and c^* for a generic aluminized and non-aluminized composite propellant.

requires two-phase flow treatment. The choice between the two categories depends heavily on the specifications of the system in consideration. For modern composite solid propellants, the recovery temperatures are on the order of 3000 K, and the gaseous products consists of oxidizing species, such as CO_2, H_2O, OH and CO. Theoretical equilibrium values for adiabatic flame temperature and characteristic velocity are given in Figure 1.3 for generic aluminized and non-aluminized composite solid propellants. Together with the immense amount of mass flux and pressures often on the order of 100 bars, plus presence of molten aluminum particles in some cases, it poses a very destructive environment such that no known material can survive continuous exposure without sacrificing some amount of mass. An excellent survey involving behavior of many materials, including refractory metals such as tungsten and molybdenium, exposed to various solid propellant formulations can be found in [10]. While historical nozzles were made of steel, usage of temperature resistant materials such as graphite, refractory metals such as tungsten or molybdenium, generally employing a heat sink type solution [11] were common. Development of charring ablators such as carbon-phenolic and silica-phenolic and application of these materials as nozzle liners led to the development of modern, highly efficient solid rocket motors, latter two being the most common in modern systems. [9].

Charring ablators have been used on SRM nozzles and reentry vehicles for more than

60 years [12, 13], as they provide a lightweight and cost effective solution to the heating problem. They are used to form the nozzle contour and generally housed inside a metal case. A certain carefully designed thickness distribution of charring ablator is present along the nozzle axis. Depending on the application, a separate throat insert such as graphite might be present to reduce the erosion rate of throat. In this case, charring ablator is generally present behind the throat insert since commonly used graphite does not serve as an insulator. As charring ablators do not posses strong mechanical properties, they are generally not used for applications requiring structural strength. However, for certain applications the mechanical strength is sufficient and no structural material is used. A common example for this is the exit cone (diverging section of the nozzle), where the pressure rapidly decreases due to expansion of gases. During firing, the exposed surface of charring ablator might recede depending on the local flow conditions, and hence the nozzle aerodynamic contour may not be considered static throughout firing. This implies that the thrust efficiency of the nozzle may become a non-negligible dynamic phenomena with usage of charring ablators.

This thesis deals with the analysis of charring ablators in solid rocket nozzles, in particular charring ablators undergoing melting ablation such as that occurs in silica-phenolic [14]. The goal is to develop necessary analysis tools to aid interior ballistics and structural design by means of reducing the number of experiments, and achieve more optimal insulation thickness distribution. In particular, work done in this thesis addresses the following questions considering a silica-phenolic nozzle:

1. How much insulation thickness is required to stay below the predefined outer temperature limit?

2. What will be the throat recession rate?

3. How does the shape of nozzle contour change and what are the implications on SRM performance?

1.2 Charring, Ablation, and Charring Ablation

In this section, definitions related to the concept of charring ablation and underlying physical mechanisms are introduced. The reader may refer to Figure 1.4 for a graphical illustration of physical phenomena discussed in this section.

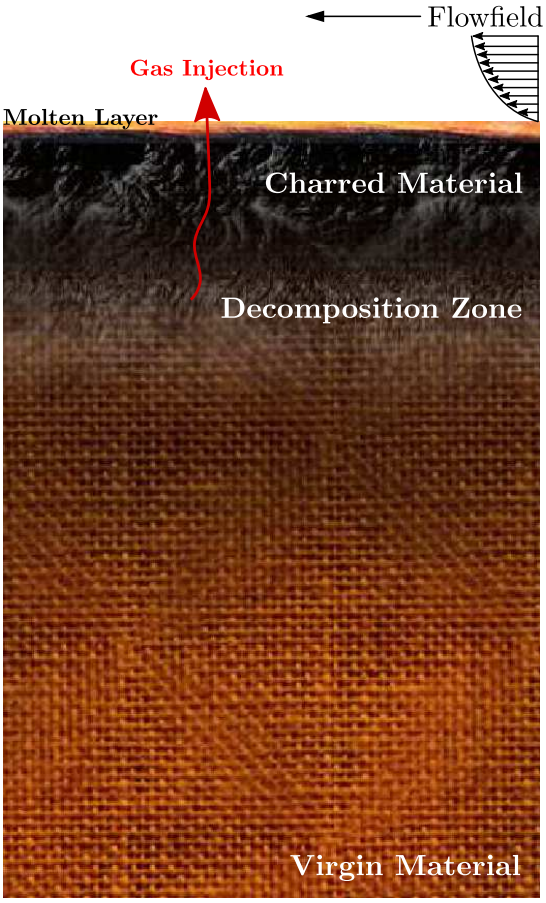

Figure 1.4: Illustration of physical phenomena in silica-phenolic under high heat flux.

1.2.1 Ablation

The term ablation originates from the latin word *auferre*, which means to remove [15]. For ablative materials, ablation is a thermophysical process which involves loss of surface material resulting as removal of a large amount of heat. There are different physical mechanisms for ablation. Although only melting ablation is considered in this work, brief information regarding the other types is included in this section.

The process of mass loss of each material used as a nozzle liner or throat insert can be considered as a subset of ablation. The main mechanisms common in SRM nozzles are as follows,

- Ablation due to surface reactions, mainly due to oxidation of carbon. This is the mechanism present in graphite, carbon-carbon and carbon-phenolic. Also refractory metals are subject to oxidation. This type of ablation is generally termed as thermochemical ablation.

- Melting, vaporization and/or sublimation, mainly occurs in silicate materials and teflon [16]. This type of ablation is Generally considered as a fail mechanism.

- Mechanical mass removal due to shear and particle impingement.

The ablation process that occurs in silica-phenolic is melting ablation [14, 17]. Silica phenolic composite insulation material consists of silica (SiO_2) reinforcement fibers and phenolic resin (C_6 H_5 OH) mixed with a certain fraction. If the temperature and heat flux is sufficient, SiO_2 melts at about 1996 K and forms a molten layer adjacent to the solid surface which is to be mechanically removed due to shear stress together with the carbonaceous residue from char. This process has been reported as like "lava flow" in [18]. Unlike thermochemical ablation, this process seems not to be affected by the presence of aluminum particles present in the combustion products [17].

The experimental investigation of ablation and associated dynamics pose a difficult task. Specimens to be used in reentry systems are generally tested in arc-jet facilities within controlled chemical and thermal environments to characterize material and aid modeling efforts such as those reported in [19]. For rocket nozzle applications, most common experimental approach is to investigate the ablative characteristics of the material in the real operational environment by performing firing tests with a subscale test article. Chapter 5 investigates such a test article.

1.2.2 Charring

Charring is an in-depth decomposition process which can also be observed in daily life, such as that occurs in wood subjected to high temperatures, followed by a visible color gradient across its cross section, as illustrated in Figure 1.4. Once heated, charring materials undergo decomposition reactions, which are referred as pyrolysis reactions. As a result loss of mass occurs and gaseous products referred as pyrolysis gas are formed. These reactions are highly endothermic, hence serve as an excellent heat dissipation mechanism, and should be considered in detail when analyzing the in-depth temperature response of a charring material. The initial state of a charring material is referred as *virgin*. Once it is completely charred, i.e no more density change occurs when temperature is increased, the state of material is referred as *char*. In charring ablators, these decomposition reactions occur within the resin, resulting in the following relevant physical phenomena:

- Material density decreases during charring until it is completely charred.
- A porous medium is formed inside the charred and decomposing sections of the material.
- Pyrolysis gas is formed as a result of pyrolysis reactions, and gas percolates through porous media.
- Material thermal properties change, based on local char content.

The relavant thermophysical properties, mainly k and C_p are different for the virgin and char states of material. In particular, value of thermal conductivity may change drastically. Production of gas inside the material causes further physical phenomena, as they percolate through the material, towards the hot char, the gases soak heat from the material and finally injected outside from the surface of the material into the boundary layer. This injection process may further decrease the rate of heat transfer due to blowing effect as an additional mechanism for heat blockage. For certain cases, pressure build up of pyrolysis gas may damage the material and additional measures become necessary to avoid this issue. The pyrolysis gas may further react with the reinforcement material to affect the overall energy balance.

To characterize a charring material and provide necessary data to perform a thermal analysis, a detailed characterization process is necessary. To obtain the chemical kinetics of pyrolysis reactions, TGA and DSC tests are performed with different heating rates to form a chemical kinetics model [20]. While this is the standard procedure, the heating rates of the material in the operational environment is generally at least one order of magnitude higher then of those present in TGA tests. Thus, kinetic models based on this data introduce the assumption that the data is valid over the operational range. While the thermophysical properties of virgin material can be obtained by means of standard test methods, the same approach may not be applicable to charred material. Since specimens charred in oven may not be representative of the material charred in actual operating environment [20, 21], a common method is to derive the thermophysical properties of charred state by means of correlation between experimental data and analysis [20].

1.2.3 Charring Ablation

As the name suggests, charring ablators are charring materials that also undergo ablation. Most common examples are silica-phenolic and carbon-phenolic when modern SRM nozzles are considered. In conjunction with previous discussions and Figure 1.4, the physical processes relevant to silica-phenolic in a SRM nozzle environment can be summarized as follows,

1. Once temperature begins to increase within the material, endothermic pyrolysis reactions start to commence. Their rate is determined by the local heating rate. Density of the material begins to decrease, and a porous structure begins to form.

2. Gaseous products of pyrolysis flow within the porous media and an energy exchange between gas and solid occur, favoring to decrease the solid temperature as gas flows through hot zones.

3. Pyrolysis gas reaches the surface, and injection affects the boundary layer dynamics. This is termed as *blowing* and reduces the effective convective heat

transfer rate. It has to be noted that surface reactions occurring in carbon based materials (graphite, carbon-phenolic etc.) also cause this effect.

4. Once the surface temperature reaches around 1996 K, silica fibers begin to melt, and a molten layer forms adjacent to the surface. While this may effect the dynamics of energy transfer between flowfield and solid, it is rather ambiguous and considered beyond the scope of this work; however, a limited amount of work is available in literature considering the dynamics of melt layer. As the melt layer forms, the carbonaceous remnants of the char layer are considered to be removed with the melt layer. After this point, surface temperature is considered to be equal to the melting temperature of silica fibers.

5. During this process, surface re-radiation is also an effective heat rejection mechanism which should be considered [17, 20].

There are additional phenomena related to the processes involved in silica-phenolic which are considered beyond the scope of this thesis, which are rather only to be named here. One of them of primary importance is the solid state carbon - silica reactions present in that may occur in the char layer under high temperatures, and effect the local thermal properties. Another such phenomena is the so called char-swelling, which as the name suggests is the volume expansion that may occur when material is charred.

1.3 Literature Survey

This section contains an overview of related work available in literature in a chronological fashion. As most of the material available in this field is related to the field of reentry, attention is restricted to applications on rocket nozzles in general. However, some works involving reentry are outlined due to their special features related to the analysis of charring ablators. Reader is referred to [22] for a detailed review about all analysis tools available for this field up to 2011.

With the development of charring ablators around 1960's [13], related theories, analysis methodologies and tools also began to develop. Probably the first well known

tool to come up was Charring Material Ablation (CMA) in 1968 [12], where details related to its development can be found in [23–25]. Ever since, CMA has become a widely used and reliable tool for analysis of charring ablators and referred as industry standard [26]. Application areas of CMA are wide, including re-entry analysis, rocket nozzle analysis and inverse property estimation by correlating data obtained from tests. A concrete example related to the usage of CMA on analysis of a SRM nozzle is given in [4]. There, CMA3 was utilized to compute external temperatures on blast tube and exit cone sections of the nozzle employing silica-phenolic material. CMA is a one-dimensional analysis tool based on finite-difference method. It is capable to calculate in-depth temperature response of a charring ablator, by solving the kinetics of pyrolysis reactions and considering a non-accumulative approach for the motion of pyrolysis gas. The implementation of the ablating boundary condition is made with a surface energy balance method which is supplemented with pre-computed surface chemistry tables and semi-empirical correlations to account for decrease of convective heat transfer rate due to blowing effect. From materials perspective, CMA is applicable to various kind of charring ablators, including carbon-phenolic. It offers analysis modes, such as specification of a constant temperature & recession rate for the boundary condition of ablating interface, convective heat transfer calculation with Bartz correlation [27] for SRM analysis and a cool-down period analysis. The latter is especially important for SRM analysis since the heating of external surface generally occurs at a later time after propellant burnout has been achieved.

About the same period of time, a number of publications appeared in literature mainly by NASA regarding the application of charring ablators and prediction of shape change for 2D bodies for reentry applications based on boundary conditions imposed on ablating surface [28, 29]. The first application of a 2D axisymmetrical thermal analysis for a nozzle employing a charring ablator is reported in [30]. It was done by an extension of thermal analysis tool ASTHMA to properly include effects related to in-depth charring, to be named ASCHAR. This application can be considered as a 2D/axisymmetrical extension of CMA as reported in [30]. They are based on the same set of governing equations solved with an explicit finite difference scheme opposed to the implicit finite difference scheme in CMA. The motion of pyrolysis gas inside the material is treated as 1D in local normal direction at each node. It has to

be pointed out that during this time period, there were certain other publications related to the analysis of in-depth charring ablation in 1D, based on different numerical schemes and mainly concentrating on computational cost. These are not discussed in detail here.

In [31] a boundary condition termed as Q^* (Heat of Ablation) is introduced. This is a simplified form for the resultant outcome of surface thermophysics, and assumes that ablation takes place under a constant temperature. The value of heat of ablation Q^* is used to determine how much material is to be removed. The model was implemented on a stretching grid scheme with finite volume method for 2D and axisymmetric geometries. The energy balance considered here did not include effects due to charring. Probably one of the first detailed analysis regarding the dynamics of pyrolysis gas inside the material is found in [32]. It was determined that the assumptions regarding the dynamics of pyrolysis gas in CMA were the probable cause of discrepancies to field data obtained from reentry vehicles. Also the assumption of zero residence time for pyrolysis gas cannot be considered adequate for certain reentry conditions, and validity is limited to small char and reaction zone thickness. Hence a method based on porous medium flow was introduced to solve the 1D continuity and momentum equations for pyrolysis gas inside material, and improvement in the discrepancy aforementioned was reported to improve. Further validation regarding the pressure of pyrolysis gas inside material is also given in [33].

A rather extensive literature survey on the modeling of charring ablators subcategorized to different application areas was conducted in [34], which includes data up to 2006. Based on their findings, there were no conjugate analysis of flowfield and charring ablator dynamics involving the injection of pyrolysis gases and a dynamically deforming grid system up to 2006. A certain advancement that should be mentioned is the work carried out in [35], where a 2D/axisymmetrical in-depth response tool was coupled with a CFD code and conjugate analysis was performed. However, surface regression and pyrolysis gas injection effects were not present. Also it appears that surface regression rates were computed based on models involving experimental correlations, as no special interface treatment between fluid and solid zones was included. One of the first analysis of CFD coupled analysis of an ablative boundary can be found in [36, 37], which investigated the effects of gas injection to the boundary

layer for a hypotethical case involving graphite using a surface energy balance and thermochemical ablation boundary condition. The results were compared to blowing rate correction factors on heat transfer rate employed in CMA and other codes, and it was shown that discrepancies increase with increasing rate of gas injection into boundary layer.

A comprehensive 1D analysis tool introduced in [7,38,39] includes certain numerical improvements such as fully implicit treatment of all terms and treatment of pyrolysis gas flow using Darcy's Law for porous media. For the literature survey conducted within this thesis, this work appears to be the most advanced one among 1D analysis tools encountered. Majority of the appearance of CFD within applications of charring ablators populates after 2007. In [40], which investigated the thermochemical ablation of carbon/carbon and graphite materials, a 2D/axisymmetric CFD code including a surface energy and mass balance boundary condition for ablating surface was introduced with inclusion of gas injection into the boundary layer. A static CFD grid system was used and steady-state recession rates were computed by means of chemical equilibrium and kinetics calculations. Also an example analysis involving a nozzle was demonstrated. A more detailed nozzle investigation by the same author can be found in [41]. A similar but a rather detailed implementation of a boundary condition that involves blowing was illustrated in [5]. Results include a conjugate analysis of an ablating carbon nosetip performed on a moving grid scheme. The in-depth thermal response was calculated by means of 1D code FIAT [42]. FIAT is also a 1D in-depth analysis tool that makes use of surface thermochemistry tables, however it is able to deal with non-equilibrium surface chemical conditions.

A thermal analysis oriented approach that is solely concentrated on SRM nozzles is shown in [1]. While ablating interface boundary condition has no coupling with CFD, in-depth solution capability of a domain involving charring ablators and another materials at the same time was demonstrated. Work presented in [43] involves coupling of CFD code LeMANS and material response code MOPAR (1D), including sophisitcated treatment of surface boundary conditions and pyrolysis gas injection. A 3D analysis tool involving transient shape change, FIAT3d was also introduced in [44]. There, motion of pyrolysis gas was treated 1D in local normal direction and zero residence time. Excellent agreement with test results were demonstrated. The first work

that has been encountered within this literature survey effort that involves transient shape change effects of an ablating nozzle was illustrated in [45]. The CFD analysis were performed steady-state and grid was updated whenever a predefined recession amount is exceeded. Demonstrated agreement with the post-firing nozzle profile was excellent, with carbon-carbon and carbon-phenolic as the studied materials. Special attention was given to the injection of gases produced by decomposition of phenolic resin. The effect of nozzle shape change (i.e considering a static grid for CFD analysis) was also underlined by the same authors in [46].

While no details regarding the pyrolysis gas injection or surface boundary condition for CFD side were given, a semi-coupled analysis of a SRM with 143 sec. burning duration including interior ballistics was demonstrated in [47]. The commercial CFD software FLUENT was employed for flow fields analysis, and grid was updated within certain intervals in a quasi-steady fashion. Nozzle thermal analysis was computed with coupling of an external analysis tool called Hero. Perhaps the most complete work regarding the analysis of charring ablators with application to solid rocket motor nozzles can be found in [17]. It was discussed that no past work has concentrated on behavior of silica based materials in a nozzle environment in context of a CFD approach. While in-depth temperature response was not solved, a steady-state ablation assumption was employed for generation of detailed surface energy and mass balance based boundary conditions, and these were implemented in a CFD solver. Coupling with a 1D material response solver (ImpACT) was also demonstrated by an iterative coupling scheme between two codes. The grid evolution was acarried-out in a quasi-steady fashion. While majority of this work deals with the ablation of carbon-based materials, a devoted chapter for silica-based materials and their treatment was included, which is regarded as a valuable reference for this work.

Another recent work regarding the thermochemical ablation process with application to hybrid rocket motors is given in [48], based on the same approach that has been used in [17, 40] as all of these work originated from the same university. Another work [49] illustrated the discontinuities in silica-phenolic and graphite interfaces for a nozzle employing graphite as throat insert. While no numerical analysis regarding the silica-phenolic was present, a cross-section photograph of post-firing nozzle was included, which is rather rare in literature. Most recent work related to the conjugate

analysis of nozzle flowfield and charring ablator response can be found in [50–53]. Again, the coupling strategy is similar to previously discussed cases, where steady-state analyses were performed at various discrete points in time, and concentration was focused to analysis of carbon-phenolic. However, this time a dynamic grid system was employed for nozzle flowfield and transient shape change phenomena was aimed to be captured. Certain stability issues regarding this issue and suppression of the instability was discussed, which has been especially valuable during the development of this thesis.

Based on the research conducted, it has been observed that majority of publications are related to analysis of reentry conditions, surface thermochemistry and thermochemical ablation modeling. The conjugate analysis of charring-ablator response and nozzle flowfield is a rather recent development in literature, and is an active field. General observed trend has been a loose-coupling between flowfield and material response, involving a quasi-transient approach by means of successive steady-state CFD solutions following grid update. Well established and validated theoretical and numerical framework is present in literature, especially for carbon based materials, however less amount of publications concentrate on the ablation of silica-phenolic. No special work has been encountered investigating the interior ballistics considerations in particular.

1.4 Scope of Thesis

Considering the discussions in the preceding sections, it is evident that certain specially designed analysis tools are necessary to aid the design process involving charring ablators. The tools mentioned in the previous chapter are corporate or in-house developed analysis tools, restricted to be used within their development environment (such as CMA3 is available to U.S citizens only), and there are no commercial analysis tool available.

Based on the requirements, two analysis tools are developed in this thesis with different levels of fidelity,

1. A 1D analysis tool named KAYMAK that encompasses similar capabilities to that of CMA3. With negligible amount of computational time required, this tool is suitable to use during initial phases of design where parametric studies and trade analysis are mostly performed. Another possible usage is for inverse estimation of charring ablator material properties based on data collected from tests.

2. Second tool is aimed for conjugate analysis of flow field and charring ablator response, including a comprehensive treatment for gas - surface interaction and a dynamic grid system to investigate nozzle dynamics as it recedes. This is expected to provide an increased level of fidelity.

Both tools are based on the same set of governing equations. The latter one described above is accomplished by carrying out the implementation of governing equations in the commercial CFD solver FLUENT. Since throat regression is strongly coupled with interior ballistics, a simple zero dimensional transient ballistics solver is coupled with both tools. Present context is limited to analysis of silica-phenolic composite material based on current needs, which also avoids extra complexity due to requirement of detailed surface thermochemistry approaches. However developed tools has the provision to include the models for treatment of carbon based materials through implementation of a thermochemical ablation model.

1.5 Outline of Thesis

This goal of this chapter was to introduce the reader with the concepts that are investigated within this thesis, and present a literature survey to discuss the modeling efforts that has been conducted in literature.

Following chapter focuses on the necessary theoretical framework which forms the basis of numerical methods which will be discussed in Chapter 2. Development of KAYMAK is discussed in Chapter 3. Chapter 4 is devoted to the conjugate analysis method which has been accomplished within the framework of commercial CFD solver FLUENT. Chapter 5 includes results, that are mainly validation cases adopted from literature and results of a test firing with a silica-phenolic nozzle. Final chapter

is devoted to the conclusions and possible for areas of focus for future work.

CHAPTER 2

THEORETICAL BACKGROUND

In this chapter, the governing equations and related discussion is presented.

2.1 Governing Equations

The equations that govern the in-depth thermal response for a charring ablator is the conservation of energy, conservation of mass and pyrolysis gas continuity equation. As a finite volume discretization scheme is to be considered, it is convenient to work with the integral form of the governing equations. The general conservation of energy for a solid material for a control volume with moving boundaries and source terms is given by

$$\underbrace{\frac{\partial}{\partial t}\int\limits_{V}(\rho C_p T)}_{\text{storage}} = \underbrace{\oint\limits_{S} k\nabla T\cdot d\mathbf{S}}_{\text{conduction}} + \underbrace{\oint\limits_{S}(\rho C_p T)\,\mathbf{v}_s\cdot d\mathbf{S}}_{\text{grid convection}} + \underbrace{\int\limits_{V}\dot{s}dV}_{\text{sources}} \tag{2.1}$$

where $d\mathbf{S}$ is $\hat{\mathbf{n}}dS$, outwards pointing area vector on the control surface defining the boundary of the control volume. The terms appearing in Equation 2.1 represent net rate of storage of energy, net rate of energy transfer due to conduction, net rate of energy transfer due to grid convection and net rate of heat generation/loss due to sources present within the volume. The effects of phenomena occurring within the charring ablator are to be included within this source term. Neglecting the solid-solid reactions such as carbon - silica reactions present in silica phenolic [19], the only contributions are due to the heat of pyrolysis and energy transfer between pyrolysis gas and solid material, hence the source term can be expanded as

$$\dot{s} = \dot{s}_{\text{pyr}} + \dot{s}_{\text{gas}} \tag{2.2}$$

As introduced in the preceding chapter, the charring is a chemical process that occurs due to pyrolysis reactions occur within the resin. The rate of these reactions govern the rate of density change within the material, and as they are endothermic a source term associated with the heat of pyrolysis needs to be considered in the energy equation. The widely accepted pyrolysis mechanism for phenolic resin is a three component decomposition scheme expressed with Arrhenius type rate equations [17, 19]. The material is assumed to be composed of individually decomposing fictitious resin components that will be termed as A and B, and a non-decomposing reinforcement part that will be termed as R. With the definition of Γ_V as the volumetric fraction of the resin, the density of the material is calculated by

$$\rho = \Gamma_V \left(\rho_A + \rho_B\right) + \left(1 - \Gamma_V\right) \rho_R \tag{2.3}$$

note that the number of fictitious decomposing components can be any integer that is dependent on the modeling of pyrolysis kinetics, however this section is prepared based on the commonly used three component scheme for phenolic resin in literature.

The reinforcement part does not decompose, i.e $\dot{\rho_R} = 0$. The rate of decomposition is given below, where dependence of the decomposition rate to heating rate can be immediately observed.

$$\frac{\partial \rho_j}{\partial t} = \left(\rho_{0,j} - \rho_{r,j}\right) \left(\frac{\rho_j - \rho_{r,j}}{\rho_{0,j} - \rho_{r,j}}\right)^{n_j} A_j e^{\frac{-E_j}{RT}} \quad \text{where} \quad j = A, B \tag{2.4}$$

The terms appearing in Equation 2.4 as $\rho_{0,j}$ denote the initial density of the corresponding component, and $\rho_{r,j}$ denote the residual density of the corresponding component. Terms n_j, A_j and E_j are the Arrhenius kinetic constants. For the common phenolic decomposition model in the literature component A is a vanishing component, that is $\rho_{r,A} = 0$. The value of $\rho_{r,B}$ is finite accounting for the carbonaceous residue from the resin once material is completely charred. The energy source associated with the heat of pyrolysis is obtained by

$$\dot{s}_{\text{pyr}} = -\Gamma_V \left(\dot{\rho}_A + \dot{\rho_B}\right) \Delta H_{\text{pyr}}|_T \tag{2.5}$$

where the term $\Delta H_{\text{pyr}}|_T$ represents the heat of pyrolysis and it can be computed as below, where h_g is the enthalpy of pyrolysis gas.

$$\Delta H_{\text{pyr}}|_T = h_g(T) - \bar{h}(T) \tag{2.6}$$

The term $\bar{h}$ represents the enthalpy of the solid and can be evaluated by the following expression. [54] includes a derivation for this equation.

$$\bar{h} = \frac{\rho_v h_v - \rho_c h_c}{\rho_v - \rho_c} \tag{2.7}$$

This computation requires information about the enthalpies of virgin and charred states, and a theoretical approch regarding the computation of enthalpies is included in Section 2.5. Conversion between resin mass fraction and volume fraction can be done as follows,

$$\Gamma_M = \frac{\Gamma_V \left(\rho_{0,A} + \rho_{0,B}\right)}{\rho_R \left(1 - \Gamma_V\right) + \Gamma_V \left(\rho_{0,A} + \rho_{0,B}\right)} \tag{2.8}$$

$$\Gamma_V = \frac{\Gamma_M \rho_R}{\Gamma_M \rho_R + \left(\rho_{0,A} + \rho_{0,B}\right)\left(1 - \Gamma_M\right)} \tag{2.9}$$

Since density of the material has been expressed a linear combination of ρ_j and ρ_R at a given location by Equation 2.3, the conservation of mass for each contributing component A and B shall be separately considered with the associated grid convection terms for a dynamic grid system as follows,

$$\underbrace{\frac{\partial}{\partial t}\int_V \rho_j dV}_{\text{storage}} = \underbrace{\int_S \rho_j \mathbf{v}_s \cdot d\mathbf{A}}_{\text{grid convection}} + \underbrace{\int_V \dot{s} dV}_{\text{sources}} \quad \text{where} \quad j = A, B \tag{2.10}$$

The terms in Equation 2.10 represent the rate of change of stored mass, net inflow/outflow of material due to grid convection and a source term which has already been introduced in Equation 2.4. Note that Equation 2.4 shall be included with a minus sign in this source term since rate of change of density due to pyrolysis is negative.

Considering the phenomena discussed so far in this section, only remaining contribution is due to the effects of pyrolysis gas. As introduced in the preceding chapter, the gaseous products of the pyrolysis reactions do have a contribution on energy balance which can not be neglected. To model these effects, certain assumptions are necessary. The recent trend in literature has been to model the flow domain of pyrolysis gas within the material by implementing a porous media formulation and obtaining a simplified expression for the momentum equation as Darcy's Law or Folcheimer's Law, or combination of both. With this kind of approach, the flow pattern of pyrolysis gas, its internal pressure and velocities can be obtained. It has been observed within literature survey that most of the modeling efforts regarding the internal behavior of pyrolysis gas originate from the need to reconstruct certain experimental

data obtained from re-entry vehicles, which are subject to very thick char layers and lesser heating rates when compared to SRM applications. Various sources suggest that for very high heating rates and thin char layers, a greatly simplified approach is also applicable, which fits for the conditions that occur within a charring ablator present in a SRM nozzle. This is also the approach considered in CMA3 [23], and can be summerized as follows,

- Pyrolysis gas has zero residence time (i.e no accumulation) within material. Formed gas leave the material instantly from the interface.

- Pyrolysis gas is isothermal with material as it percolates through.

For a 1D domain, this dictates that all the gaseous products formed within a timestep leave the domain through the interface. Under these assumptions, it is no longer required to solve an additional differential equation to model the dynamics of pyrolysis gas, and amount of pyrolysis gas flowing at a location r can be obtained as follows, where r denotes the direction perpendicular to the heat flux.

$$\dot{m}_{\text{gas}} = \sum_{r}^{r_{\text{max}}} \int_{V} \Gamma_V \left(\dot{\rho}_A + \dot{\rho_B} \right) dV \tag{2.11}$$

Above equation simply states that the amount of pyrolysis gas flowing through a location is the sum of all the gas generated *above* that location. With the isothermal assumption, the energy transfer between the gas and solid material can be obtained as follows,

$$\dot{s}_{\text{gas}} = \int_{S} \left(\rho h\right)_{\text{gas}} \mathbf{v}_{\text{gas}} \cdot d\mathbf{A} = -\dot{m}_{\text{gas}} \Delta h_{\text{gas}} \tag{2.12}$$

The above consideration regarding the movement direction of pyrolysis gas has physical sense only within a 1D domain whereas all other governing equations presented in this section are valid regardless of the physical dimensions. KAYMAK is a 1D solver, whereas the FLUENT implementation needs to consider 2D effects. Detailed description for the extension of these assumptions for 2D analysis is presented in Chapter 4, which considers gas movement constrained within local normal directions.

2.2 Boundary Conditions

Within the context of a 1D domain, there are two boundary conditions that needs to be modeled for various analysis conditions. While treatment of back surface, indicated as structure in Figure 1.4 is straightforward, the boundary condition for the heated surface comes in form of a surface energy balance equation. While the discussion in this section is mainly carried out within the context of a 1D analysis, same surface energy balance equation applies for a multidimensional conjugate analysis at faces separating the solid and fluid zones.

2.2.1 Surface Energy Balance

The proper boundary condition that needs to be applied at the fluid/solid interface comes from the resolution of surface energy balance of the infinitely thin surface separating the solid and fluid regions. The resolution of surface energy balance becomes especially important when dealing with materials that do not have a constant surface temperature during ablation. Graphite, carbon-carbon and carbon-phenolic are the commonly used examples of this kind. For ablation problems it becomes important to numerically track the surface temperature precisely.

The reader is referred to [17, 36, 51] for detailed derivations and applications of surface energy and mass balance approach. For our considerations here regarding melting ablation of silica-phenolic, we will restrict our attention to two distinct regimes regarding the condition of the surface. These are the heating or cooldown phases where no solid mass loss from the surface is present, and the melting ablation in which the surface temperature is assumed to be constant. Since no surface reactions are considered within the scope of this work, surface mass balance is not investigated in detail.

2.2.1.1 Stationary Surface

The stationary surface case corresponds to the heating or cooldown phases in which no ablation, i.e surface material consumption is present. The purpose of this sur-

face energy balance is to provide the necessary surface temperature information for accurate computation of conductive heat flux supplied to the material. A schematic describing the contributing energy fluxes are given in Figure 2.1. Note that we have

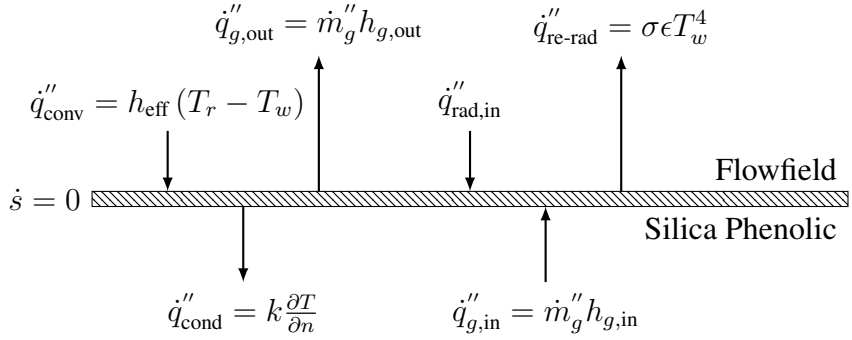

Figure 2.1: Surface energy fluxes for heating or cooldown phases.

neglected the possible energy fluxes due to diffusion of species between the surface and the adjacent flow field as these effects are generally relevant to thermochemical ablation problems. For the stationary surface case, the energy fluxes entering the surface are,

1. Convective heat flux due to heat transfer between flowfield and solid material.
2. Energy flux of the incoming pyrolysis gas from deep within material.
3. Radiant heat flux.

And the leaving energy fluxes are,

1. Energy flux due to re-radiation.
2. Energy flux of leaving pyrolysis gas.
3. Heat flux due to the heat conducted to the solid material.

In conjuction with Figure 2.1, the surface energy balance for the stationary surface case can be obtained as follows,

$$q''_{\text{conv}} + q''_{\text{g,in}} = q''_{\text{re-rad}} + q''_{\text{cond}} + q''_{\text{g,out}} \tag{2.13}$$

The treatment of convective heating term in Equation 2.13 depends on the type of analysis conducted, i.e if flowfield is modeled by means of a CFD analysis then q''_{conv} can be obtained by means of local normal temperature gradient at the wall, which will be discussed in Chapter 4. Within KAYMAK, the convective heating is modeled with an effective convective heat transfer coefficient, yielding the following equation, where T_r is the recovery temperature.

$$h_{\text{eff}}\left(T_r - T_w\right) = \sigma\epsilon\left(T_w^4 - T_{\text{surr}}^4\right) + k_s\frac{\partial T}{\partial n} + \dot{m}''_{\text{gas}}\frac{\partial h_{\text{gas}}}{\partial n} \tag{2.14}$$

Resolution of above equation dictates the surface temperature for heating/cooling phase in which no ablation takes place and surface is stationary. Another point to mention here is that the incoming radiative heat flux can be omitted for most of SRM nozzle applications, especially for non-aluminized propellants. For aluminized propellants, presence of liquid Al_2O_3 droplets may include significant radiative heating contributions.

2.2.1.2 Ablating Surface

Once ablation is commencing, the surface of the solid material is no longer spatially static. The analysis is carried out on a coordinate system tied to the receding surface, and all energy transfer phenomena is considered relative to the surface, that is considering the surface as static and everything else as moving away or towards the surface. The surface energy balance presented in this section is based on works given in [17, 20] both including detailed explanations.

As in [20], the surface mass loss due to fail modes such as spallation and melting do not contribute to the surface energy balance as the mechanisms driving this phenomena are based on mechanical effects. As briefly introduced before, the accepted surface mass loss mechanism in silica phenolic is due to the removal of the molten layer, which includes liquid SiO_2, and carbonaceous residue from resin is considered to be removed within this layer. As indicated in [17], additional information describing the removal of melt layer or additional assumptions regarding this process is necessary. Physically the removal mechanism and thickness of the melt layer depends on the local properties and viscous stresses present within the melt layer.

There are certain works in literature that attempt to describe the dynamics of melt layer. In [19] melt layer has been considered as a constant thickness zone of user supplied value adjacent to a foamy zone described by products of silica - carbon reactions. Some derivations are also included to represent thermal conductivity within this zone, however limited success is reported. Another recent work [55] investigates the dynamic of melt layer with its impliciations on surface ablation within consideration of silicate materials, mainly meteroids and certain thermal protection systems used in re-entry vehicles. Findings indicate that the significance of the molten layer in terms of effecting surface recession decrease. However since the conditions and materials considered in [55] differ from that of considered in this thesis, no quantitative deductions are made.

Following the methodology in [17], the mass removal mechanism is assumed as a sudden fail process, neglecting the internal dynamics of melt layer and viscous stresses which describe the driving process for the removal of melt layer. As underlined in [20], fail mass loss mechanisms do not contribute to the surface energy balance, however we still need to account for the heat of phase change of SiO_2 from solid to liquid state. This process is assumed to undergo as a surface mechanism and treated separately from the convected char enthalpy due to movement of surface. Assuming that the reinforcement consists of SiO_2, the enthalpy difference required for this phase change can be computed by the built-in thermodynamic library within NASA CEA [56, 57] chemical equilibrium analysis tool. Enthalpy of SiO_2 between 300 K and 1996 K is given in Figure 2.2. The small enthalpy changes between crystalline phase changes of SiO_2 that occur at 848 K and 1200 K are neglected. Following the above discussion, a schematic of the energy fluxes regarding the ablating surface is given in Figure 2.3. The additional terms due to melting ablation are highlighted in red. The explanation of the additional terms are as follows,

1. The term $\dot{m}_c^{''}$ is the energy flux of char entering the surface due to the movement of surface towards the char, which is the dominant term and can be viewed as the enthalpy required to consume unit amount of char. Expanding the char mass flux yields the following expression, which relates the char energy flux to the rate of surface recession.

$$\dot{m}_c^{''} = \dot{s}\rho_c \tag{2.15}$$

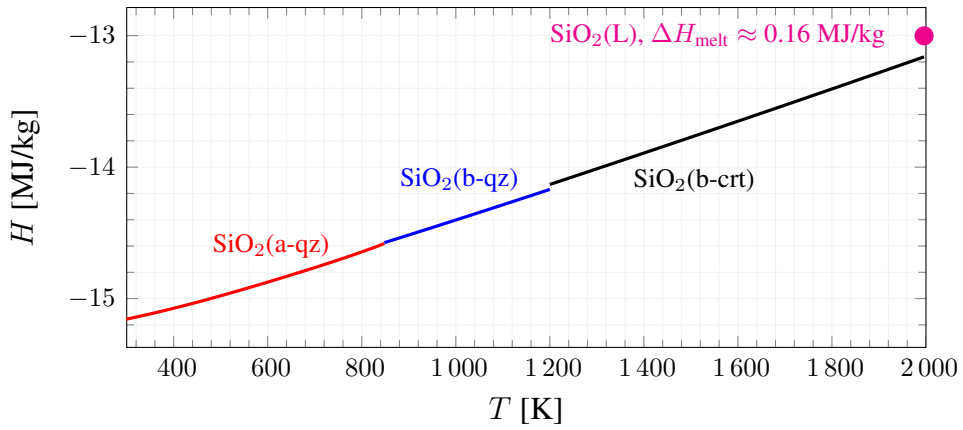

Figure 2.2: Enthalpy of SiO_2.

2. As discussed before, the melting of SiO_2 has been treated as a phenomena that occurs within the surface; acting as a source term.

3. The term $\dot{m}''_f h_c$ is the amount of energy flux leaving due to mechanical removal of the liquid layer, and does not contribute to the surface energy balance. Here $\dot{m}''_f$ denotes the mass flux of material leaving due to the presumed fail removal mechanism, and it is equal to $\dot{m}''_c$.

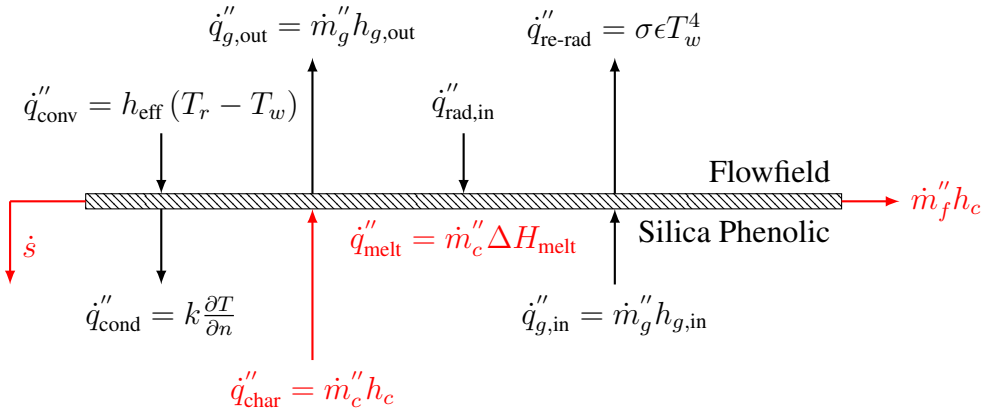

Figure 2.3: Surface energy fluxes for ablating surface.

During melting ablation of silica phenolic, we assume in conjunction with the previous discussion that the surface temperature is equal to that of the melting temperature of SiO_2, which is 1996 K, hence T_w is not an unknown which needs to be determined. Hence, the surface energy balance equation serves to compute the value of $\dot{s}$. If the ablation mechanism in consideration was carbon-phenolic, graphite or carbon-carbon

in which material consumption is due to surface reactions, the surface temperature would still be an unknown that needs to be computed by means of equilibrium surface thermochemistry or kinetics and the amount of gas leaving the surface would include additional terms since ablation products are also gaseous [40].

Now we can construct the equation for surface energy balance for ablating surface as follows,

$$h_{\text{eff}}\,(T_r - T_w) + \dot{s}\rho_c h_c + \dot{m}_{\text{g}}^{''} h_{\text{g,in}} + \sigma\epsilon T_{\text{surr}}^4 = k\frac{\partial T}{\partial n} + \sigma\epsilon T_w^4 + \dot{m}_{\text{g}}^{''} h_w + \dot{s}\rho_c \Delta H_{\text{melt}} \quad (2.16)$$

Resolution of above equation allows for the computation of surface recession rate. As introduced before the surface temperature in this case is equal to the melting temperature of SiO_2, 1996 K. The computation of char enthalpy is required to resolve Equation 2.16 and this is discussed in Section 2.5.

Another point to discuss here is the wall enthalpy, h_{w}. The wall enthalpy is dependent on the local chemical composition at the wall and its thermodynamic conditions dictated by (T, P). The chemical composition at the wall depends on the composition of the injected gases, surface reactions and diffusion of species from flow field. For the ablation mechanism considered here, we are not dealing with surface reactions. Furthermore, to reduce the complexity of problem the effects of species diffusion on the chemical composition at the wall has been neglected and composition of injected gas has been used in computation of h_{w}.

2.2.2 Back Surface

For the treatment of back surface in KAYMAK, no additional surface energy balance is performed and boundary conditions are directly emposed on the cell. The appliable boundary conditions are adiabatic surface, specified heat flux, convection, radiation or combination of convection and radiation. The boundary conditions for these cases are given in as follows,

$$k\frac{\partial T}{\partial n} = 0 \quad (2.17)$$

$$k\frac{\partial T}{\partial n} = q_{\text{bc}}^{''} \quad (2.18)$$

$$k\frac{\partial T}{\partial n} = h\left(T_\infty - T_s\right) + \sigma\epsilon\left(T_{\text{surr}}^4 - T_s^4\right) \tag{2.19}$$

2.3 Pyrolysis Gas Injection

The injection of pyrolysis gas into the boundary layer, so called *blowing* thickens the boundary layer and reduces the effective rate of heat transfer into solid. The reduction is effect is quite significant especially for lower Stanton numbers, where local heating rate is low. In this work, special attention is paid to model this phenomena accurately within CFD environment. The commonly used semi-empirical formulation in literature has also been described and investigated in terms of accuracy.

As discussed before for the silica-phenolic material considered in this work, a melt layer is actually present between gas and solid surface, and injected gas causes bubbles within the molten material and this phenomena and its effects are actually investigated in [14]. However within the analysis presented in this work we have considered the melt layer as an infinitely thin layer and the effect of gas injection on the reduction of heat transfer during melting ablation is modeled as if no melt layer was present. Another quite important point to stress here is that the blowing consists of all the gaseous species injected into the boundary layer. Since our consideration here is limited to silica-phenolic only, the present mechanisms of surface ablation does not involve gaseous ablation products, and hence the only considered gas source is the products of pyrolysis. Certain solid state reactions between SiO_2 and carbonaceous resin residue may produce additional gaseous products but they were neglected due to their complexity and lack of extensive literature. For carbonaceous materials, the blowing may become significantly more important, as the products of surface ablation are also in gaseous form. An extensive amount of literature investigating this effect on graphite, carbon-carbon and carbon phenolic is present. The discussion above also illustrates the point that obtaining an accurate value of gas flux would be quite important for environments characterized with high char thickness and relatively lower heating rates that are present in re-entry environments, which is considered the a main reason why a significant amount of effort is present in literature for modeling pyrolysis gas motion on heatshields that are used on re-entry vehicles.

2.3.1 Semi-Empirical Approach

The semi-empirical approach is based on the blowing rate parameter that is to be computed by

$$\Omega_{\text{blowing}} = \frac{\phi}{e^{\phi} - 1} \tag{2.20}$$

and the effective heat transfer coefficient is then modified accordingly as follows.

$$h_{\text{eff}} = \Omega_{\text{blowing}} h_0 \tag{2.21}$$

here, h_0 stands for the value of heat transfer coefficient in case of zero blowing. Where ϕ appearing in Equation 2.20 is obtained by the following equation.

$$\phi = 2\lambda \frac{\dot{m}''}{\rho_e u_e C_{h,0}} \tag{2.22}$$

The choice of parameter λ is related to the dynamics of boundary-layer. Suggested values in literature is $\lambda = 0.4$ for laminar flow and $\lambda = 0.5$ for turbulent flow. $\dot{m}''$ denotes the mass flux of the injected gas into boundary layer. The formulation in literature is usually given in terms of Stanton number C_h, that relates the convective heat flux and enthalpy difference, whereas in this work a formulation based on convective heat transfer coefficient h has been used. They are related with the following equation,

$$\rho u C_h = \frac{h}{C_p} \tag{2.23}$$

Related work in literature involving surface reactions define the convective heating rate based on enthalpy difference between recovery conditions and conditions that are present on wall, which depends on products of thermochemical ablation process. Since no surface reactions are considered within this work, the usual convective heat transfer coefficient approach has been adopted. Therefore, the implemented form of Equation 2.22 is as Equation 2.23 in terms of convective heat transfer coefficient where $C_{p,e}$ is the value of specific heat capacity of gas at the edge of the boundary layer, i.e mainstream flow at that cross-section. In the following part implementation of this effect within CFD environment and its assessment is detailed.

2.3.2 CFD Implementation and Verification

The approach described in preceding section to describe the decrease in heat transfer coefficient under blowing relies on a semi-empirical approach. If a CFD solution up to the viscous sub-layer can be devised, effects of this phenomena is believed to be realized with better accuracy. This section describes the implementation of blowing boundary condition to commercial CFD software FLUENT and verification of this implementation with available data in literature. Works given in [5, 58] include a verification model for blowing and suction boundary conditions that are implemented in CFD codes LAURA and DPLR that are used by NASA. Both of them perform the verification against the tabulated values of Blasius solution for boundary layer on a flat-plate with suction and blowing tabulated in [6] for various amounts of blowing and suction. Here, we will not describe the Blasius solution with blowing and suction in detail and restrict our attention for the same computational domain described in [5]. The Blasius equation describing the flow over a flat plate is given as follows,

$$f''' + ff'' = 0 \tag{2.24}$$

The blowing or suction boundary condition is introduced to the Blasius equation within the value of $f(0)$ at the wall [6]. Note that negative values of $f(0)$ correspond to the blowing case where positive values are used for suction.

$$\frac{(\rho v)_w}{(\rho u)_\infty} = -\frac{f(0)}{2\sqrt{\mathrm{Re}_x}} \tag{2.25}$$

The term Re_x is the local Reynolds Number on the flat plate evaluated by the local x coordinate where the beginning of the flat plate is considered as $x = 0$.

$$\mathrm{Re}_x = \frac{\rho_\infty u_\infty x}{\mu} \tag{2.26}$$

The value of $(\rho v)_w$ describes the mass flux of gas injected into the boundary layer. As obvious to obtain a constant value of the similarity variable f the amount of blowing depends on the local x coordinate as dictated in Equation 2.25. The verification case described in [5] is illustrated in Figure 2.4. While no details about the boundary conditions other than the value of M_∞ is given in [5], they are deducted to be as follows, $M_\infty = 0.3$, $P_\infty = 101325$ Pa and $T_\infty = 300$ K. Working fluid is air with $\mu = 1.7894 \times 10^{-5}$ kg/m/s, MW = 28.966 g/mol and $C_p = 1006.43$ J/kg/K. Laminar

flow solutions are computed and flat plate is treated as adiabatic. The upwind and downwind extension of the computational domain is to reduce the effects of imposed boundary conditions on the subject flat plate.

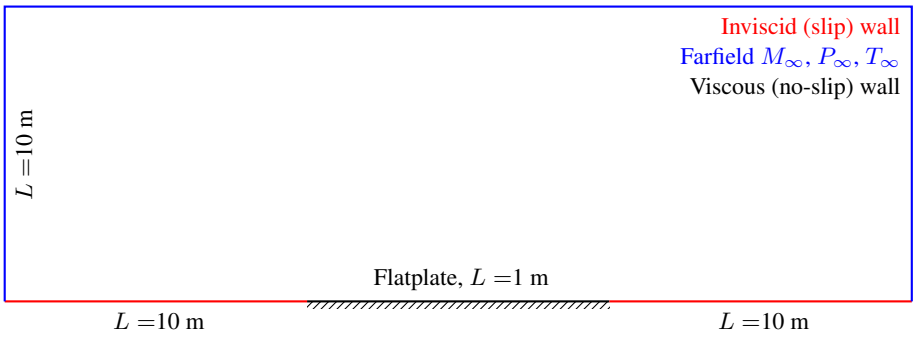

Figure 2.4: Summary of solution domain and boundary conditions for blowing boundary condition verification [5].

When blowing or suction is present at a wall, the local no-slip boundary conditions need to be changed to account that the normal velocity is no longer zero at wall. Since there is no way known to author to change the no-slip wall boundary condition to include this effect on FLUENT, a rather different approach then of described in [5] has been developed with consideration of source terms on the cell adjacent to the wall by means of `DEFINE_SOURCE` UDF's. The mass injection is characterized by mass, normal momentum and energy source terms given by below equation. It has been observed that the lack of energy source term causes the addition of new mass to act as an energy sink and modifies the boundary layer temperature profile in an unphysical way.

$$\begin{aligned} \dot{s}_{\text{mass}} &= (\rho v)_w \, \frac{A_{\text{face}}}{V_{\text{cell}}} \\ \dot{s}_{\text{n-mom}} &= (\rho v)_w \, v_w \, \frac{A_{\text{face}}}{V_{\text{cell}}} \\ \dot{s}_{\text{energy}} &= (\rho v)_w \, h_{\text{inj}} \, \frac{A_{\text{face}}}{V_{\text{cell}}} \end{aligned} \tag{2.27}$$

To evaluate the normal momentum source term given in above equation, value of v_w needs to be computed. This is accomplished by dividing the mass flux term $(\rho v)_w$ with the local value of density obtained by means of flow field solution. The approach illustrated here can be used to model gas injection into boundary layer in a flexible manner such that injections with any enthalpy can be realized. FLUENT solutions are

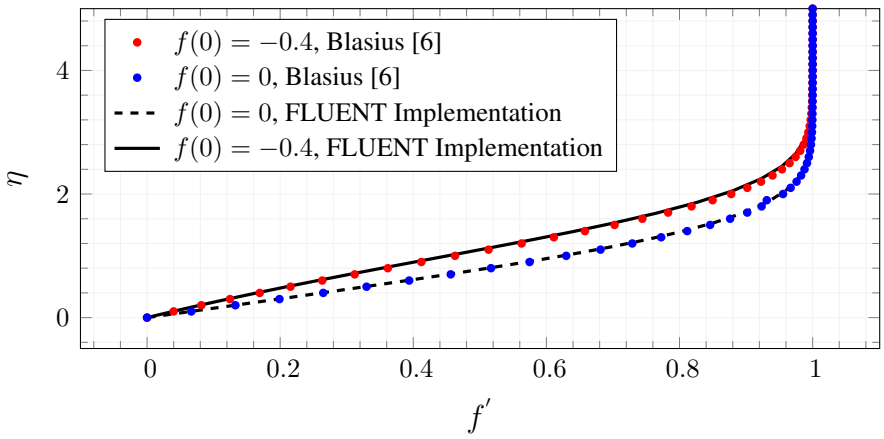

Figure 2.5: Comparison of results at $x = 0.5$ with tabulated data obtained from [6].

carried on until residuals are flattened and excellent convergence has been obtained for both solutions presented here. Density based implicit solver with Roe's Flux and second order spatial discretization has been used on a grid system clustered near flat plate with $\Delta s = 1\mu$m near wall. The results are given in Figure 2.5.

Figure 2.5 illustrates an excellent agreement between analytical Blasius solution and devised boundary condition implementation within FLUENT. Thickening of the boundary layer is also obvious observing the value of η. It appears that a slightly better agreement than of [5] has been obtained.

2.3.3 Comparison of Semi-Empirical Approach and CFD

With the verification of the developed boundary condition for blowing in previous section, the accuracy of the semi-empirical formulation can be assessed. The case described in preceding section has been employed by considering the flat plate as a constant 250 K temperature wall, and solutions are carried out with same parameters for no blowing and a for a spatially varying blowing rate corresponding to $f(0) = -0.4$ as illustrated in the previous section. The temperature of the injected gas has been considered as equal to the constant wall temperature 250 K.

The values of heat flux, heat transfer coefficient as evaluated by FLUENT and corresponding values of Ω_{blowing} are compared throughout the length of flat plate. Since laminar flow is considered, $\lambda = 0.5$ has been used in Equation 2.22 suggested in

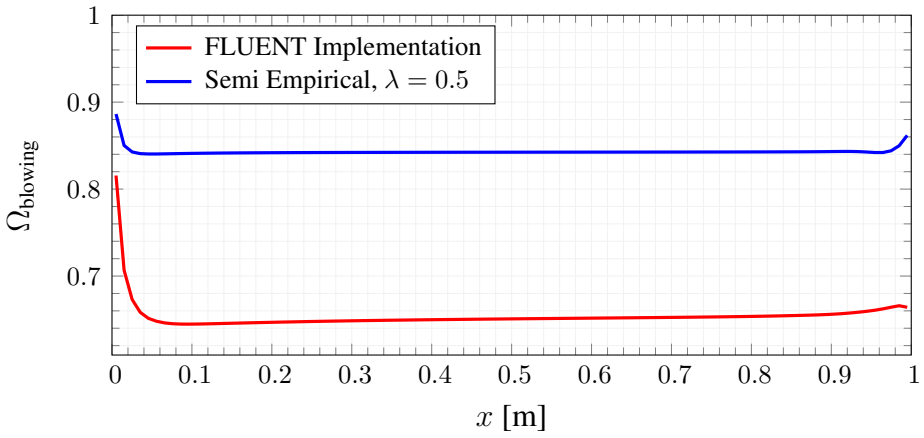

Figure 2.6: Comparison of Ω_{blowing} values.

literature. Comparison of results are given in Figure 2.6. Although the value of Reynold's Number for the case illustrated in [5] and reproduced here correspond to a high Reynold's Number, which exceeds the regime of laminar flow, this issue will not be discussed further since the main goal of this chapter is to follow the same approach given in [5]. As shown in Figure 2.6, there is a significant difference between CFD results and semi-empirical blowing correlation in which the correlation under predicts the amount of heat transfer coefficient reduction. It has been observed that a value of λ about 1.2 produces nearly identical results. It can also be observed that towards the beginning and the end of flat plate the local values are disturbed by freestream conditions and Ω_{blowing} attains an approximately constant value at the inner regions of the flat plate.

2.4 Computation of Local Material Properties

As discussed in previous sections, the material is described as a mixture of virgin and charred states locally. The common approach in literature which has been used successfully is to describe the specific heat capacity and thermal conductivity of the material by means of a mixture law based on local virgin and char content. While there are more complicated functional forms for these relations appear in literature, the basic linear mixture form has been used in this work. A degradation parameter, x

defined by below expression is introduced to represent the state of material.

$$x = \frac{\rho - \rho_{\mathrm{c}}}{\rho_{\mathrm{v}} - \rho_{\mathrm{c}}} \tag{2.28}$$

Based on this definition, the local values dependent on the degradation state of material are computed. Computation of thermal conductivity and specific heat capacity is carried out as given below,

$$k = xk_{\mathrm{v}} + (1 - x)\, k_{\mathrm{c}} \tag{2.29}$$

$$C_{\mathrm{p}} = xC_{\mathrm{p,v}} + (1 - x)\, C_{\mathrm{p,c}} \tag{2.30}$$

The values of virgin and char thermal conductivities and specific heats are temperature dependent.

2.5 Computation of Enthalpies

Computation of enthalpy values and gas properties can be performed by means of chemical equilibrium computations as illustrated in [17, 19]. The starting assumption of this section is that the resin is composed of the phenol molecule, C_6H_6O and reinforcement is composed of SiO_2. Any other ingredients and their contributions are neglected as they are assumed to occupy negligible amount of mole fraction within material.

A further assumption is that resin and the carbonaceous char produced from pyrolysis of resin do not chemically interact with SiO_2, which may occur and related work can be found in [19, 59]. This assumption allows for separate treatment of pyrolysis reaction and its gaseous products. Chemical equilibrium calculations indicate that these reactions mainly involve consumption of solid carbon and production of condensed SiC and gaseous SiO, and they begin to dominate at temperatures close to the melting temperature of SiO_2 that is 1996 K. This would obviously affect a thin zone near the receding surface, and also violate the computational method of energy balance, specific heat capacity, density and thermal conductivity calculations introduced in the preceding sections. It is also another question that if these carbon-silica reactions reach equilibrium or their kinetics need to be taken into account within the timescale

of the problem. Some kinetics data is also present in [19], however since implementation of silica - carbon reactions for the problem considered in this thesis is not yet common in literature, such an attempt has not been made here.

Based on the previous discussion in the related sections, the key points are to determine the enthalpy of char and heat of pyrolysis which depends on the enthalpy difference between pyrolysis gas and solid material. To proceed, the following information should be readily available,

1. The resin mass fraction, Γ_M or volume fraction Γ_V. Conversion between them is possible by Equations 2.9 and 2.8.

2. Virgin material density, ρ_v and charred material density ρ_c. Char density can also be theoretically computed with also required resin model. Computation of effective reinforcement density can be accomplished by,

$$\rho_R = \frac{\rho_{\text{v}} \left(\rho_{0,\text{A}} + \rho_{0,\text{B}}\right) \left(\frac{1}{\Gamma_M} - 1\right)}{\frac{\left(\rho_{0,\text{A}} + \rho_{0,\text{B}}\right)}{\Gamma_M} - \rho_{\text{v}}} \tag{2.31}$$

3. A model for the resin including $\rho_{0,\text{A}}$ and $\rho_{0,\text{B}}$. In this thesis no additional attempt has been made to characterize the kinetics of phenol, instead values given in [1, 19] has been employed and these are observed to be almost identical.

4. Enthalpy information for C_6H_6O and SiO_2, or heat of formation for virgin and charred states plus C_p for the temperature range in consideration. For the theoretical calculations presented here, the species enthalpy data present in the library of NASA CEA [56, 57] in polynomial forms has been employed.

For the equilibrium computations presented here, only species with molar fractions greater than 0.0001 has been considered. We begin with computing the mass fractions of C_6H_6O and SiO_2 based on Γ_M as follows,

$$H_{\text{v}} = H_{\text{C}_6\text{H}_6\text{O}} \Gamma_M + \left(1 - \Gamma_M\right) H_{\text{SiO}_2} \tag{2.32}$$

The commonly used phenolic model in literature considers a carbon residual fraction of 0.4 per unit mass of resin, and this value is adopted for the computation of char

enthalpy. The resin residual mass fraction can be obtained or verified from the resin model data by,

$$y_{\text{C,resin}} = \frac{\rho_{\text{r,B}}}{\rho_{\text{0,A}} + \rho_{\text{0,B}}} \tag{2.33}$$

considering that the residue carbon from resin and SiO_2 reinforcement do not decompose, the char constitutes of SiO_2 and C. Hence the char enthalpy can be computed by,

$$H_{\text{c}} = H_{\text{C}} \frac{y_{\text{C,resin}} \Gamma_M}{1 + (y_{\text{C,resin}} - 1)\,\Gamma_M} + H_{\text{SiO}_2} \frac{1 - \Gamma_M}{1 + (y_{\text{C,resin}} - 1)\,\Gamma_M} \tag{2.34}$$

The char enthalpy computed in this fashion at the melting temperature of SiO_2 is also to be used in Equation 2.16, hence surface recession rate is pretty sensitive to this value. As defined previously in Equations 2.7 and 2.6, pyrolysis gas enthalpy needs to be computed within the temperature range of interest. For this, constituents of pyrolysis gas with mass fractions shall be known. Based on equilibrium computations performed on C_6H_6O this data can be approximated, however it has been observed that the pyrolysis gas composition - hence its enthalpy - has a certain dependence on pressure. Since in-depth internal gas flow model included in this work does not yield any information regarding the internal pressure of the pyrolysis gas, further assumptions are necessary at this point.

In [1], enthalpy data for virgin, char and pyrolysis gas are explicitly given for a wide temperature range for a silica phenolic with Γ_V =0.422 which corresponds to a Γ_M value of 0.3146 in accordance with the other parameters given in [1]. However no information is present related to the source of enthalpies of formation or the method of computation for enthalpies. Nevertheless, since this is among the only such data source available in literature within the knowledge of the author, a comparison is presented. Another source of data for temperature dependent data for pyrolysis gas is also present in [2] and these values are also included in comparison given in Figure 2.7. As illustrated in Figure 2.7, quite good agreement has been observed for virgin and char densities obtained from [1] and computed here according to parameters specified. A larger discrepancy is present for char enthalpy, however it is hard to perform a discussion since no information regarding this computation is present in [1]. For pyrolysis gas enthalpy, serious discrepancy is present for lower temperatures. The decrease of gas enthalpy with increasing pressure is in agreement with additional data present in [2]. It can also be observed that values obtained from different sources are

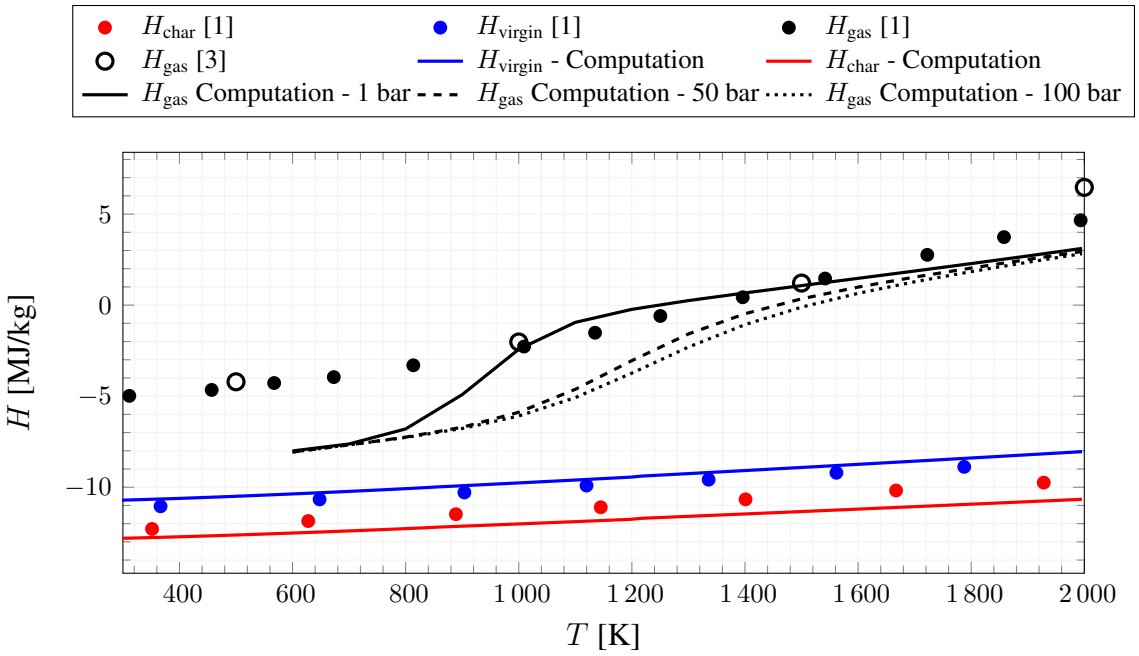

Figure 2.7: Comparison of computed enthalpies with data available in literature. Solid lines represent computed values.

almost identical, hence for the computations to be presented in the following sections values for gas enthalpy given in [1] will be used instead of the computationally obtained ones. The reason for this discrepancy is most probably related to the way the chemical equilibrium computations are performed. It is stated in [2] that gas enthalpy was obtained by means of equilibrium computations involving certain assumptions regarding the inallowance of condensed carbon to precipitate, however attempts to reproduce the gas enthalpy by omitting condensed carbon in equilibrium computations did not introduce better agreement.

2.6 Summary of Required Material Data

As there is a plenty amount of data required to conduct an analysis based on foundations described in the preceding sections, this section has been included to present a brief summary of required as required by the models introduced in this chapter. To model pyrolysis gas injection in a CFD coupled analysis, values of molecular weight, viscosity and specific heat capacity are also required.

Table 2.1: Summary of required parameters.

Parameter	**Explanation**
$k_{\mathrm{v}}(T)$	Virgin thermal conductivity vs. temperature
$k_{\mathrm{c}}(T)$	Char thermal conductivity vs. temperature
$C_{p,\mathrm{v}}(T)$	Virgin specific heat capacity vs. temperature
$C_{p,\mathrm{c}}(T)$	Char specific heat capacity vs. temperature
$h_{\mathrm{v}}(T)$	Virgin enthalpy vs. temperature
$h_{\mathrm{c}}(T)$	Char enthalpy vs. temperature
$h_{\mathrm{gas}}(T)$	Pyrolysis gas enthalpy vs. temperature
$\rho_{0,\mathrm{A}}$, $\rho_{0,\mathrm{B}}$, $\rho_{\mathrm{r,A}}$, $\rho_{\mathrm{r,B}}$, ρ_{R}	Resin constituent densities
A_j, E_j, n_j	Resin decomposition model constants
Γ_M or Γ_V	Resin mass or volume fraction
$\epsilon_{\mathrm{v}}(T)$	Virgin emissivity vs. temperature
$\epsilon_{\mathrm{c}}(T)$	Char emissivity vs. temperature

CHAPTER 3

DEVELOPMENT OF KAYMAK

KAYMAK has been developed to include certain features that are present in CMA3 [23], such as analysis with pre-specified surface temperature & regression rate, implementation of Bartz equation for estimation of convective heat transfer rate, and perform analysis with presence of a non-charring backup material, and analysis capability for cool-down period in which SRM firing duration is over and boundary conditions are different.

KAYMAK is a 1D analysis tool that is also applicable to axisymmetric domains. It is based on discretization of governing equations with finite volume method of first order spatial accuracy on a uniform stretching dynamic grid scheme. Time integration is performed in a semi-implicit manner as only diffusion of heat is treated implicit in time to enhance stability and decrease overall computational time required. In this section, numerical implementation of previously discussed theoretical foundation is detailed.

3.1 Discretization of Governing Equations

The governing equations are discretized in a 1D finite volume solution domain with a regular grid system. Required user input is the extent of domain and backup material if present, and number of cells. Axisymmetric analysis capability is introduced within usage of Equations 3.4 and 3.5 for computation of cell volumes and face areas. For pure 1D analysis values of A_i are equal to unity and V_i is equal to Δr. Following

algebraic equations are employed for grid generation,

$$\Delta r = \frac{r_{\max} - r_{\min}}{n_{\text{cells}}} \tag{3.1}$$

$$r_i = r_1 + \Delta r\,(i-1) \tag{3.2}$$

$$r_{ci} = \frac{r_{i+1} + r_i}{2} \tag{3.3}$$

$$A_i = 2\pi r_i \tag{3.4}$$

$$V_i = \pi\left(r_{i+1}^2 - r_i^2\right) \tag{3.5}$$

The main equation to be solved is the conservation of energy previously defined in Equation 2.1. For sake of clarity it is repeated below,

$$\frac{\partial}{\partial t}\int_V (\rho C_p T)\,dV = \oint_S k\nabla T \cdot d\mathbf{S} + \oint_S (\rho C_p T)\,\mathbf{v}_s \cdot d\mathbf{S} + \int_V \dot{s}dV \tag{3.6}$$

Employing the finite volume method and representing the gradient of temperature at faces by first order forward and backward differences, spatially discretized form of the energy equation can be obtained as follows,

$$\begin{aligned}(\rho V C_p)_i \frac{\partial T_i}{\partial t} + (\rho C_p T)_i \frac{\partial V_i}{\partial t} = \frac{A_{i+1/2}k_{i+1/2}}{r_{c_{i+1}} - r_{c_i}}(T_{i+1} - T_i) - \frac{A_{i-1/2}k_{i-1/2}}{r_{c_i} - r_{c_{i-1}}}(T_i - T_{i-1}) \\ + u_{i+1/2}A_{i+1/2}\,(\rho C_p T)_{i+1/2} - u_{i-1/2}A_{i-1/2}\,(\rho C_p T)_{i-1/2} + \dot{S}_i\end{aligned} \tag{3.7}$$

The values defined at locations $i + 1/2$ and $i - 1/2$ represent the values at north and south faces respectively. Value of thermal conductivity at faces are obtained by simple averaging as given below,

$$\begin{aligned}k_{i+1/2} &= \tfrac{1}{2}(k_i + k_{i+1}) \\ k_{i-1/2} &= \tfrac{1}{2}(k_i + k_{i-1})\end{aligned} \tag{3.8}$$

However for the face value of convected enthalpy due to grid motion simple averaging is not suitable with the physics of the problem and instead upwinding needs to be employed. That is, the face value shall be represented based on the flow direction,

dictated by the local direction of grid velocity. Since the contraction of grid system only consists of velocities towards the north face, the required values are obtained as follows,

$$\begin{aligned}(\rho C_p T)_{i+1/2} &= (\rho C_p T)_{i+1} \\ (\rho C_p T)_{i-1/2} &= (\rho C_p T)_{i}\end{aligned} \tag{3.9}$$

We now introduce the temporal discretization by approximating the time derivative of temperature with a first order forward difference and evaluating the conductive terms at unknown time step $n+1$. It is also possible to use the $n+1$ values for grid convection terms without affecting the tridiagonal form that will be obtained; however, since grid velocity is related to surface energy balance and this will be implemented in an explicit fashion these terms are also considered in an explicit fashion for consistency. The source term is also expanded as an explicit and implicit part as defined below,

$$S = S_u + S_p T \tag{3.10}$$

with the inclusion of source term discretization, the overall discretized form of energy equation is as follows,

$$\begin{aligned}(\rho V C_p)_i^n \frac{T_i^{n+1} - T_i^n}{\Delta t} + (\rho C_p T)_i^n \frac{V_i^{n+1} - V_i^n}{\Delta t} = \\ \frac{A_{i+1/2}^n k_{i+1/2}^n}{r_{c_{i+1}}^n - r_{c_i}^n}\left(T_{i+1}^{n+1} - T_i^{n+1}\right) - \frac{A_{i-1/2}^n k_{i-1/2}^n}{r_{c_i}^n - r_{c_{i-1}}^n}\left(T_i^{n+1} - T_{i-1}^{n+1}\right) \\ + u_{i+1/2}^n A_{i+1/2}^n \left(\rho C_p T\right)_{i+1/2}^n - u_{i-1/2}^n A_{i-1/2}^n \left(\rho C_p T\right)_{i-1/2}^n + S_{u_i} + S_{p_i} T_i^{n+1}\end{aligned} \tag{3.11}$$

Defining the source term in an implicit and explicit part is useful in terms of enhancement of stability and compactness of the implementation. All explicit terms can be included in the definition of S_u. Nonlinear source terms can be linearized in time as follows to allow implicit computation,

$$S^{n+1} = S^n + \left.\frac{\partial S}{\partial T}\right|^n \left(T^{n+1} - T^n\right) \tag{3.12}$$

S_u and S_p for a particular source term can be derived by employing above equation.

Introducing the following definitons to allow a compact notation,

$$\begin{aligned}\beta &= \tfrac{\rho_i V_i C_{p_i}}{\Delta t} \\ \alpha_n &= A_{i+\frac{1}{2}} \tfrac{k_{i+1}+k_i}{2\left(r_{c_{i+1}} - r_{c_i}\right)} \\ \alpha_s &= A_{i-\frac{1}{2}} \tfrac{k_i+k_{i-1}}{2\left(r_{c_i} - r_{c_{i-1}}\right)}\end{aligned} \tag{3.13}$$

based on these definitions and the definition of source terms, Equation 3.11 can be reduced to the following compact form,

$$a_i T_{i-1}^{n+1} + b_i T_i^{n+1} + c_i T_{i+1}^{n+1} = d_i \tag{3.14}$$

where the coefficients a_i, b_i, c_i and d_i are defined as given below.

$$a_i = -\frac{\alpha_s}{\beta} \tag{3.15}$$

$$b_i = \frac{\beta + \alpha_n + \alpha_s - S_p}{\beta} \tag{3.16}$$

$$c_i = -\frac{-\alpha_n}{\beta} \tag{3.17}$$

$$d_i = T_i + \frac{S_u}{\beta} \tag{3.18}$$

As mentioned before all explicit contributions are to be included within the term S_u. These contributions are due to grid convection, heat of pyrolysis and pyrolysis gas source terms.

$$S_u = S_{u,\text{gc}} + S_{u,\text{gas}} + S_{u,\text{pyr}} \tag{3.19}$$

From Equation 3.11 and discussion related to the computation of face value of the convected enthalpy, the source terms due to grid convection are as follows,

$$S_{u,\text{gc}} = u_{i+1/2}^n A_{i+1/2}^n \left(\rho C_p T\right)_{i+1}^n - u_{i-1/2}^n A_{i-1/2}^n \left(\rho C_p T\right)_i^n - \left(\rho C_p T\right)_i^n \frac{V_i^{n+1} - V_i^n}{\Delta t} \tag{3.20}$$

The last term is related to the rate of element volume change is computed at the beginning of each time step considering the grid at time levels n and $n+1$.

The source term due to heat of pyrolysis is computed by,

$$S_{u,\text{pyr}} = \Delta H_{\text{pyr}}|_{T_i^n} \left.\frac{\partial \rho}{\partial t}\right|_i^n V_i^n \tag{3.21}$$

and finally the source term due to pyrolysis gas is computed as follows,

$$S_{u,\text{gas}} = \dot{m}_{\text{gas},i} \left(h_{\text{gas}}|_{i+1} - h_{\text{gas}}|_i \right) \tag{3.22}$$

where mass flow rate of pyrolysis gas at any cell is computed by,

$$\dot{m}_{\text{gas},i} = \sum_{j=i+1}^{i_{\max}} -\left.\frac{\partial \rho}{\partial t}\right|_j^n V_j^n \tag{3.23}$$

Above equation simply states that the pyrolysis gas flowing through a particualar cell is equal to the sum of pyrolysis gas generated above that cell in conjunction with the no accumulation&zero residence time assumption defined before. Minus sign is due to the fact that rate of change of density is a negative value.

It can be realized from Equation 3.14 that if it is written for each cell within the domain, an algebraic system of equations given as below can be formed,

$$\tilde{\mathbf{A}}^n \mathbf{T}^{n+1} = \mathbf{d}^n \tag{3.24}$$

and a tridiagonal coefficient matrix is formed which is illustrated in for a 5×5 system below,

$$\begin{bmatrix} b_1 & c_1 & 0 & 0 & 0 \\ a_2 & b_2 & c_2 & 0 & 0 \\ 0 & a_3 & b_3 & c_3 & 0 \\ 0 & 0 & a_4 & b_4 & c_4 \\ 0 & 0 & 0 & a_5 & b_5 \end{bmatrix}^n \begin{bmatrix} T_1 \\ T_2 \\ T_3 \\ T_4 \\ T_5 \end{bmatrix}^{n+1} = \begin{bmatrix} d_1 \\ d_2 \\ d_3 \\ d_4 \\ d_5 \end{bmatrix}^n \tag{3.25}$$

this system is numerically solved for $\mathbf{T}^{n+1}$ at each time step with the efficient Thomas Algorithm commonly employed for tridiagonal systems.

To obtain the values for source terms, we now consider the numerical treatment of conservation of mass. Since the density of the material at any given location is a linear combination of ρ_j at that location, the conservation equations for each decomposing component has been considered with appropriate terms for grid convection. The corresponding conservation equation is repeated here for sake of clarity.

$$\frac{\partial}{\partial t}\int_V \rho_j dV = \int_S \rho_j \mathbf{v}_s \cdot d\mathbf{A} + \int_V \dot{s} dV \quad \text{where} \quad j = A, B \tag{3.26}$$

With application of finite volume discretization the spatially discretized form of conservation of mass is obtained as follows,

$$\frac{\partial \rho_{j_i}}{\partial t} V_i + \frac{\partial V_i}{\partial t} \rho_{j_i} = (\rho_j u)_{i+1/2} A_{i+1/2} - (\rho_j u)_{i-1/2} A_{i-1/2} + \dot{S}_j \tag{3.27}$$

where the source term here is the rate of consumption of component j due to pyrolysis reactions and is given by below equation.

$$\dot{S}_j = -\left(\rho_{0,j} - \rho_{r,j}\right)\left(\frac{\rho_j - \rho_{r,j}}{\rho_{0,j} - \rho_{r,j}}\right)^{n_j} A_j e^{\frac{-E_j}{RT}} \quad \text{where} \quad j = A, B \tag{3.28}$$

Employing a first order forward temporal discretization, evaluating other quantities at the known time step n and considering the upwind evaluation of face values related to grid convection yields an explicit formulation for conservation of mass as follows,

$$\rho_{j_i}^{n+1} = \rho_{j_i}^{n} + \dot{S}_{j_i}^{n}\Delta t + \frac{\Delta t}{V_i}\left[\rho_{j_{i+1}}\left(uA\right)_{i+1/2} - \rho_{j_i}\left(uA\right)_{i-1/2}\right] - \frac{\dot{V}_i \rho_{j_i}}{V_i} \tag{3.29}$$

Equation 3.29 and 3.24 are solved at each time step to successfully update the main solution variables T_i and ρ_{j_i}. So far only the grid velocity terms defined at faces are left to define and this is detailed in Section 3.3.

3.2 Boundary Conditions

In this section, numerical treatment for boundary conditions are detailed.

3.2.1 Surface Energy Balance

As discussed in previous chapter, surface energy balance is investigated for two different phases: stationary and ablating surface. Switching between these two are done by means of monitoring the surface temperature. If it exceeds the value of T_{abl}, ablating surface mode is activated and surface recession occurs. If at any time step the net heat flux driving the ablation becomes negative program switches back to the stationary surface mode.

Since the output of surface energy balance approach yields a surface temperature value, the implication of this boundary condition into the domain occurs via the conductive heat transfer rate between the surface and the first cell of domain. As the surface energy balance computation is done explicitly in time, the implementation of the boundary condition for the first cell has been done by modifying the source term S_u defined in the preceding section as illustrated below,

$$S_{u_1} = S_{u,\text{gc}} + S_{u,\text{gas}} + S_{u,\text{gas}} + k_1 A_{1/2}\frac{(T_w - T_1)}{r_{c_1} - r_1} \tag{3.30}$$

with this implementation the value of α_s, representing the implicit contribution of conductive heat flux from south face is set to zero for the first cell.

3.2.1.1 Stationary Surface

A schematic for the surface energy balance of the stationary surface case, corresponding to heating or cooldown phases is previously given in Figure 2.1. The previously derived surface energy balance Equation 2.14 is repeated below for clarity.

$$h_{\text{eff}}\left(T_r - T_w\right) + \dot{m}_g^{''}\left(h_{\text{g,in}} - h_w\right) + \sigma\epsilon_w\left(T_{\text{surr}}^4 - T_w^4\right) - k\frac{\partial T}{\partial n} = 0 \tag{3.31}$$

Where h_{eff} represents the effective convective heat transfer coefficient including the effects of blowing as discussed in Section 2.3.1. For the heating or cooldown phases, the surface temperature is an unknown and needs to be deducted from surface energy balance. This boundary condition for static surface can also be directly applied to the first cell adjacent to the surface, however this type of treatment allows direct monitoring of surface temperature and treats it as a solution variable, increasing accuracy and consistency with the ablating surface case.

As can be observed from Equation 2.14, the equation is nonlinear in terms of T_w and no analytical solution is present, hence an iterative solution needs to be performed. First we obtain the discretized form by replacing the temperature gradient with a backward difference approximation to obtain the following,

$$h_{\text{eff}}\left(T_r - T_w\right) + \dot{m}_g^{''}\left(h_{\text{g,in}} - h_w\right) + \sigma\epsilon_w\left(T_{\text{surr}}^4 - T_w^4\right) - k_s\frac{T_w - T_1}{r_{c_1} - r_1} = 0 \tag{3.32}$$

this equation can be cast in the following general form which is to be solved with Newton-Raphson iterative method.

$$f = A + BT_w + CT_w^4 = 0 \tag{3.33}$$

The coefficients are as follows,

$$\begin{aligned} A &= h_{\text{eff}}T_r + \tfrac{k_s}{r_{c_1} - r_1}T_1 + \sigma\epsilon_w T_{\text{surr}}^4 + \dot{m}_{\text{g}}^{''}\left(h_{\text{g,1}} - h_w\right) \\ B &= -h_{\text{eff}} - \tfrac{k_s}{r_{c_1} - r_1} \\ C &= -\sigma\epsilon_w \end{aligned} \tag{3.34}$$

Note that while the enthalpy of pyrolysis gas required to evaluate h_w and $h_{g,1}$ terms are also dependent on the surface temperature. To avoid further complications, values of gas enthalpy based on the value of surface temperature from previous time step has been used.

Newton-Raphson method is one of the most commonly used methods for solving nonlinear equations if analytical derivative is available. Below equation 3.35 is employed for successive iterations until difference between T_w^{k+1} and T_w^k drops below a specified tolerance.

$$T_w^{k+1} = T_w^k - \frac{f(T_w^k)}{f'(T_w^k)} \tag{3.35}$$

An initial guess needs to be supplied and this may affect the convergence point based on the local behavior of derivative. The supplied initial value is the value of T_w at previous time step. The superscript k denotes the iteration number and derivative of f with respect to T_w is obtained from differentiating Equation 3.33.

3.2.1.2 Ablating Surface

Within consideration of melting ablation mechanism at constant temperature, the value of surface temperature is no longer an unknown and the surface energy balance equation now serves to compute the value of surface recession rate. For other ablation mechanisms as discussed in previous sections, material consumption is related to the surface thermochemical conditions. For these cases the surface temperature is still an unknown and additional information relating the consumption of condensed surface material to the temperature of surface needs to be supplied in order to obtain a closure and satisfy surface energy balance equation. While the case investigated in this work does not cover these type of mainly carbon based materials, KAYMAK includes the necessary provisions to include this type of surface energy balance in a future release without changing the main structure of the code.

One of the reasons for explicit treatment of surface energy balance is due to the fact that the value of grid velocities defined on faces are dependent of the rate of surface recession and a tridiagonal system of equations can no longer be formed, an additional column of coefficients appear destroying the diagonal structure and requires more

expensive numerical treatment, as illustrated in [7]. The previously derived Equation 2.16 for surface energy balance on an ablating surface is repeated below for clarity.

$$h_{\text{eff}}\left(T_r - T_w\right) + \dot{s}\rho_c h_c + \dot{m}_{\text{g}}^{''} h_{\text{g,in}} + \sigma\epsilon T_{\text{surr}}^4 - k\frac{\partial T}{\partial n} - \sigma\epsilon T_w^4 - \dot{m}_{\text{g}}^{''} h_w - \dot{s}\rho_c \Delta H_{\text{melt}} = 0 \tag{3.36}$$

As discussed, the surface temperature is a known value for this case and it is equal to T_{abl}. Substituting this value and rearranging the equation as done in preceding section yields the following,

$$\dot{s} = \frac{\overbrace{h_{\text{eff}}\left(T_r - T_w\right)}^{\dot{q}_{\text{conv}}^{''}} - \overbrace{\dot{m}_g^{''}\left(h_w - h_{\text{g,in}}\right)}^{\dot{q}_{\text{gas}}^{''}} - \overbrace{\sigma\epsilon_w\left(T_w^4 - T_{\text{surr}}^4\right)}^{\dot{q}_{\text{re-rad}}^{''}} - \overbrace{k\frac{T_{\text{abl}} - T_1}{r_{c_1} - r_1}}^{\dot{q}_{\text{cond}}^{''}}}{\rho_c\left(\Delta H_{\text{melt}} - h_c^{1996}\right)} \tag{3.37}$$

The resolution of surface recession rate is obtained by above equation and value of char enthalpy h_c is computed at T_{abl} =1996 K. The value of $\Delta H_{\text{melt}} - h_c$ when h_c is evaluated at melting temperature of SiO_2 can be thought as analogous to the value of Q^*, defined as heat of ablation for the simple heat of ablation model commonly used in literature. Note that h_c has a negative value and computed as follows,

$$h_c^{1996} = \Delta H_{f,c}^{298} + \int_{\text{T=298}}^{\text{T=1996}} C_{p,c}(T)dT \tag{3.38}$$

The status of surface is tracked within KAYMAK and if the numerator of Equation 3.37 becomes negative, KAYMAK switches back to the stationary surface mode.

3.2.2 Back Surface

The treatment of back surface boundary conditions is rather straightforward as the boundary conditions are directly applied to the last cell of the domain and no additional surface energy balance is employed. While this is a possibility that can easily be implemented, it has not been deemed necessary to include.

The implementation of back surface boundary conditions introduced in Section 2.2.2 are done by means of source terms S_u and S_p defined in the preceding section, and they are implemented in an implicit manner. Also it has to be mentioned here that

the pyrolysis gas source term for the last cell of the domain is zero even the analysis in hand consists of no backup material defined and last cell also represents charring ablator. Reason for that is obviously there is no incoming pyrolysis gas flux to the last cell.

3.2.2.1 Adiabatic wall

The value of coefficient α_n is simply set to zero for last cell and this represents the adiabatic condition where no heat flux is present at the north face of last cell.

3.2.2.2 Convection and radiation

This is the main boundary condition that will be used for practical purposes, and it has been implemented implicitly through linearization of corresponding terms. The convective heat transfer rate at the north face of last cell is computed as follows,

$$q^{'}_{\text{conv}} = hA_{i_{\text{max}}} \left(T_{\infty} - T_{i_{\text{max}}}\right) \tag{3.39}$$

similarly, radiative heat transfer rate is computed by,

$$q^{'}_{\text{rad}} = \sigma\epsilon A_{i_{\text{max}}} \left(T^4_{\text{surr}} - T^4_{i_{\text{max}}}\right) \tag{3.40}$$

Linearization of above equations as defined in Equation 3.12 yields the final source terms S_u and S_p for the last cell as given below.

$$\begin{aligned} S_u &= S_{u,\text{gc}} + S_{u,\text{pyr}} + hA_{i_{\text{max}}+1/2}T_{\infty}A_{i_{\text{max}}+1/2}\sigma\epsilon\left(3T^{n^4}_{i_{\text{max}}} + T^4_{\text{surr}}\right) \\ S_p &= -hA_{i_{\text{max}}+1/2} - 4A_{i_{\text{max}}+1/2}\sigma\epsilon T^{n^3}_{i_{\text{max}}} \end{aligned} \tag{3.41}$$

3.3 Dynamic Grid Scheme

The problem of ablation obviously needs to be solved in a dynamic grid scheme as the extent of solution domain decreases in time. The main requirement for the selection of dynamic grid scheme can be defined as accuracy and robustness. Grid deformation algorithms can be roughly investigated in two main classes as node/cell dropping schemes and contracting/expanding grid schemes.

During development of KAYMAK both of these methods have been implemented, first one being the initial consideration as it requires less implementation effort and does not introduce grid convection terms to governing equations. However due to considerable inaccuracies caused by this implementation led to the replacement of grid scheme algorithm to a contracting grid scheme, and the code has been practically rewritten due to core structural changes. In this section a brief comparison is made between these two approaches and details of implementation are presented.

The first implementation was based on the method illustrated in [60]. As surface recession commences, only the cell adjacent to surface was deformed, hence no additional terms related to grid convection is necessary for this approach. Obviously after a certain amount of deformation the first cell and the second cell needs to be merged, and properties of the new formed cell, which will become the first cell needs to be determined. That is the point prone to certain problems. A simple volumetric average for any property ϕ was computed as follows,

$$\phi_{1-2} = \frac{V_1\phi_1 + V_2\phi_2}{V_1 + V_2} \tag{3.42}$$

the artificially formed properties this way caused some disturbing behavior near the surface as illustrated in Figure 3.1 for an earlier solution. While no considerable effect occurs on the total amount of surface recession, this is has been considered as not a suitable approach within the defined requirements for dynamic grid scheme.

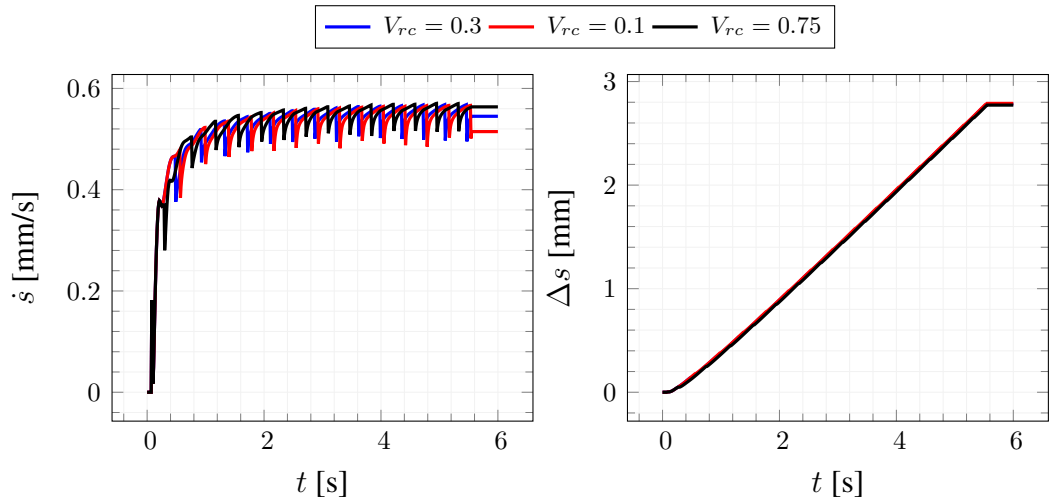

Figure 3.1: Illustration of side effects observed with cell dropping scheme.

In Figure 3.1, V_{rc} stands for the volume ratio of first and second cells that has been

used as a threshold value to merge them. As discussed in first chapter, one of the most complete and numerically sophisticated 1D analysis tool encountered in literature is [7]. While requires more effort, the contracting grid scheme illustrated in [7] is perhaps the numerically best method for this kind of problem, reasons for which is explained below.

The scheme involves a Landau coordinate system transform resulting as the distance between cells stay constant as the grid stretches, which forms the basis for the method. While various other methods can be suggested to define face velocities, this method is unique in terms of the selection of face velocities. Keeping the face - cell center distance same for adjacent cells is beneficial in terms of numerical accuracy as no further interpolation error is introduced for the computation of face values. Note that in this scheme the total number of cells stay constant, and apparent value of Δr decreases throughout analysis; whereas for the first method discussed the number of cells is decreasing, Δr is constant for static cells and size of the system of linear algebraic equations to be solved decreases after each cell merger operation.

Based on definitions in Figure 3.2, the Landau coordinate η is obtained by the following equation for each face,

$$\eta_i = \frac{L_0 - z_i}{L_0 - s_{\text{total}}} \tag{3.43}$$

As shown in Figure 3.2, grid motion is limited to the part of domain occupied by the charring ablator only. Once values of η_i at all moving faces are available, the local face velocity can be related to the surface recession rate at time level n by,

$$u_i^n = \eta_i^n \dot{s}^n \tag{3.44}$$

3.4 Bartz Heat Transfer Correlation

The Bartz [27] heat transfer correlation has been a very popular practical method to estimate the local convective heat transfer coefficient in rocket nozzles. It is based on boundary layer equations and certain experimental correlations considering experiments performed on various nozzles. The Bartz correlation is given as follows,

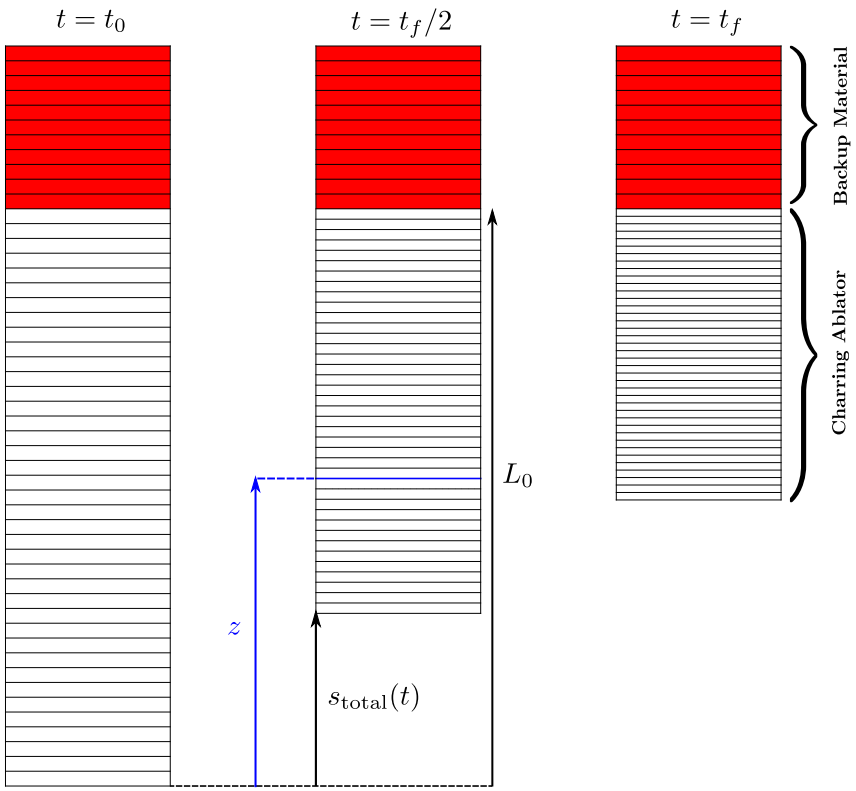

Figure 3.2: Dynamic grid scheme illustration and related reference locations, after [7].

$$h = \left[\frac{0.026}{D_t^{0.2}}\left(\frac{\mu^{0.2}C_p}{Pr^{0.6}}\right)_0\left(\frac{P_c}{c^*}\right)^{0.8}\right]\left(\frac{A_t}{A}\right)^{0.9}\sigma \tag{3.45}$$

where σ in Bartz correlation is as term to account for property variations in boundary layer and evaluated by,

$$\sigma = \frac{1}{\left[\frac{1}{2}\frac{T_w}{T_0}\left(1+\frac{\gamma-1}{2}M^2\right)+\frac{1}{2}\right]^{0.8-\omega/5}\left[1+\frac{\gamma-1}{2}M^2\right]^{\omega/5}} \tag{3.46}$$

here ω is the temperature exponent in the equation that describes the variation of viscosity with temperature.

Having obtained a value for the heat transfer coefficient, the convective heat flux is calculated by,

$$q''_{\text{conv}} = h\left(T_r - T_w\right) \tag{3.47}$$

where T_r is the recovery temperature and is calculated by the following expression,

$$T_r = T\left(1 + r\frac{\gamma - 1}{2}M^2\right) \tag{3.48}$$

this can be further related to the total conditions in chamber as given below.

$$T_r = T_0\frac{\left(1 + r\frac{\gamma-1}{2}M^2\right)}{\left(1 + \frac{\gamma-1}{2}M^2\right)} \tag{3.49}$$

Value of r in above equations depends on the regime of flow in terms of turbulence. For our considerations we stick with the commonly used value of $r = \sqrt[3]{\text{Pr}}$ for turbulent flows. The Bartz equation requires the information of local Mach number in the section of nozzle that the computation is to be performed. This is accomplished by means of performing an iterative solution for the isentropic area relation given below at each nozzle station based on local area ratio.

$$\frac{A}{A_t} = \left(\frac{\gamma + 1}{2}\right)^{-\frac{\gamma+1}{2(\gamma-1)}} \frac{\left(1 + \frac{\gamma-1}{2}M^2\right)^{\frac{\gamma+1}{2(\gamma-1)}}}{M} \tag{3.50}$$

The turbulence model assessment carried out in Section 4.3 contains comparisons with the predictions of local heat transfer with Bartz coefficient against CFD results. Results given therein shows strong discrepancies against CFD results in terms of magnitude. While the general trend of heat flux along nozzle axis is captured well with Bartz correlation, certain treend disagreement is present within the neighborhood of throat. These results suggest that care must be taken with the usage of Bartz correlation as the accuracy sought may not be sufficient for the nozzle in consideration. [61] includes a detailed experimental investigation of the application of Bartz correlation for SRM's, and also reports that Bartz correlation overestimates the amount of heat flux as illustrated in this work. Similar results are also present in [3]. Following this discussion, we introduce an additional factor defined as below to the Bartz equation to correlate the values obtained to those obtained from CFD analysis.

$$h_{\text{bartz,eff}} = C_{\text{bartz}} h_{\text{bartz}} \tag{3.51}$$

3.5 Zero Dimensional Transient Interior Ballistics Analysis

To perform an interior ballistics analysis coupled with the throat recession computations, a simple zero dimensional transient interior ballistics solver has also implemented into KAYMAK. As the chamber pressure of a SRM is crucially dependent

on the instantaneous throat area, two computations must be done fully coupled or an empirical data or relation should be supplied for throat recession rate during interior ballistics analysis. In this section, the implemented interior ballistics model is detailed.

The control volume consisting of the interior motor volume up to throat has been treated as a single element as illustrated in Figure 3.3, where spatial variations of all properties are neglected. This assumption holds very well for SRM's with low L/D ratio in which the axial pressure drop is negligible and gas velocities and mass fluxes within grain port sections are low, hence no erosive burning is present. The gas is assumed to be stagnant at chamber conditions.

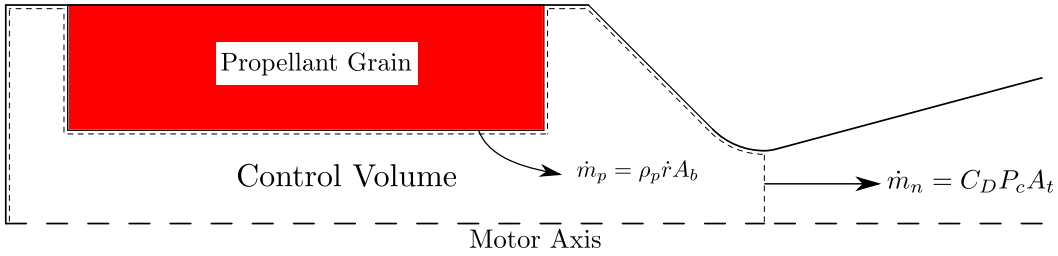

Figure 3.3: Illustration of control volume within a SRM schematic.

The transient formulation including the chamber filling end tail-off transient sections are adopted, since for certain SRM configurations these transient portions may be of importance. This type of analysis neglects all kind of dynamics due to the ignition transient, and assumes that all of the propellant burning surface has been initially ignited and producing mass. The rate of gas generation due to combustion of solid propellant is computed by,

$$\dot{m}_p = \rho_p \dot{r} A_b \tag{3.52}$$

and the mass flow rate of gas leaving the control volume through nozzle is as follows.

$$\dot{m}_n = C_D P_c A_t = \frac{P_c A_t}{c^*} \tag{3.53}$$

The Saint-Vielle's Law for solid propellant burn rate as given below is applicable to many solid propellants, however other forms can also be easily implemented.

$$\dot{r} = a P_c^n \tag{3.54}$$

Based on above considerations, the conservation of mass for control volume can be obtained as follows,

$$\frac{\partial\left(\rho_c V_c\right)}{\partial t} = \dot{m}_p - \dot{m}_n \tag{3.55}$$

expanding the terms in above equation, and employing chain rule for the derivative on the left hand side, following governing equation for the chamber pressure can be obtained.

$$\frac{\partial P_c}{\partial t} = \frac{RT_c}{V_c}\left[\rho_p(aP_c^n)A_b - \frac{P_c A_t}{c^*} - \frac{P_c}{RT_c}A_b(aP_c^n)\right] \tag{3.56}$$

To obtain a solution, the free volume inside the chamber also needs to be tracked, which increases with consumption of solid propellant. This contribution is present in Equation 3.56 within the last term that originates from the evaluation of below expression. This also requires the information related to the initial free volume inside the chamber to be available and can be disabled if no such information is present.

$$\frac{\partial V_c}{\partial t} = \dot{r}A_b \tag{3.57}$$

The propellant total burn area, A_b is dependent on the amount of the regression of the burning front. This is to be computed by means of a grain burnback analysis. The implementation in KAYMAK requires the values of $A_b(\Delta r)$ to be given in a tabular form and performs linear interpolation to obtain instantaneous values of A_b.

The numerical solution of Equation 3.56 is accomplished by means of simple Euler integration in time for P_c, V_c and r as below.

$$\begin{aligned} P_c^{n+1} &= P_c^n + \left(\tfrac{\partial P_c}{\partial t}\right)^n \Delta t \\ V_c^{n+1} &= V_c^n + \left(\tfrac{\partial V_c}{\partial t}\right)^n \Delta t \\ r^{n+1} &= r^n + \dot{r}^n \Delta t \end{aligned} \tag{3.58}$$

CHAPTER 4

FLUENT IMPLEMENTATION

This chapter describes the implementation of the theoretical foundations discussed in Chapter 2 to the commercial CFD solver ANSYS FLUENT. The main goals of this effort were directed to the following points,

1. Increase accuracy of convective heat transfer rate evaluation.
2. Increase accuracy of the computation for blowing heat transfer reduction effect.
3. Perform fully coupled transient analysis involving shape change of complete nozzle geometry.
4. Provide means to assess nozzle thrust efficiency throughout firing.
5. Provide means to perform the fully coupled analysis with boundary conditions governed by the of a interior ballistics solver.

An initial road map at the beginning of this thesis work was to develop a 2D/axisymmetric CFD solver; as the implementation, especially surface energy balance, requires serious modification which may not be realizable within customization limits of commercial CFD solvers or simply the required effort would exceed that of developing a CFD solver from scratch. Based on this belief, an explicit, multi-block structured, second order accurate CFD solver was developed, however due small time step requirements arising from explicit time integration and lack of advanced convergence acceleration techniques such as preconditioning and dual time stepping led to immense solution times that compromised the main focus of this work, and flow field analysis that should serve as a tool within stated goals started to require the ma-

jor amount of effort that needed to be given. This led to direct the effort towards implementing the features to an already available CFD solver.

The reason for the choice of FLUENT as a CFD solver to host this implementation was simply due to the authors previous experience regarding the software, and it can be said that other tools with several features, such as OpenFOAM could also be employed. An implementation in OpenFOAM targeted for the analysis of charring ablators can be found in [62], however no detailed information related to existence of CFD coupling or dynamic shape treatment is given.

With the decision of carrying out an implementation of FLUENT, the initial consideration was to employ the already available KAYMAK at locally normal directions among the nozzle wall and perform data transfer along the surface. While this could be done, it has soon led to the realization of implementing the solution of whole set of governing equations within FLUENT was possible and would decrease the numerical efficiency and development effort immensely, mainly related to the data transfer between KAYMAK which is written in FORTRAN90 and FLUENT User Defined Functions in C programming language. While they are based on same governing equations and assumptions, KAYMAK and FLUENT Implementation discussed here are completely seperate standalone tools.

The current implementation has been developed with 2D/axisymmetrical analysis of rocket nozzle flows in mind, and as in KAYMAK the ablation treatment is limited to melting ablation only. However necessary provisions exist to extend the capabilities to include thermochemical ablation and 3D coupled analysis. Since the 2D/axisymmetrical analysis targeted here typically required domain sizes about 50000 computational cells, no special effort related to the parallelization of algorithms during implementation has been carried out. However as will be illustrated parallel computation is possible within the flow side of the domain with manual partitioning.

In the first section of this chapter the implementation of governing equations for the charring solid side is detailed. Second section deals with the implementation of surface energy balance and coupling strategy to allow conjugate analysis. Third section describes the coupling of the simple interior ballistics solver, and finally fourth section deals with the approach that has been taken to suppress the shape change instability

which is previously introduced in literature as a feature that is present in coupled ablation simulations involving dynamic shape changes.

4.1 Implementation of Charring Zone Analysis

The governing equations for KAYMAK introduced in Chapter 3 are to be implemented. The previous assumptions regarding the 1D case has been extended where necessary to incorporate in 2D analysis. Before detailing the procedures, following key points are stated,

1. The energy equation governing the temperature of solid zones is already solved by FLUENT. Since the interaction of charring with the energy equation is via the source terms S_{pyr} and S_{gas}, these terms can be introduced to the energy as user defined source terms. The terms related to grid convection are already present in energy equation and no additional action is needed.
2. Two additional equations, the conservation of mass for the decomposing components A and B shall be solved. Required data for energy source terms will be available once solution is available. To accomplish this, there are two main paths;
   (a) Making use of FLUENT's User Defined Scalar (UDS) option to define the transport equation as required and solve it within FLUENT engine.
   (b) Perform required operations manually and make use of FLUENT's User Defined Memory (UDM) to store required data within solution domain.
3. Additional equations modeling the motion of pyrolysis gas in two dimensions need to be considered or further assumptions shall be made.

Based on above statements, it can be concluded that the main goal is to properly treat pyrolysis. Inclusion of resultant source terms within energy equation is relatively straightforward. The initial approach considered was to perform the implementation under the UDS capability and gain advantage of the numerical stability of FLUENT. This has been accomplished successfully to realize that terms related to grid convection are not present for UDS that are solved in solid zones. Hence manual inclusion

of these grid convection terms is a necessity. This raised concerns and with the desire to use the exact same numerical treatment in KAYMAK, solution for Equation 2.10 is carried out within a separate routine in C code, and FLUENT is basically used as a discretized solution environment. Solution data is stored in each cell within UDM locations.

Inclusion of grid convection terms requires the resolution of the flux term given below,

$$F_{\text{gc}} = \oint_S (\rho C_p T)\, \mathbf{v}_s \cdot d\mathbf{S} \tag{4.1}$$

and the source term arising due to the change of control volume as in the second RHS term of below equation.

$$\frac{\partial}{\partial t} \int_V \rho_j dV \approx \frac{\partial \rho_j}{\partial t} \Delta V + \frac{\partial \Delta V}{\partial t} \rho_j \tag{4.2}$$

The change of cell volume depends on the motion of faces forming the cell. Computing the rate of change of cell volume with below equation also satisfies the grid conservation law.

$$\frac{\partial}{\partial t} \int_V dV = \oint_S \mathrm{v}_s \cdot d\mathrm{S} \approx \sum_{\text{faces}} \mathrm{v}_f \cdot \mathrm{S}_f \tag{4.3}$$

The velocity of faces are defined at their centroids and their motion is computed based on averaging the motion of nodes defining the faces within a timestep. Nodal coordinates for the previous time step are accessible within UDF environment. Having computed the value of face centroid velocity, the required source term and flux term for grid convection are evaluted.

The 1D treatment of pyrolysis gas flow in KAYMAK was based on zero residence time and locally isothermal assumptions for the gas. Since the domain was one dimensional the flow direction was not a concern. However for the 2D treatment we either need to assign a flow direction for pyrolysis gas under certain assumptions, or implement one of the porous media approaches in literature to solve continuity equation for gas with a momentum closure in the form of Darcy's or Forchheimer's law.

As discussed before the heating conditions in solid rocket nozzle environments are characterized with extreme heating rates and relatively short exposures leading to

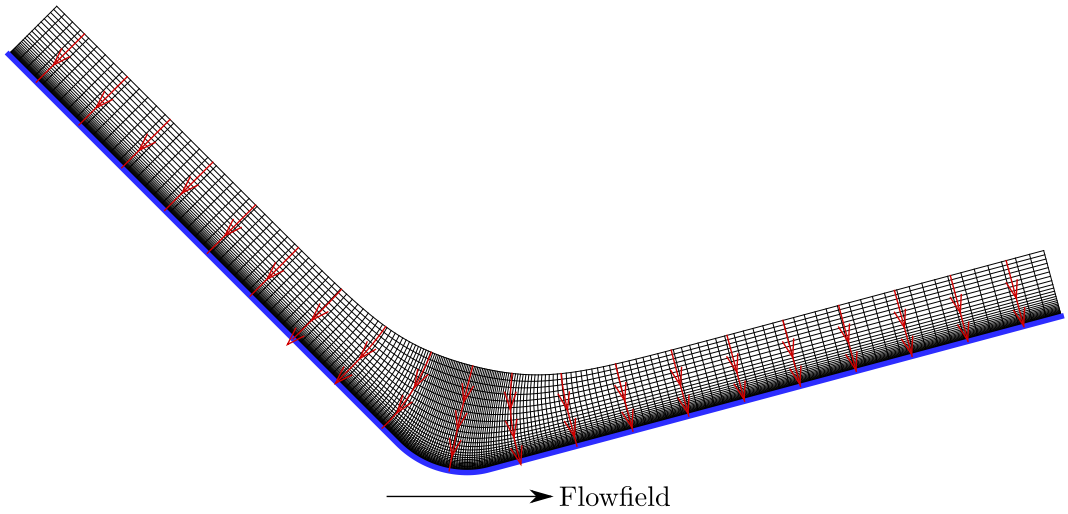

Figure 4.1: Structured orthogonal grid system and illustration of assumed pyrolysis gas flow direction.

thin char layers. This kind of situation is suitable to assume that the pyrolysis gas formed at each axial location of the nozzle move in the local normal direction.

To realize this assumption within the discretized solution domain, two approaches can be followed. The easiest realization is that if the discretization is performed in such a manner that local normal orientation is preserved within grid, then the computation of the amount of gas flowing through a cell can easily be conducted as in KAYMAK. If the discretization does not preserve the normal orientation, then an additional continuity equation needs to be employed. Here the first approach is by employing a high quality structured grid such that constant i direction is orthogonal to nozzle wall. An example grid system along with streamlines of gas flow is given in Figure 4.1. This way the amount of gas flowing through a cell can be computed by employing Equation 3.23 along constant i-lines. While the necessity to use a structured grid may pose some restrictions on the geometry, it is only required up to the extent of char plus recession where production of pyrolysis gas will be present, which is usually quite thin for general solid rocket nozzle cases. Beyond that zone any kind of grid system can be used and only the energy equation for the virgin state of material can be solved within FLUENT.

The strategy described above requires a structured access capability to identify the

cells laying on constant i-direction, however FLUENT is an unstructured solver and access to individual cells are done by pointers to individual cell threads within UDF environment. The fact that the cell loop within a cell zone is based on the cell ID can be exploited to create an ordered array of cell pointers corresponding to their i and j indexes.

To accomplish this the generated grid shall be exported in an (i, j) ordered fashion, where cell $(1, 1)$ corresponds to southwest corner and cell ID increases in i-direction. For this structure, the cell indexes can be computed by the following expressions, where ID_{sw} denotes the cell ID of southwest cell.

$$\begin{aligned} i &= \text{ID} - \text{ID}_{\text{sw}} \pmod{i_{\text{max}}} \\ j &= \left\lceil \frac{\text{ID} - \text{ID}_{\text{sw}}}{i_{\text{max}}} \right\rceil \end{aligned} \tag{4.4}$$

Above discussion outlines the key points that has been required to implement the charring zone analysis capability within FLUENT. No more details are included since the numerical treatment is the same as in KAYMAK and is already discussed in Chapter 3.

One point to mention here is that FLUENT does not allow to define dependence of C_p to any other variable than temperature. While density and thermal conductivity as defined in Chapter 3 are implemented as functions of local degradation parameter and component densities with `DEFINE_PROPERTY` macros, this is not possible for C_p. This limitation causes to inability to treat the char and virgin C_p values separately. However as will be illustrated in Chapter 5 this is not a serious issue since values of C_p for virgin and char states found in literature are either very close or same values are used.

4.2 Implementation of Surface Energy Balance and Coupling Strategy

Resolution of the surface energy balance along with surface mass balance for thermochemical ablation mechanism is perhaps the only proper way to perform conjugate analysis of flow field and a charring ablator. On a discrete basis, this operation is identical to perform the surface energy balance considered in KAYMAK on each face separating the flowfield and solid, and computing the convective heat flux based

on flowfield temperature gradient in the local normal direction. While conjugate heat transfer analysis is within the capabilities of FLUENT, implementation of surface energy balance could not be performed without breaking the default conjugate heat transfer linking within FLUENT. The default shadow-zone coupling mechanism in FLUENT is removed and rewritten considering the resolution of surface energy balance. Surface energy balance for conjugate analysis during the heating or cooldown phases, i.e while surface is stationary is given as follows,

$$k_f \left.\frac{\partial T}{\partial n}\right|_f - \sigma \epsilon_w \left(T_w^4 - T_{\text{surr}}^4\right) - k_s \left.\frac{\partial T}{\partial n}\right|_s + \dot{m}_{\text{g}}'' \left(h_w - h_{\text{g,in}}\right) = 0 \tag{4.5}$$

The only difference from previously introduced Equation 3.32 is the first term replacing the convective heat transfer coefficient approach with the fluid side temperature gradient. On a local basis convection process is governed by the conductive heat transfer between fluid adjacent to wall, while actual convection of heat is dependent on the dynamics of boundary layer and its interaction with core flow field. The normal gradient term is discretized as follows,

$$\frac{\partial T}{\partial n} = \frac{T_w - T_{\text{cell}}}{\Delta S_\perp} \tag{4.6}$$

where $\Delta S_\perp$ denotes the normal distance between wall face centroid and corresponding cell centroid as illustrated in Figure 4.2 and computed by,

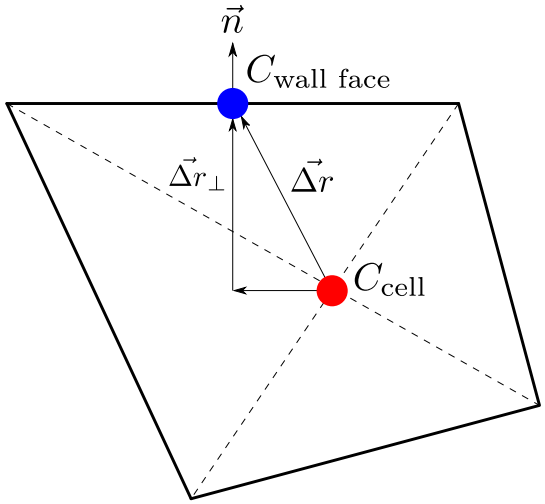

Figure 4.2: Vectors used for normal gradient computation adjacent to wall.

$$\Delta S_\perp = |\mathbf{\Delta r}_\perp| = \mathbf{\Delta r} \cdot \mathbf{n} \tag{4.7}$$

Note that for an ideal case the orientation of face and cell centroids would be such that the vector s $\mathbf{\Delta r}$ and $\mathbf{n}$ would be parallel. While this is easily satisfied for the initial state of grid, divergence from this ideal case occurs as the grid deforms in regions where ablation is present. As done in Chapter 3, we cast Equation 4.5 into the fourth order polynomial form of Equation 3.33 and obtain the coefficients with the following expressions.

$$\begin{aligned} A &= \left.\frac{kT_{\text{cell}}}{\Delta S_{\perp}}\right|_f + \left.\frac{kT_{\text{cell}}}{\Delta S_{\perp}}\right|_s + \sigma\epsilon_w T_{\text{surr}}^4 + \dot{m}_{\text{g}}^{''}\left(h_{\text{g,in}} - h_w\right) \\ B &= -\left.\frac{k}{\Delta S_{\perp}}\right|_f - \left.\frac{k}{\Delta S_{\perp}}\right|_s \\ C &= -\sigma\epsilon_w \end{aligned} \tag{4.8}$$

Equation 4.5 is solved to obtain wall temperature for each non-ablating wall face within each dual-time iteration in FLUENT through a `DEFINE_ADJUST` macro, with implementation of a Newton-Raphson routine as introduced in Chapter 3. The pyrolysis gas mass flux term is obtained through the gas mass flow rate available from the in-depth solution and divided by face area to obtain the gas flux through face. As done before gas enthalpies are computed based on the surface temperature from the previous time step.

For the solver configuration, both fluid and solid zones has a spatially varying temperature boundary condition for the nozzle wall which has been fed into the solver with `DEFINE_PROFILE` macros. This way absolute control of the surface temperature has been achieved. However, with this kind of implementation control over the heat fluxes acting on the solid and fluid cells adjacent to the wall has been left to FLUENT and needs to be checked. These are expected to be equal to the heat flux values computed by the normal gradient evaluation discussed in this section and observed to be identical within 0.1% with the default LSQ gradient scheme in FLUENT. It is also possible to alter the method for computation of wall heat fluxes within FLUENT with `DEFINE_HEAT_FLUX` macro, however this has not deemed necessary as almost identical results has been achieved.

The downside of performing the conjugate heat transfer coupling manually comes as stability problems that can occur due to very large gradients felt in first time steps, as we no longer have the leverage of internal numerics built-in FLUENT. Large cell volume ratios of fluid and solid cells adjacent to wall increases this instability. For

the analysis presented in this work, the first cells in boundary layer have a height of 0.1μm for y^+ requirements. Solid cells with a first layer height of 1μm corresponding to a planar volume ratio of 10 has been used. Also to obtain a good resolution in pyrolysis zone refinement of solid cells towards the wall is necessary. Even with a planar volume ratio of unity, stability could not be achieved without considering some sort of a relaxation parameter. This has been achieved through a relaxation parameter defined as follows,

$$\beta_r = max\left(1, \text{N\_TIMESTEP}/\text{N\_RAMP}\right) \tag{4.9}$$

here, N_TIMESTEP is the number of current solution time step and N_RAMP is an user defined parameter that defines the extent of relaxation in terms of number of time steps. The value of convective heat flux, denoted with the first term of Equation 4.5, is relaxed through multiplication of k_f with the relaxation parameter β_r. This linearly increases the amount of supplied convective heat flux from zero to its actual value within N_RAMP timesteps. This obviously destroys the time accuracy within first N_RAMP timesteps, however the required values of N_RAMP has been observed to be about 10. Combined with the timescale of the problem and the small time step sizes that needs to be used in the initial transient of a coupled interior ballistics solution, this has no effect on the overall solution results.

As solution progresses, eventually certain faces exceed the predefined melting ablation temperature value, $T_{\text{abl}} = 1996$ K for silica phenolic. When this occurs, the surface energy balance equation on these faces are switched to below equation and temperature is set to T_{abl}.

$$k_f \left.\frac{\partial T}{\partial n}\right|_f + \dot{s}\rho_c h_c + \dot{m}_{\text{g}}^{''} h_{\text{g,in}} + \sigma\epsilon T_{\text{surr}}^4 - k_f \left.\frac{\partial T}{\partial n}\right|_s - \sigma\epsilon T_w^4 - \dot{m}_{\text{g}}^{''} h_w - \dot{s}\rho_c \Delta H_{\text{melt}} = 0 \tag{4.10}$$

As done in Chapter 3, the discretized form of above equation, given below, is used to compute the value of local recession rate at face centroid.

$$\dot{s}_{\text{face}} = \frac{\overbrace{\left.\frac{k\left(T_w - T_{\text{cell}}\right)}{\Delta S_\perp}\right|_f}^{\dot{q}_{\text{conv}}^{''}} - \overbrace{\dot{m}_g^{''}\left(h_w - h_{\text{g,in}}\right)}^{\dot{q}_{\text{gas}}^{''}} - \overbrace{\sigma\epsilon_w\left(T_w^4 - T_{\text{surr}}^4\right)}^{\dot{q}_{\text{re-rad}}^{''}} - \overbrace{\left.\frac{k\left(T_w - T_{\text{cell}}\right)}{\Delta S_\perp}\right|_s}^{\dot{q}_{\text{cond}}^{''}}}{\rho_c\left(\Delta H_{\text{melt}} - h_c^{1996}\right)} \tag{4.11}$$

If the numerator of above equation becomes negative, the surface energy balance routine switches back to the stationary surface computation given by Equation 4.5. The individual components labeled in Equation 4.11 are also stored in UDM for examination and post-processing.

4.3 Solution Strategy, Boundary Conditions and Turbulence Model Assessment

A sketch of boundary conditions is given in Figure 4.3. Flow is modeled as axially symmetric. To simulate the nozzle flow the inlet is modeled as a pressure inlet boundary condition where total pressure and temperature are specified and flow direction is normal to the boundary. Before the convergent part of nozzle a short straight section is included as it improves stability, also such a portion is present in the motor geometry investigated in Chapter 5.

Outlet is a pressure outlet where ambient pressure and temperature are specified. While backflow is permitted through specification of total pressure and temperature from this boundary, it does not occur for the most parts of analysis due to outgoing characteristics present in supersonic flow. All unlabeled boundary conditions in Figure 4.3 are adiabatic walls except the wall seperating fluid and solid zones.

Related works in literature [17, 51, 53] has employed Spalart-Allmaras, k-ω BSL or k-ω SST turbulence models, and resolution of boundary layer was achieved with employing grid systems such that $y^+ < 1$. The employment of Spalart-Allmaras for nozzle flows is rather rare in literature, hence the aforementioned usage of this model has been treated as an isolated case. In [63] authors have demonstrated the unphysical behavior of k-ω SST formulation under favorable pressure gradient conditions that is present in nozzle flows against experimental data. It was also shown in [63] that k-ω BSL formulation produces better agreement with experimental observations. Same observation is also present in [50]. In general the SST formulation under-predicts the rate of heat transfer. Based on these findings the k-ω BSL turbulence model is employed for the results presented in Chapter 5. A comparison for these three turbulence models has been presented in Figure 4.4 for the undeformed geometry of nozzle defined in Chapter 5. The obtained results confirm that SST formulation predicts a

lower heat transfer rate whereas Spalart-Allmaras and BSL formulations predict almost identical heat transfer rates in the vicinity of throat. These computations were made for a inlet total pressure of 85 bar and a constant wall temperature of 1500 K, on a grid system providing a $y^+ \approx 0.35$ at throat, properly resolving the viscous sub-layer. The values obtained for the value of convective heat flux at throat are also compared with the prediction made by Bartz correlation, and given in Table 4.1.

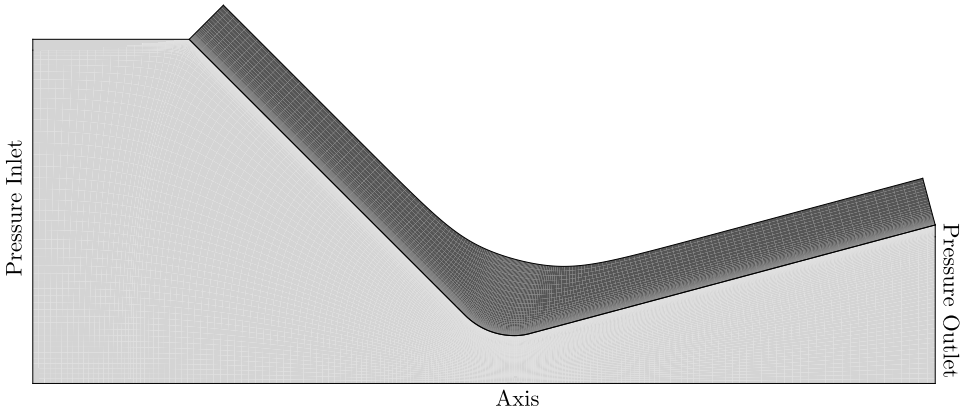

Figure 4.3: Illustration of boundary conditions. Dark region is the charring ablator solution zone.

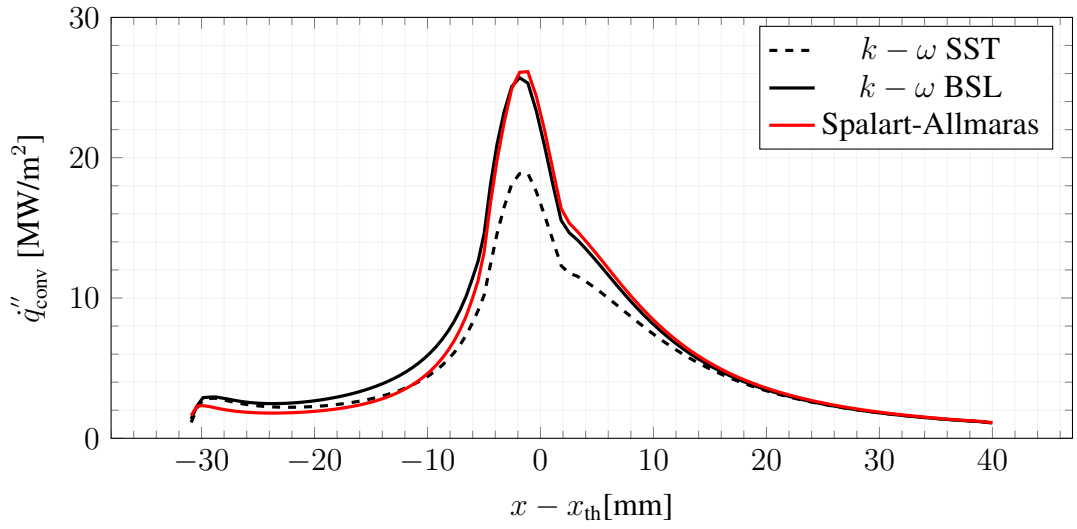

Figure 4.4: Comparison of heat flux values computed with different turbulence models, T_w = 1500 K. Coarse grid shown in Figure 4.5 has been used.

As shown in Table 4.1, Bartz correlation over predicts the heat transfer rate similar to shown in other works in literature [2, 19] with similar nozzle dimensions.

Table 4.1: Throat heat transfer rate comparison with Bartz correlation for different turbulence models.

Model	h [W/m^2/K] for T_r =2763 K	h_{Bartz} [W/m^2/K]	C_{Bartz}
$k-\omega$ SST	14951.022	29144.775	0.513
$k-\omega$ BSL	20352.195	29144.775	0.698
Spalart-Allmaras	20691.264	29144.775	0.710

FLUENT offers two solvers, namely the pressure-based solver and density-based solver and both of them has implicit implementations available. For highly compressible flows such as the one considered in this work the density based approach seems more suitable as pressure bsaed formulations are generally used for incompressible flows. However the pressure based coupled solver in FLUENT has excellent applicability for compressible flows and produces identical results with the density based solver and comes with a major advantage that it offers higher stability thus reducing the number of iterations required. All solutions presented in this work are obtained with second order discretization for all solution variables. Transient simulations are conducted with a first order implicit temporal discretization employing a dual-time convergence acceleration scheme. As discussed before the devised coupling mechanism involving the surface energy balance is also present for the iterations in pseudo-time.

For the analysis presented in Chapter 5 a grid dependence study has been performed considering the change of the axial distribution of heat transfer rate. The refinement was carried out in the vicinity of throat region where most of the shape change phenomena occurs. Three set of grids for the flow domain are considered as in Figures 4.5 to 4.7. The grid spacing adjacent to wall is identical for all three cases and equal to 0.1μm. The test analysis has been conducted for a uniform wall temperature of 1996 K and a inlet pressure of 80 bar with $k-\omega$ BSL turbulence model. Solution are carried out until residuals are flattened. Results for axial distribution near the throat region is given in Figure 4.8.

Inspecting Figure 4.8, it is evident that the coarse grid does not resolve the axial

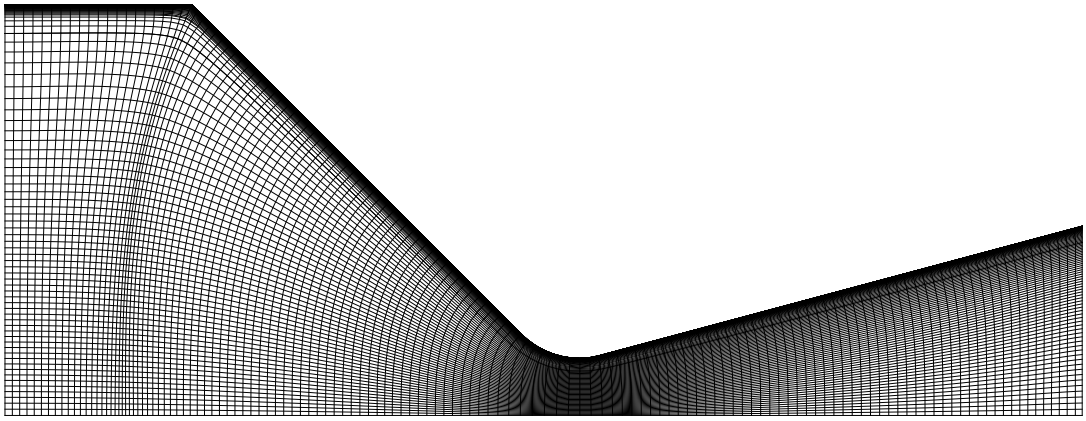

Figure 4.5: Coarse grid. 134 $\times$ 119.

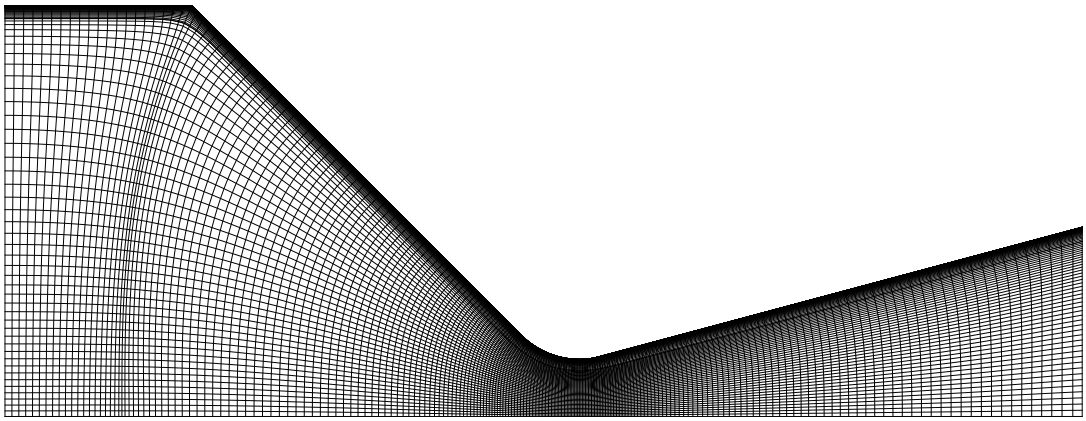

Figure 4.6: Medium grid. 194 $\times$ 119.

gradient as well as medium or fine grids. Although the resolution is almost doubled from medium grid to fine grid, almost identical results have obtained. Therefore the medium grid resolution will be used for the conjugate analysis in Chapter 5.

One point to discuss related to the distribution given in Figure 4.8 is the occurrence of a local minima at downstream of throat, about $x = 1.7$mm. This location coincides with the small radius that is present between throat and divergent cone as in Figure 5.19. The occurrence of this local minima is dependent on the wall temperature, and observed to be vanishing for a cold wall analysis. As the surface recession for melting ablation is primarily driven by the local heat transfer rate, concerns related to the internal contour shape produced with this kind of distribution and its possible impact on stability led to further investigation of this phenomena. Similar hot wall

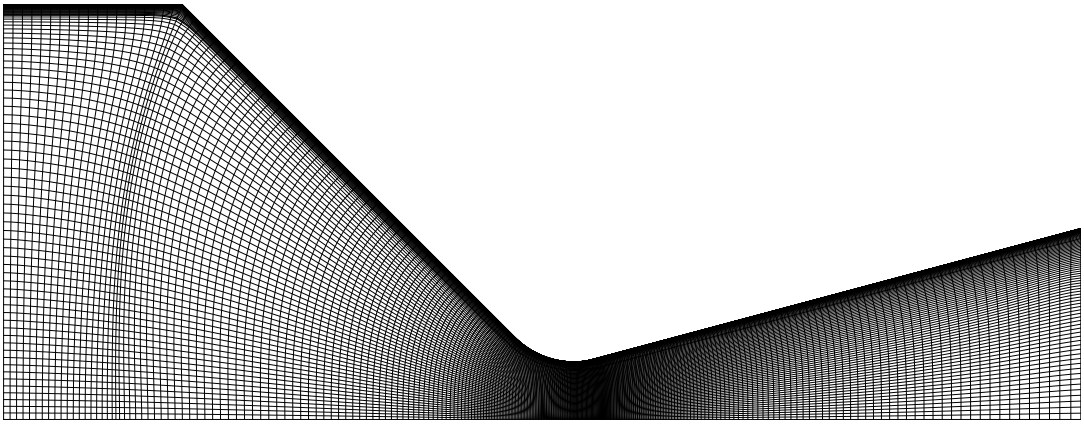

Figure 4.7: Fine grid. 241 $\times$ 119.

analysis carried out in [63] also indicate the presence of the same phenomena in the same location. Research carried on this specific issue did not led to finding any experimental backup, hence the physicality of this phenomena is still regarded as a question. Opinion here is that this is related to the sharp curvature change leading to the sudden expansion of nozzle core flow. The effect of this phenomena was also observed in the final contour produced by the conjugate analysis in Chapter 5. Results for a wide range of wall temperature has is given in Figure 4.9, concentrated on the aforementioned location.

As discussed above, Figure 4.9 illustrates that the local minima that occurs about $x = 1.7$ mm vanishes with decreasing wall temperature. It can be also observed that the maximum heat transfer rate occurs slightly upstream of physical throat location. This is most probably due to the fact that the physical location of throat is a point for this particular geometry with large curvature regions present both in upstream and downstream locations.

4.4 Pyrolysis Gas Injection

The implementation of blowing boundary condition for CFD has been previously introduced and validated in Chapter 2. The gases produced from the combustion of solid propellant and pyrolysis gases have different thermodynamic and transport properties and this needs to be accounted. Since most of the work in literature dealing with

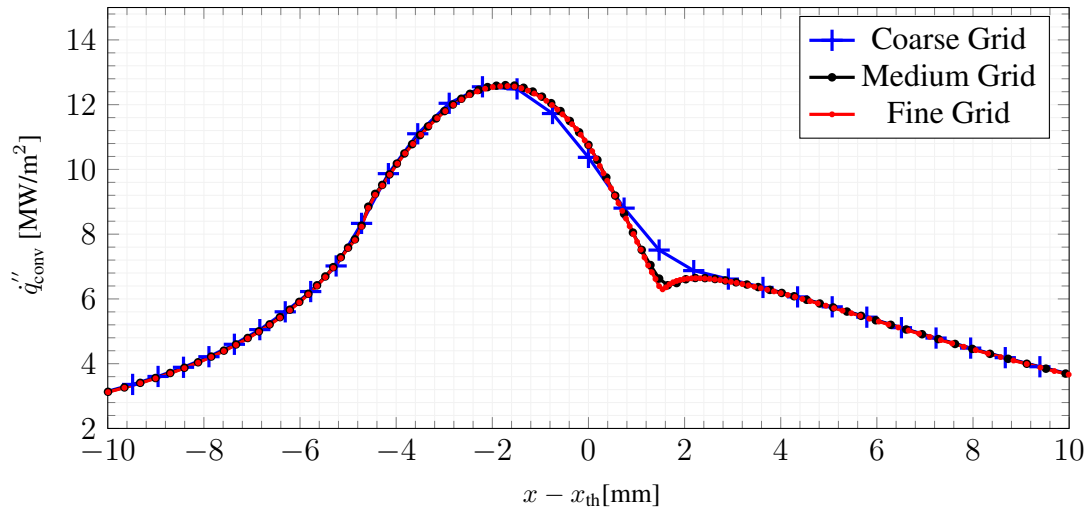

Figure 4.8: Results of grid refinement study in the axial neighborhood of throat. $T_w =$ 1996 K.

ablation problems is focused on the thermochemical ablation of carbon based materials, concentration of individual species contributing to surface reactions becomes a parameter of primary importance. Therefore such simulations generally involve solution for the conservation of primary species, and products of ablation which are gaseous as well as pyrolysis gas are considered as such. Since in this work the mechanism of ablation that is investigated is a failure mechanism, we are not dealing with surface reactions.

To simplify the problem based on above considerations, the combustion products and pyrolysis gas are treated as different species as a whole rather than tracking their individual constituents, and local properties are evaluated with ideal gas mixing law in mixed regions. The mass diffusivity is computed by unity Lewis number assumption.

With the availability of in-depth solution for the charring ablator, the mass flow rate of pyrolysis gas adjacent to the nozzle wall is available. Based on the pyrolysis gas mass flow rate value of the adjacent cell the injected mass flux is computed by,

$$(\rho v)_w = \frac{\dot{m}_g}{A_{\text{face}}} \tag{4.12}$$

for the computation of injection velocity in the wall normal direction that is required for the momentum source terms, the gas density at wall needs to be computed. This

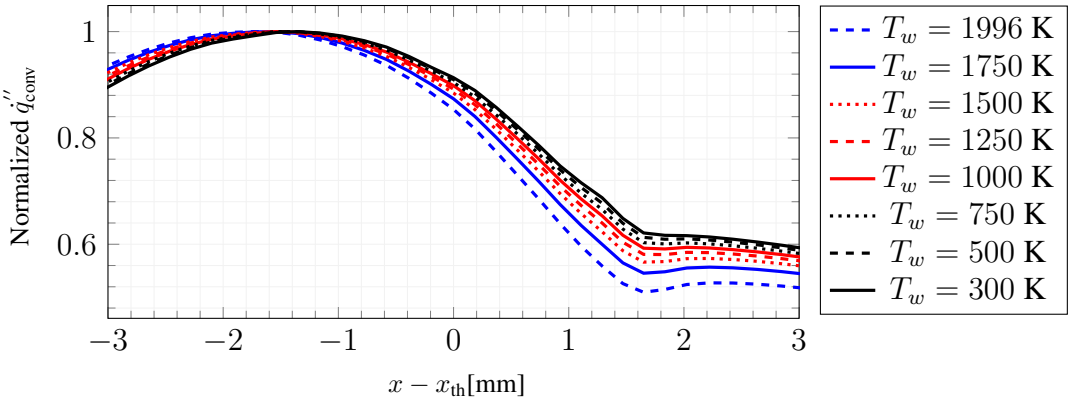

Figure 4.9: Effect of wall temperature on the behavior of heat flux distribution in the vicinity of throat.

is done with the ideal gas relation as follows.

$$\rho_w = \frac{P_w}{RT_w} \tag{4.13}$$

The set of equations for the source terms that are defined at the adjacent boundary layer cell to the nozzle wall are given below. The momentum source is split into axial and radial components based on the value of local unit normal vector at nozzle wall face centroid. The components of unit normal vector is denoted as n_x and n_y. Value of h_g required for the energy source term is evaluated at the wall temperature.

$$\begin{aligned}
\dot{s}_{\text{mass, pyrolysis gas}} &= (\rho v)_w \, \tfrac{A_{\text{face}}}{V_{\text{cell}}} \\
\dot{s}_{\text{x-mom}} &= n_x \, (\rho v)_w \, v_w \, \tfrac{A_{\text{face}}}{V_{\text{cell}}} \\
\dot{s}_{\text{y-mom}} &= n_y \, (\rho v)_w \, v_w \, \tfrac{A_{\text{face}}}{V_{\text{cell}}} \\
\dot{s}_{\text{energy}} &= (\rho v)_w \, h_g \, \tfrac{A_{\text{face}}}{V_{\text{cell}}}
\end{aligned} \tag{4.14}$$

As discussed in Chapter 2, the equilibrium composition of the pyrolysis gas has a quite significant variation over the pressure and temperature ranges that are present at the nozzle wall. The inclusion of this variation is only possible through individual tracking of species that form the pyrolysis gas. As though this is possible to implement in FLUENT, and further integrate the equilibrium wall composition by means of pre-calculated lookup tables no such attempt has been considered in this work.

Another point to mention here is that the amount of blowing present in the boundary layer is quite low for melting ablation when compared to the thermochemical ablation

cases in which the products of ablation process are also gaseous and needs to be included in the $(\rho v)_w$ term.

4.5 Coupling with Zero Dimensional Transient Interior Ballistics Solver

Reults of a conjugate analysis coupled with the simple interior ballistics model introduced in Chapter 3 is presented in Chapter 5. For this purpose the interior ballistics model has been included in the C code as a separate routine, and previous time step values of integrated quantities are held in memory with static variables. As discussed before, the interior ballistic state of a solid rocket motor primarily depends on the balance between two quantities, rate of gas generation and rate of gas ejection through nozzle. With the availability of the flow field solution, the mass flow rate through the nozzle can be computed by,

$$\dot{m}_n = \int_{\text{outlet}} \rho u dA \tag{4.15}$$

where u is the axial component of the velocity vector. Similarly, instantaneous thrust is computed by performing the integration given below, where all variables are evaluated at faces of the outlet.

$$T = \int_{\text{outlet}} \left(\rho u^2 + P - P_{\text{amb}}\right) dA \tag{4.16}$$

Obtained value for the mass flow rate leaving the nozzle is fed into the governing interior ballistics differential equation by replacing the corresponding term Equation 3.56 with Equation 4.15 to obtain below equation. This form of the equation including the mass storage allows to approximate the chamber filling transient.

$$\frac{\partial P_c}{\partial t} = \frac{RT_c}{V_c}\left[\rho_p(aP_c^n)A_b - \dot{m}_n - \frac{P_c}{RT_c}A_b(aP_c^n)\right] \tag{4.17}$$

The value of A_b versus burnt distance r is supplied in the form of a lookup table and instantaneous values are computed by linear interpolation.

4.6 Shape Change Instability, Suppression, Root Cause and Investigation of Amplification Mechanism

During development of this implementation certain instabilities causing some sort of noise on the axial distribution of $\dot{s}$ has been experienced. Even tough the solver is perfectly stable for the solid and fluid zone computations within presence of this noise, the unphysical deformations induced on the nodes eventually blow up the solution. Research on this issue has revealed that this type of instability is common for ablation simulations involving dynamic shape change dependent on the flow field. Since this field of fluid/structure interaction is quite narrow, only [64] specifically deals with this issue. Other works [50, 53] has made use of this method and improved it based on their unique implementation needs.

The oscillations start to initiate after a certain amount of successive deformations are applied. An example is given in Figure 4.10. These data were taken from the development process of conjugate analysis presented in Chapter 5.

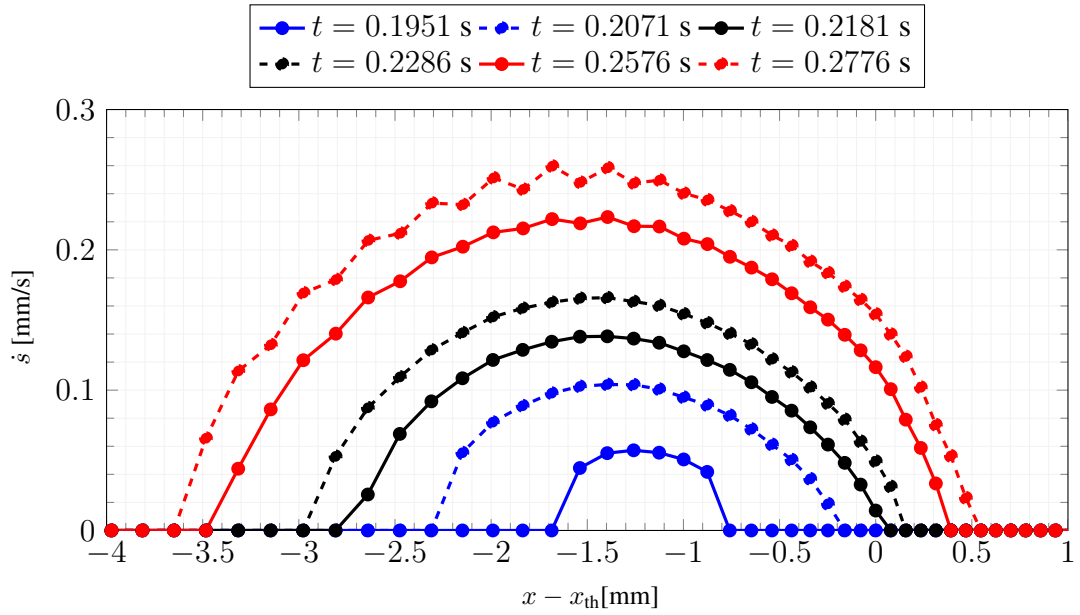

Figure 4.10: Illustration of the initiation of instability. Time step was 1 ms throughout this period.

The implementation of the smoothing scheme described in [64] and [53] has been implemented and no other effort was necessary to suppress the instability. The smooth-

ing method is a moving average filter within a stencil spanning n_w points upstream and downstream of each point as given below. It can be considered as a simple low-pass filter.

$$\dot{s}_i = \frac{1}{2n_w + 1} \left(\dot{s}_{i-n_w} + \cdots + \dot{s}_{i-1} + \dot{s}_i + \dot{s}_{i+1} + \cdots + \dot{s}_{i+n_w} \right) \tag{4.18}$$

This smoothing has been applied to the values of $\dot{s}$ on nodes which have non-zero recession rate. While a constant 5 point stencil corresponding to $n_w = 2$ has been used in [53], a variable span has been considered in this work. As authors of [53] has mentioned this method does not cure the instability but only delays it, therefore in this implementation it is made possible to pause the analysis and adjust the span of moving average filter within FLUENT. This is done manually and care must be taken to ensure using excessively large spans. A sample application has been illustrated in Figure 4.11 for various span sizes.

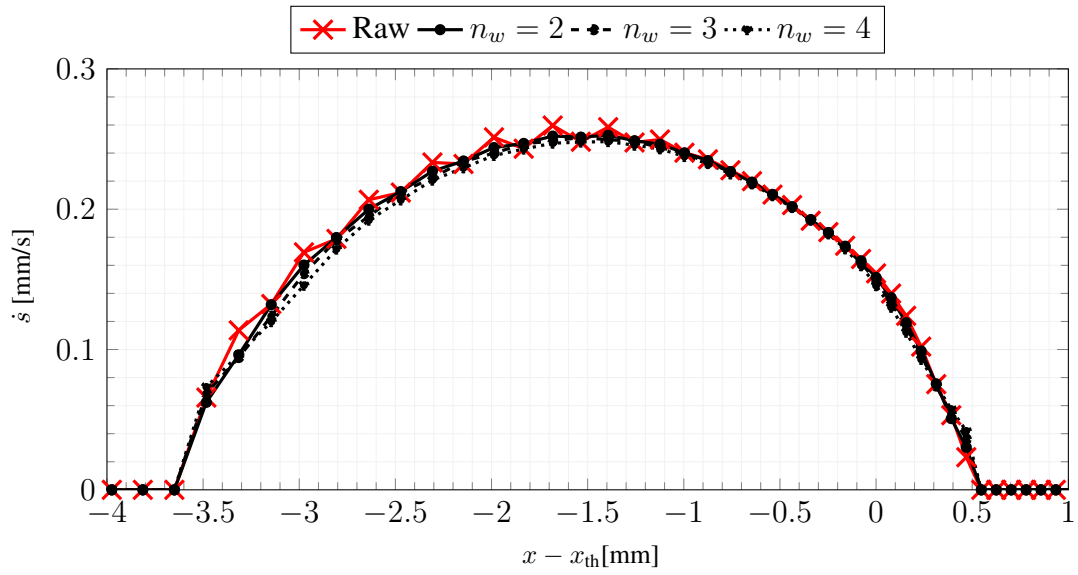

Figure 4.11: Illustration of the moving average filter. Applied on data for t =0.2776 s in Figure 4.10.

As demonstrated in Figure 4.11 this method effectively removes the oscillations and does not alter the data in the stable portions. The implementation initiates the value of n_w from 2 as the default value. While there are certain investigations present in [64] and [51, 53] there appears no definite explanation for the underlying physical mechanism triggering this phenomena. One of the strong points of the implementation presented here is the fact that whole process is governed within a single software and

a very tight coupling has been achieved between fluid and solid zones, the local recession rates and geometry is updated every time step. Combined with the simplicity of melting ablation when compared to thermochemical ablation, this case allows to study the instability in more detail.

Post-processing the results has shown that even if the instability is suppressed and simulation is advanced with such kind of proper surface recession with the implementation of aforementioned filtering, the root cause remains. If the convective heat flux term given below is inspected we still observe the oscillations within the axial extent of ablation. Since this value is only effective in the computation of $\dot{s}$ as far as the stability of the solution is concerned this poses no problems.

$$q''_{\text{conv}} = k_f \frac{\partial T}{\partial n}\bigg|_f \tag{4.19}$$

The evaluation of the above gradient has been previously discussed and it has been compared with the LSQ gradient scheme which is the default option in FLUENT, and observed to produce almost identical results. In fact, if built-in computation of heat flux distribution is plotted within FLUENT, oscillations are still present as shown in Figure 4.13.

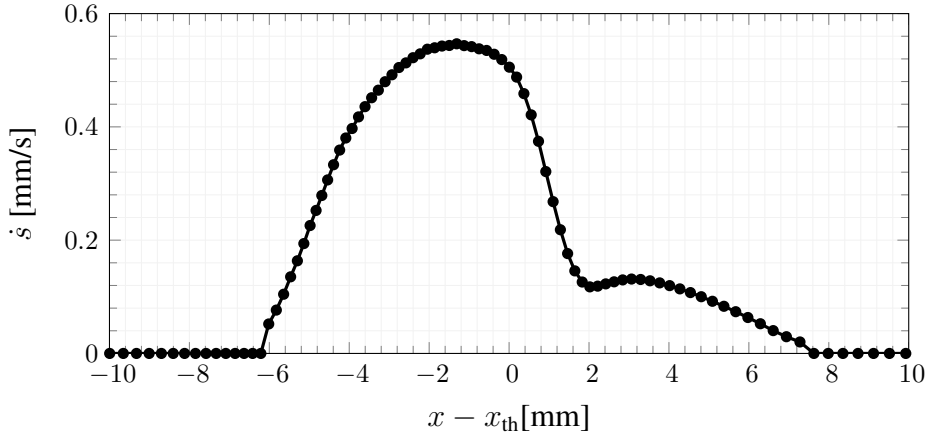

Figure 4.12: Distribution of $\dot{s}$ for $t = 0.5875$ s. Moving average filter was active with $n_w = 3$.

It is evident that evaluation of the expression given in Equation 4.19 depends on a few quantities, that are k_f, T_w, T_{cell} and local unit normal vectors. Since value of k_f also depends on cell temperature it can be removed from this list. The wall temperature

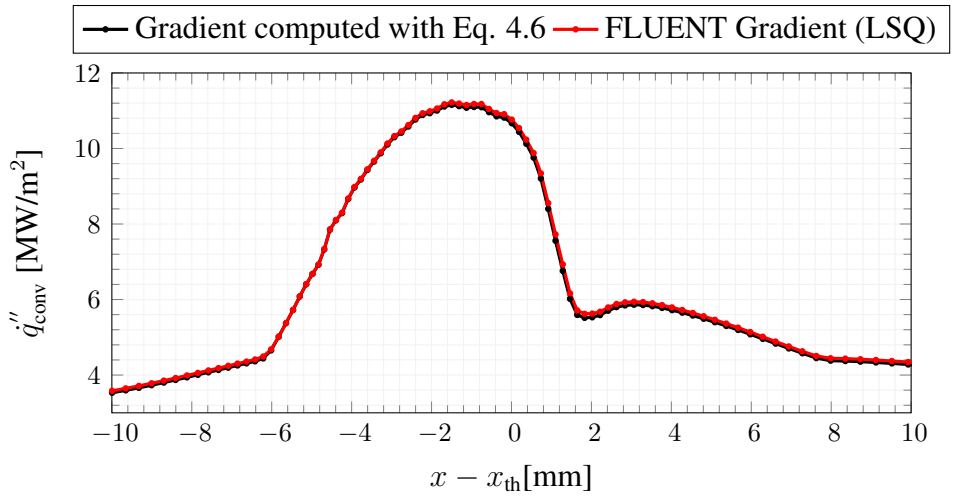

Figure 4.13: Distribution of q''_{conv} for $t = 0.5875$ s. Oscillations are small in magnitude but they are present.

is also constant when ablation is present, hence T_w can also be removed from this list, leaving T_{cell} and unit normal vectors to consider. The axial distribution for the components of unit normal vector is given in Figure 4.14.

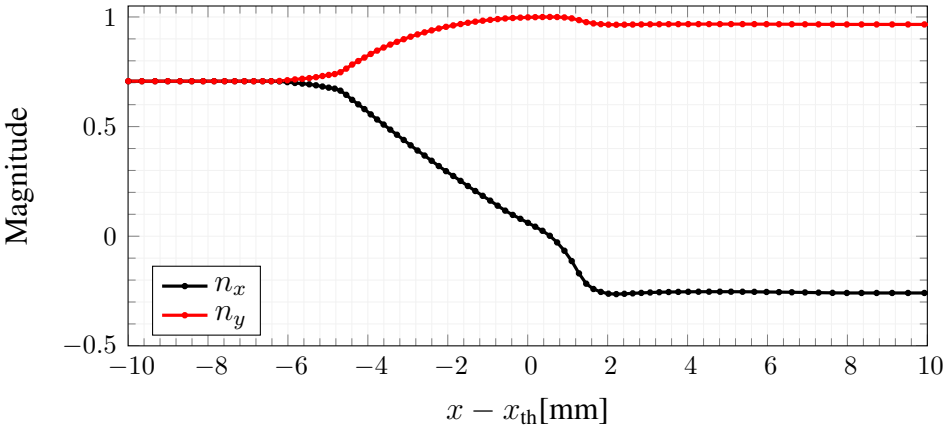

Figure 4.14: Distribution of n_x and n_y for $t = 0.5875$ s. Moving average filter was active with $n_w = 3$.

Distribution of the adjacent cell temperature difference is given in Figure 4.15. Very small oscillations are present in the temperature distribution that are probably caused due to the distribution of heat flux. The data presented so far does suggest a probable root cause for the instability. However instead of considering the smooth appearance of unit normal vector components given in Figure 4.14, their axial derivatives shall

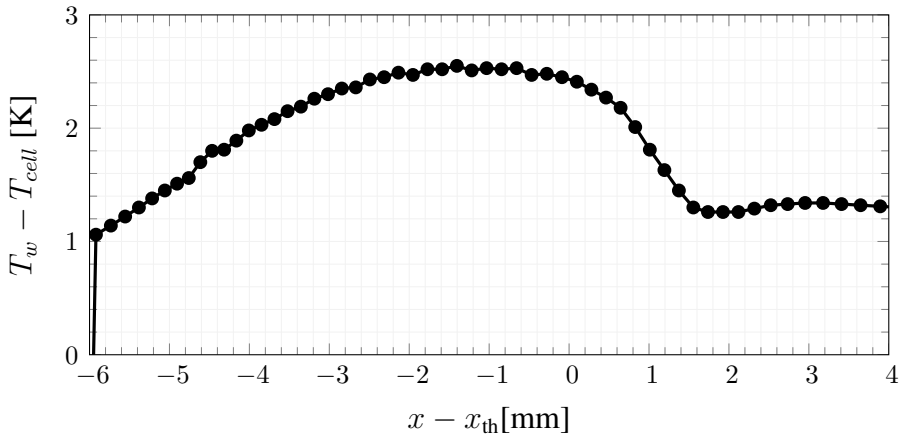

Figure 4.15: Distribution of adjacent cell temperature difference for $t = 0.5875$ s. Note the scale of y-axis.

be investigated to detect small oscillations. At this point, one may also blame the injection source terms present in the first cells of boundary layer that we have been inspecting so far as a potential reason for this instability. Considering Equation 4.14, the driving term is $(\rho v)_w$ and its magnitude is dependent on the outcome of the conjugate in-depth analysis. For clarity its axial derivative is also presented in Figure 4.16 among other variables.

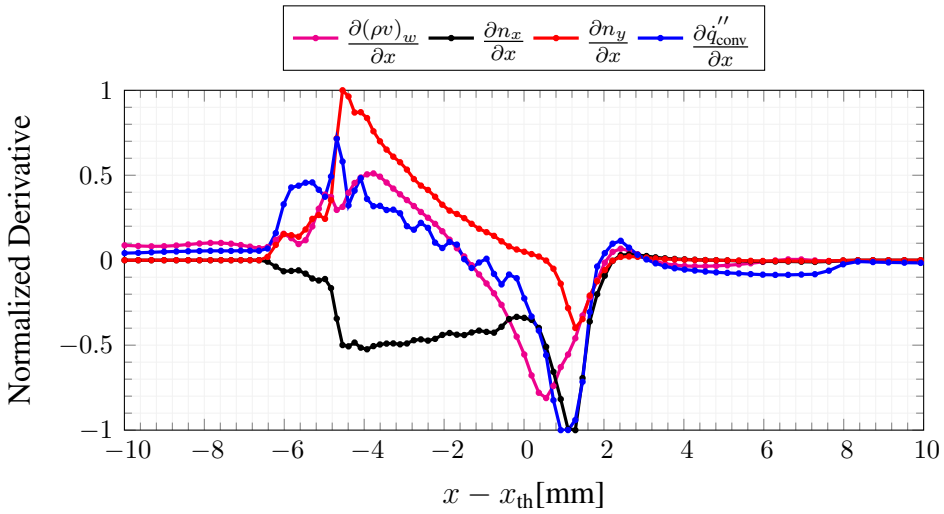

Figure 4.16: Distribution of normalized axial derivatives of various variables for $t = 0.5875$ s.

Figure 4.16 does not suggest any correlation between the distribution of axial deriva-

tive of pyrolysis gas mass flux and distribution of derivative of heat flux. However there is a clear match between the frequency small oscillations in the derivative of n_x with the derivative of heat flux, and they are greatly amplified. The reason for this amplification seems to be due to the definiton of gradient,

$$\dot{q}''_{\text{conv}} \propto \frac{\partial T}{\partial n} = \frac{T_w - T_{\text{cell}}}{\mathbf{\Delta r} \cdot \mathbf{n}} \tag{4.20}$$

since the role of normal vector appears in the denominator combined with the very small value of required grid spacing, small perturbations do lead to large axial variations in heat flux. Furthermore as this effect builds up on the temperature difference between wall and adjacent cell this seems to result in a divergent amplification mechanism.

The amount of deformation we induce on nodes are outcomes of an approximate solution of a complex non-linear problem on a discretely represented geometry, and as one might expect they do not necessarily follow a distribution such that the resultant shapes have G1 continuity that would yield a smooth derivative for unit normal vectors. The problem is such that even the slightest disturbance in the distribution of unit normal vectors get amplified, and with the implementation of the moving average filter we suppress the oscillations, and reduce their growth. However, the cause remains. It appears that eliminating this probable root cause of this instability goes through devising filtering or curve fitting methods such that the evolution of geometry in successive time steps yield a high quality curve with at least G1 continuity.

4.7 Grid Deformation Strategy and Limitations

In Section 4.2 the value of $\dot{s}$ was computed at face centroids. However the user defined grid motion, that has been implemented through the `DEFINE_GRID_MOTION` macro requires to specify the individual position of nodes laying on the nozzle wall. Therefore, at each time step $\dot{s}$ values that are available on face centroids are averaged to compute nodal values, as well as the unit normal vectors also defined on face centroids.

The locally computed values of recession rates are for the motion of surface towards

the local normal direction as in the burnback of a solid propellant grain. For relatively small extent of deformations the local tracking method employed here works very well and it is believed to be suitable for a very large portion of practical ablation problems for rocket nozzles. The limitation comes due to the possible collapse of convex geometrical features into a point, which inevitably causes the nodes forming that particular feature to merge. If number of nodes are kept constant as in this work, this poses a limitation for the extent of deformation. An example illustrating this limitation is given in Figure 4.17.

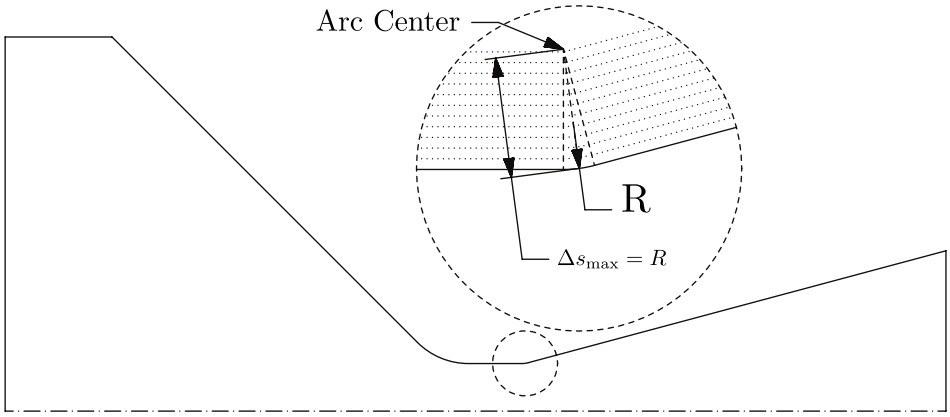

Figure 4.17: Illustration of loss of feature on a representative nozzle geometry.

FLUENT offers many algorithms to compute the interior motion of nodes that are present within zones with moving boundaries, and has the option to deform the adjacent boundary layer cells with the same velocity vector applied on boundaries. This latter option is especially useful to keep the y^+ value within required ranges throughout the analysis. The motion of interior nodes are left to be computed with the spring analogy along with laplacian smoothing. The resultant final grid along with the initial grid showing the deformed region near throat is given in Figure 4.18. Figure 4.18 has been constructed from the conjugate analysis presented in Chapter 5.

4.8 Considerations Regarding Parallel Computation

Many practical engineering problems involving the use of charring ablators require very fine grid systems leading to a severe increase in computational time if solved on a

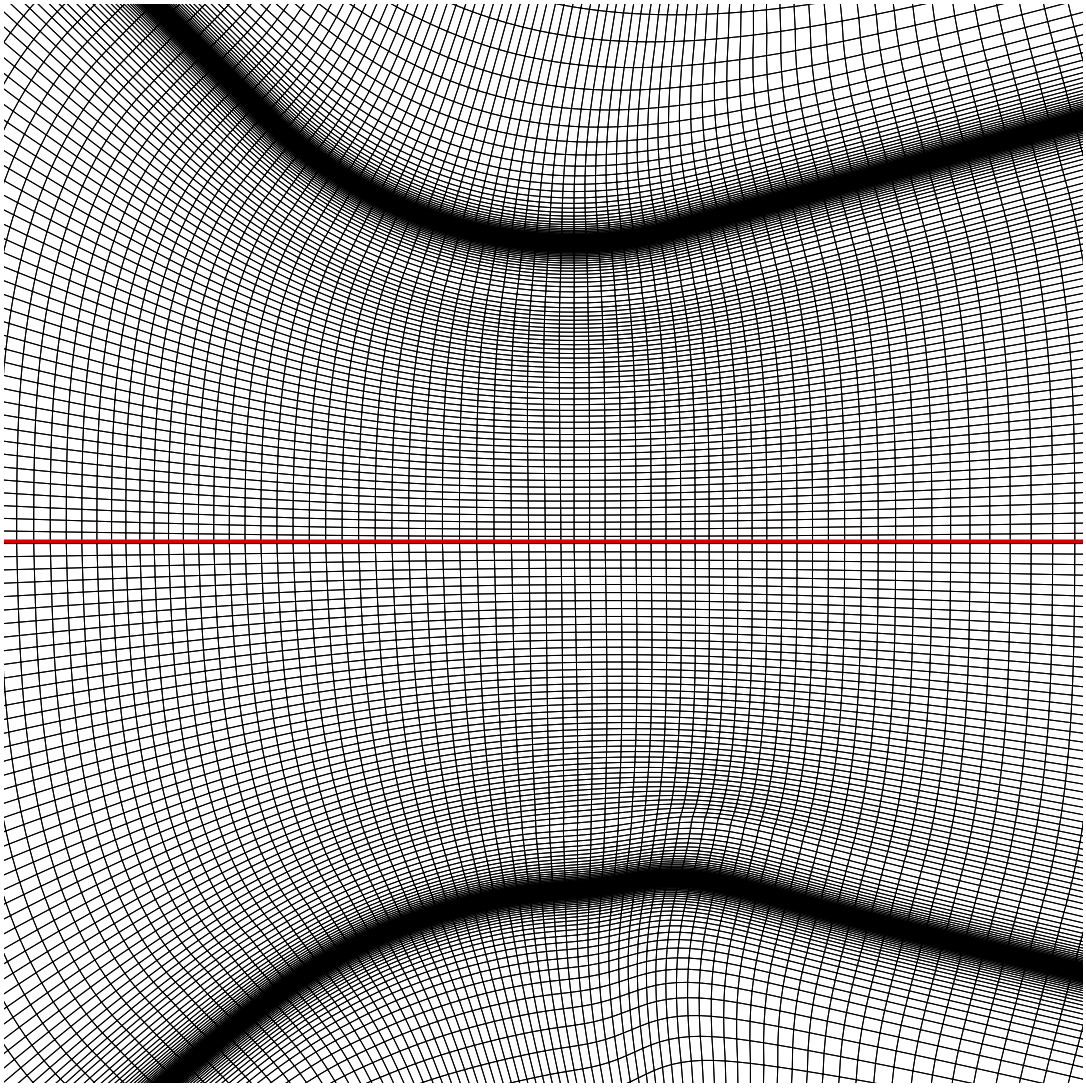

Figure 4.18: Comparison of inıtıal grid (top) and final grid (bottom).

single CPU. The parallelization of a particular solver is mainly based on partitioning of the problem and providing necessary implementations for data transfer between each partition to be handled on different CPU's. In this work no special efforts are given to the parallel implementation of the charring ablation model to FLUENT and considered beyond the scope. However, parallel computation is possible with decreased efficiency if solution domain is manually partitioned. To accomplish this, the solid zone where the charring ablation takes place and the first cell of the adjacent fluid zone should be located within the same partition. This way the implementation works within a single computing node and rest of the domain can be partitioned manually to allow parallel computing. In fact all solutions presented in this work are carried out with the partitioning method described here.

CHAPTER 5

RESULTS

5.1 Validation of KAYMAK with Data Available in Literature

Since both KAYMAK and FLUENT Implementation rely on the same governing equations, the validation cases included in this section are considered as applicable to both. After presenting the validation of KAYMAK, proceeding section investigates to verify the implementation in FLUENT based on comparison with KAYMAK.

5.1.1 Validation of In-Depth Analysis Capability

The data available in [1] is among the rare sources found in literature providing solution data for in-depth temperature and density profiles involving silica-phenolic, including solutions performed with industry standard CMA3 [23]. All the required detailed input for analysis is available. However this case uses an external recession rate as a function of time and constant surface temperature as the boundary condition for ablating surface, hence it does not serve as a validation tool for the computations regarding recession rate. On the other hand this creates a perfect validation case to verify the implementation of in-depth solution capability in KAYMAK since the heat flux entering the domain is fixed.

A schematic for the case is given in Figure 5.1 and the boundary conditions are stated in Table 5.1. The initial condition is given as uniform 299.15 K. The data for the pyrolysis resin decomposition kinetics is given in Table 5.2. The temperature dependent material properties are given in Figure 5.2 and the externally specified recession rate for the ablating surface is given in Figure 5.3.

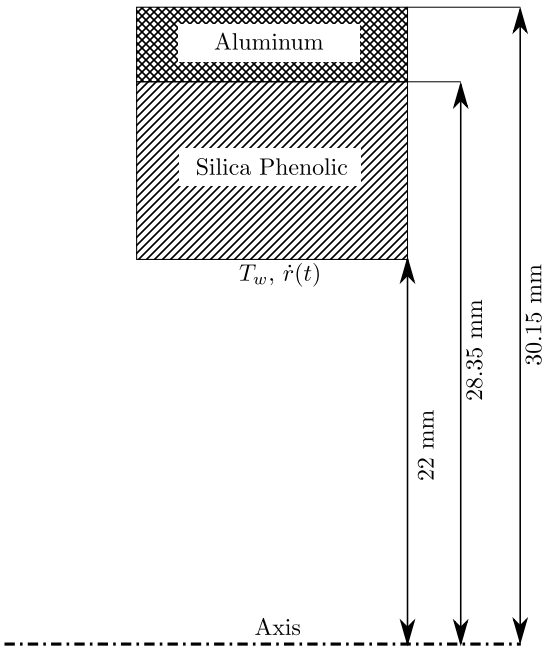

Figure 5.1: Schematic of validation case, adopted from [1].

Table 5.1: Summary of boundary conditions for validation case, adopted from [1].

Time [s]	**Receeding Surface**	**Back Surface**
0-5	$T_w = 2473$ K, $\dot{r} = f(t)$	$T_\infty = 293.15$ K, $h = 26$ W/m^2/K, $\epsilon = 0.05$
5-95	$\epsilon_w = 0.6$, $T_\infty = 473.15$ K	$T_\infty = 293.15$ K, $h = 26$ W/m^2/K, $\epsilon = 0.05$

KAYMAK analysis were performed with a timestep of 1 ms on three different grid sizes employing 20, 60 and 120 cells. The overall integral output of this analysis is the temperature of the outer surface and comparison of KAYMAK results with those present in [1] for CMA3 and G2DHeat is given in Figure 5.4.

As shown in Figure 5.4, excellent agreement has been obtained on exterior surface temperature. Since no details regarding a grid dependence study is present [1], the discrepancy present in the CMA3 solution may be attributed to insufficient resolution. Comparison of in-depth temperature and density profiles for $t = 5$ and $t = 10$ s are given in Figures 5.5 and 5.6 respectively.

As illustrated in Figures 5.5 and 5.6, agreement of in-depth profiles is also satisfactory. However the results given in [1] indicated as markers indicate a quite coarse grid

Table 5.2: Summary of chemical kinetics data for pyrolysis reaction in silica-phenolic, adopted from [1].

	E [J/kmol]	**A [1/s]**	**n**	ρ_0 **[kg/m^3]**	ρ_r **[kg/m^3]**	T_{pyr} **[K]**	Γ_V
Component A	71.14×10^6	1.4×10^4	3	325.015	0	333	0.422
Component B	169.98×10^6	9.75×10^8	3	973.926	518.998	550	0.422
Reinforcement	-	-	-	2066.380	2066.380	-	0.578

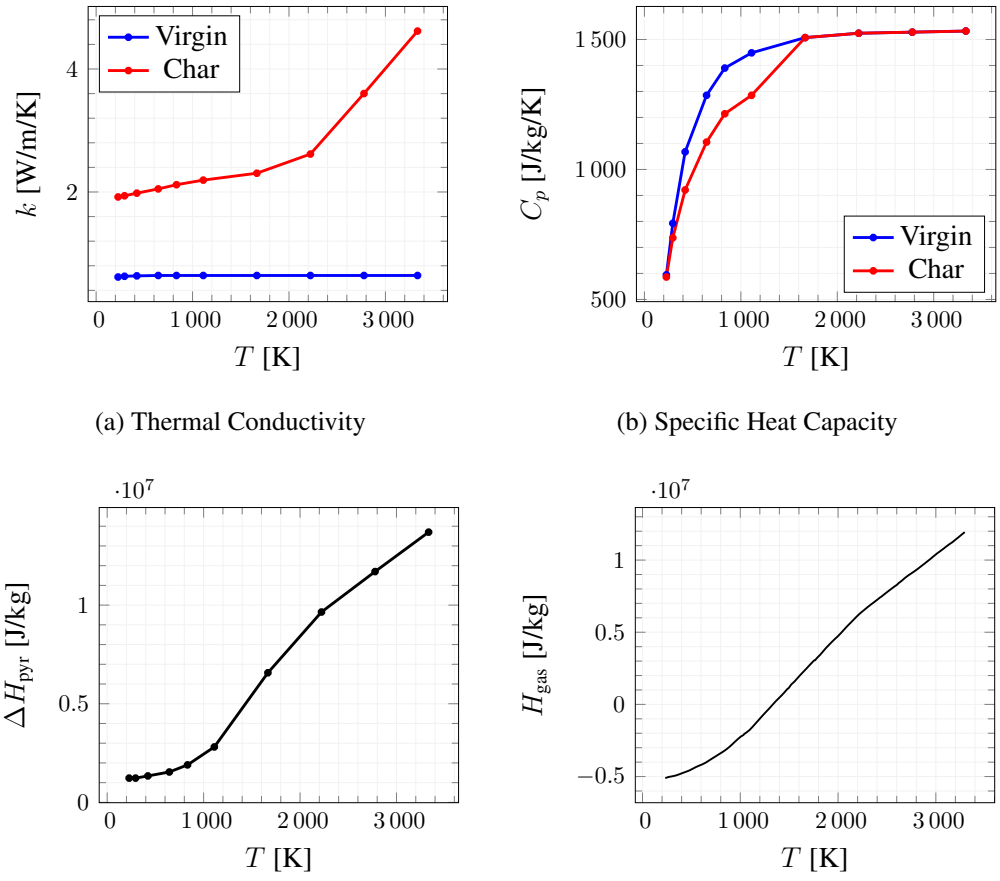

(a) Thermal Conductivity

(b) Specific Heat Capacity

(c) Heat of Pyrolysis

(d) Pyrolysis Gas Enthalpy

Figure 5.2: Summary of temperature dependent material properties [1].

resolution, which is most probably one of the reasons of minor discrepancies. It might be useful here to state that once this kind of boundary condition is specified for the ablating surface, the energy input to the domain will be fixed. This allows to study the implications of parameters such as char thermal conductivity and its temperature de-

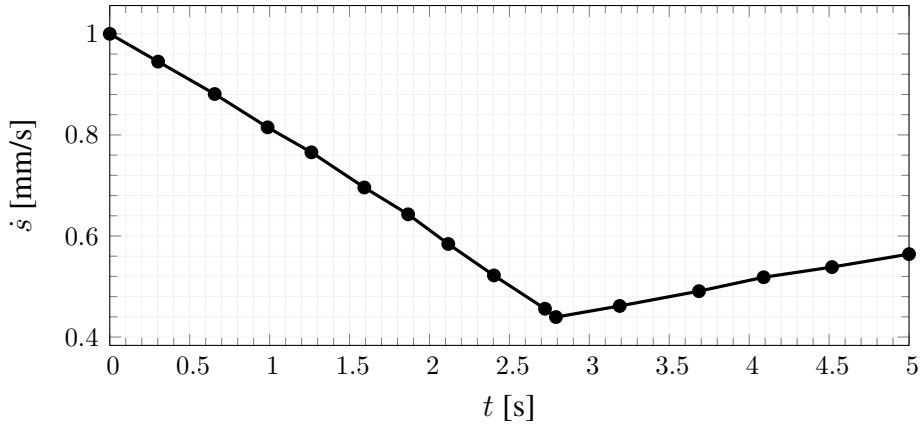

Figure 5.3: Externally specified recession rate versus time for validation case [1].

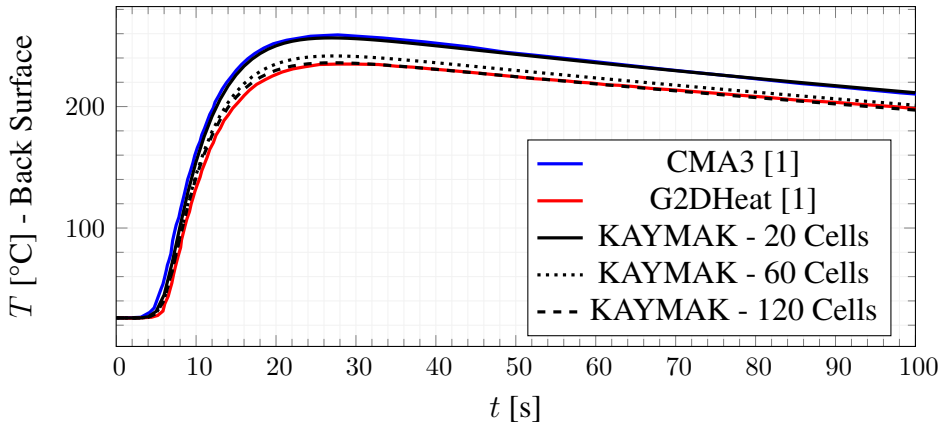

Figure 5.4: Comparison of results for exterior surface temperature.

pendence and appropriate boundary conditions for cool-down phase in detail against experimental data. This feature is one of the most widely usage case in industry as indicated in literature.

5.1.2 Validation of Ablation Treatment

The test campaign conducted in Nasa Lewis Research Center during 1970's [3] provides an extensive database about the thermal response and recession rate values for silica-phenolic designated as MXS-89 nozzles tested in an arc plasma generator facility at various conditions. The goal of campaign was to successively perform sub-scale nozzle tests under simulated thermal and chemical conditions of a liquid rocket en-

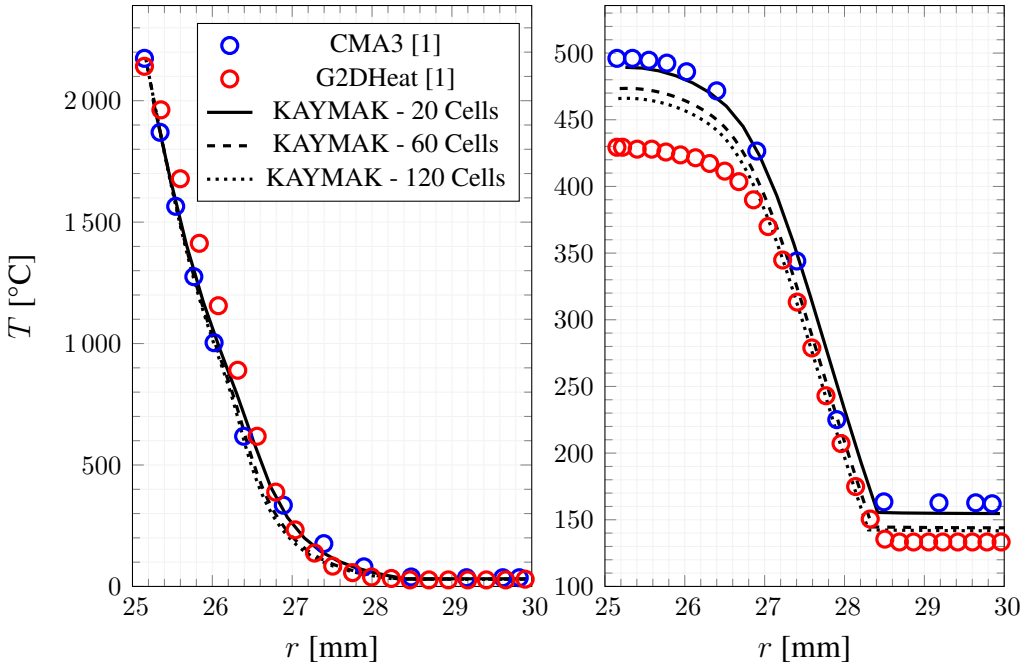

(a) t =5 s (b) t =10 s

Figure 5.5: Comparison of results for in-depth temperature profiles.

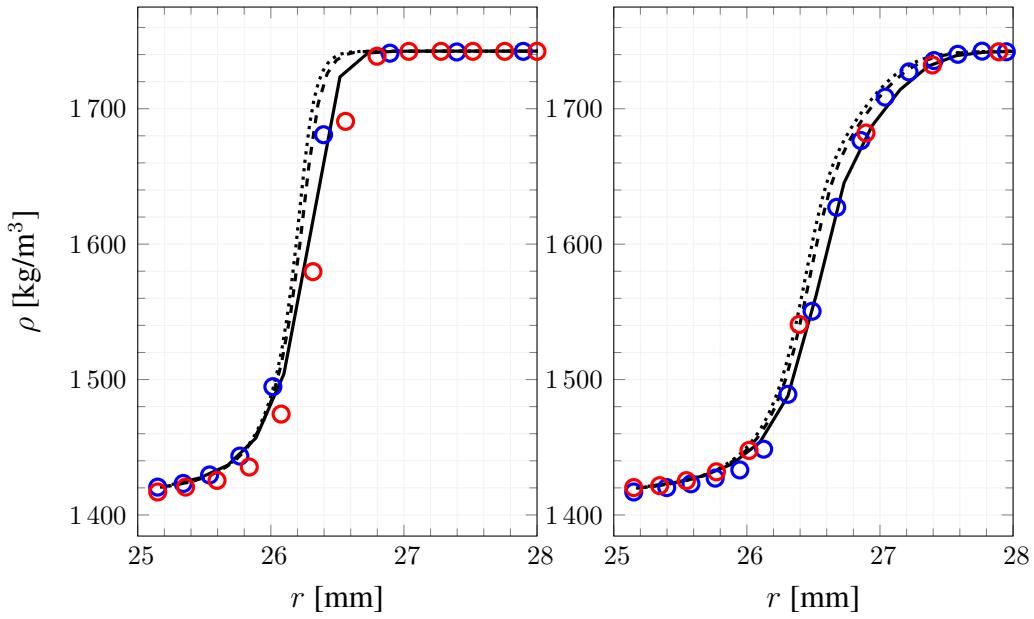

(a) t =5 s (b) t = 10 s

Figure 5.6: Comparison of results for in-depth density profiles.

gine utilizing N_2O_4 - N_2H_4/UDMH propellant. This same database has also been used as a validation case in [17].

The data supplied in [3] also includes the derived heat transfer coefficient values and their comparisons to those computed with Bartz correlation, which illustrate a value of C_{Bartz} about 0.5 depending on operating conditions of arcjet. The availability of such data serves as an excellent tool to validate the surface energy balance implementation, since we will not deal with the possible inaccuracies caused by the evaluation of convective heat flux. Also inspection of the data related to MXS-89 silica-phenolic given in [3,19] and previously considered values for the validation case in the previous section, we conclude that the parameters describing the pyrolysis of phenolic resin used in both of them are essentially the same values.

It is common in literature to express the thermal conductivity of partially degraded material in terms of certain blending functions. While this has not been introduced before, and a linear blending dependent on degradation parameter has been used as in Equation 2.28, thermal conductivity for MXS-89 silica phenolic material was given in the form below. The corresponding blending functions are given in Figure 5.7. To include this effect, KAYMAK has been modified to include blending functions.

$$k = f_1(x)k_{\text{v}} + f_2(x)k_{\text{c}} \tag{5.1}$$

The blending functions f_1 and f_2 are generally used to adjusted to reproduce experimental results, while virgin thermal conductivity can be easily measured, char thermal conductivity is generally obtained based on such inverse methods. In fact, it is outlined in [23] that a major task of analysis software such as CMA is to construct values for char thermal conductivity and its dependence on temperature using the specified recession rate and surface temperature option as these two quantities can be more or less measured. As there is plenty amount of information regarding the corresponding mixture mass fractions related to the considered test database in [17], it has been considered beneficial to work on one of the same three test cases considered in [17], and test case 1129 was considered. Since the formulation of convective heat transfer in KAYMAK is based on temperature difference driving potential instead of the enthalpy driving potential of the Stanton number formulation, we need the explicit value of C_p at the boundary layer edge. Using the composition mass fractions in [17],

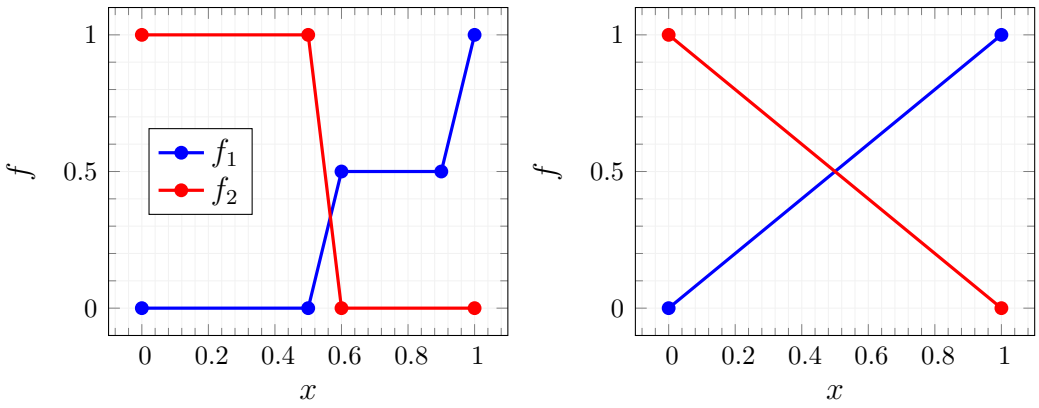

(a) Data for MXS-89 [3].

(b) Linear Blending

Figure 5.7: Thermal conductivity blending functions for MXS-89 given in [2] (left) and blending functions corresponding to default linear blending (right) introduced before.

which are not repeated here, the required values of $C_{p,e}$, Pr and γ for the calculation of recovery temperature and convective heat transfer coefficient are calculated utilizing NASA CEA [57].

To perform analysis, we initially construct all required material properties from data related to MXS-89 silica phenolic given in [19] and [3]. Since some of temperature data did not cover all of the required temperature ranges, cubic extrapolation has been performed where necessary. One other source of possible uncertainty related to the computed recession rates is the char swelling. Char swelling is the phenomenon that is the increase of char volume, sometimes resulting as negative surface recession measurements. The tests numbered as 1349, 1337 and 1116 in [3] illustrate this phenomena. Therefore, based on the possibility that for the cases in which significant amount of surface recession has occurred may also include a certain amount of char swelling, an uncertainty can be expected. A drawing of MXS-89 nozzle insert used in [3] is given in Figure 5.8.

As the value of the inner diameter value to compute material thickness is missing, it is measured from Figure 5.8 as 37 mm. This value is not critical since the conduction of heat does not even reach these sections within the duration of test. The summary of material properties for MXS-89 is given in Table 5.3.

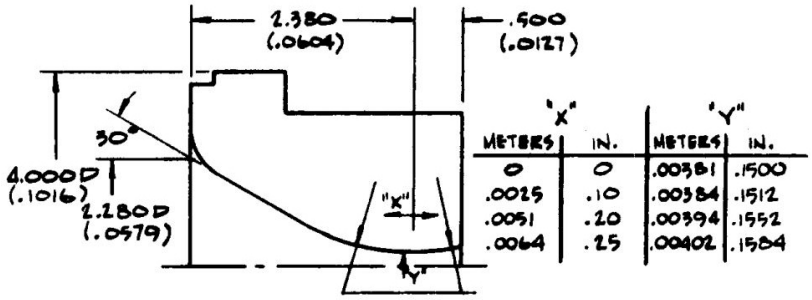

Figure 5.8: Cross-section of nozzle insert [3].

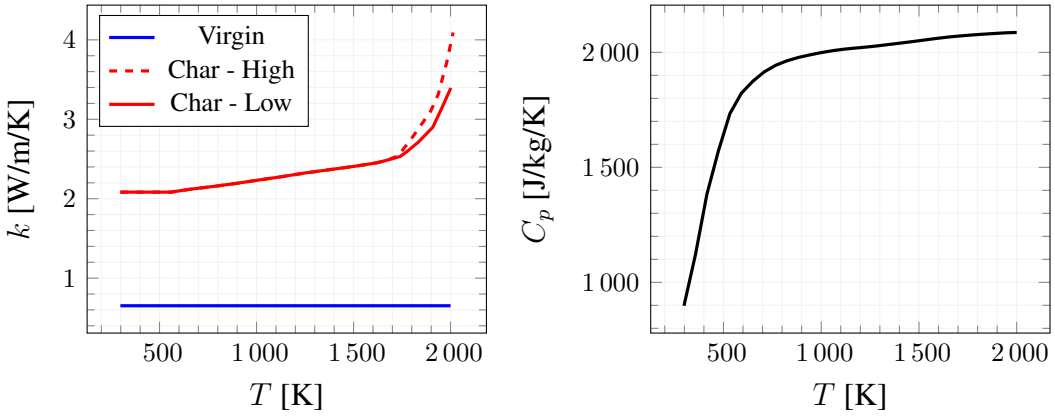

(a) Thermal conductivity.

(b) Specific heat capacity (Same for virgin & char).

Figure 5.9: Temperature dependent material properties for MXS-89 [3].

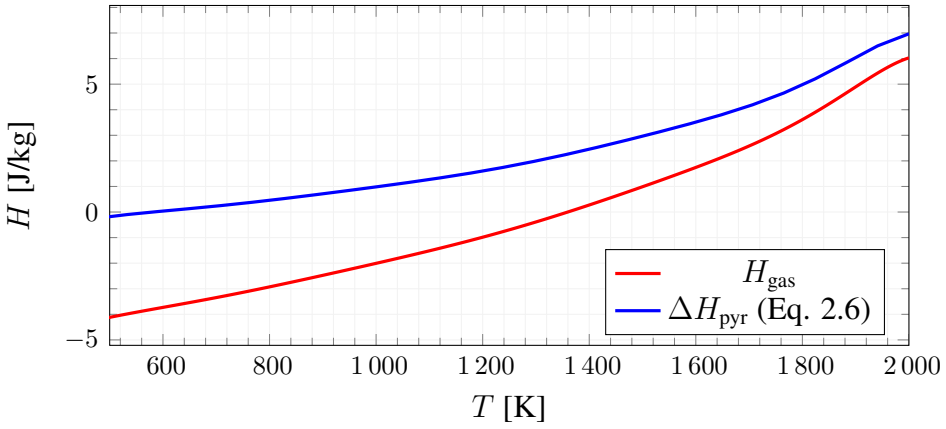

Figure 5.10: Pyrolysis gas enthalpy and heat of pyrolysis for MXS-89 [3].

Table 5.3: Summary of MXS-89 silica phenolic material properties [2, 3]

Parameter	Value
ρ_{v}	1678.73 kg/m^3
ρ_{c}	1371.18 kg/m^3
$\rho_{0,\text{A}}$	973.12 kg/m^3
$\rho_{\text{r,A}}$	518.99 kg/m^3
$\rho_{0,\text{B}}$	324.21 kg/m^3
$\rho_{\text{r,B}}$	0 kg/m^3
ρ_{R}	1927.02 kg/m^3
Γ_M	0.305
Γ_V	0.395
A_{A}	9.76×10^8 1/s *
A_{B}	1.4×10^4 1/s
E_{A}	169.98×10^6 J/kmol
E_{B}	71.13×10^6 J/kmol
$\Delta H_{\text{f,v}}^{298.15}$	-11.295 MJ/kg
$\Delta H_{\text{f,c}}^{298.15}$	-12.886 MJ/kg
$C_{\text{p,v}}(T)$ and $C_{\text{p,c}}(T)$	See Figure 5.9
$k_{\text{v}}(T)$ and $k_{\text{c}}(T)$	See Figure 5.9
$h_{\text{gas}}(T)$ and $C_{\text{p,gas}}(T)$	See Figure 5.10
$\Delta H_{\text{pyr}}(T)$	See Figure 5.10
ϵ_{c}	See below note. **
ϵ_{v}	See below note. ***

* The value was given for a different form of Equation 3.28, therefore adjusted to match the form of Equation 3.28.

** No explicit value was found in literature for MXS-89. Reflectance data for MXS-89 in [65] suggests a high emmisivity value. Data in [1] suggests a value of 0.6 for a different silica-phenolic.

*** No explicit value was found, assumed to be equal to half of char emissivity for each analysis.

The char enthalpy has been computed as defined in Chapter 2 based on char heat of formation and specific heat capacity data given in Figure 5.9. For the computation of heat flux due to re-radiation, assumption regarding the same case in [17] has been used and all emitted radiation is considered to be absorbed by the gaseous medium, and surface-to-surface effects are hence neglected. The relatively low value of convective heat flux tremendously increases the sensitivity of the total recession rate to the heat loss via re-radiation mechanism and value of char thermal conductivity. Since there is two different set of data present for char thermal conductivity, both of them are used in analysis. The time dependent heat transfer coefficient data for Test 1129 is given in Figure 5.11. Since data was given in terms of enthalpy driving potential, the value of h in Figure 5.11 was computed by multiplying this value with the theoretical value of C_p at throat core flow. It has been observed that given data corresponds to approximately $C_{\text{Bartz}} = 0.7$.

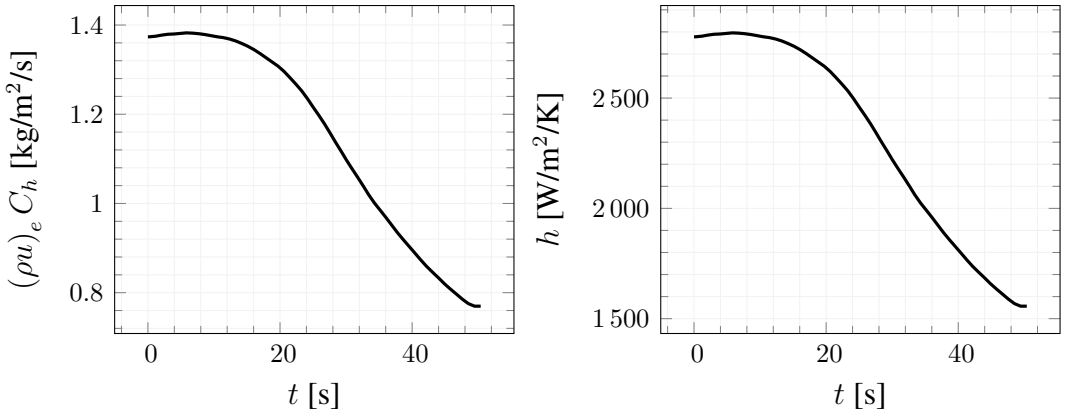

Figure 5.11: Time dependent heat transfer coefficient data for Test 1129 [3].

Authors of [3] has also given the inferred throat diameter history based on post-firing measurements and a regenerated throat diameter history based on pressure decay as given in Figure 5.12.

The initial decrease of throat radius in Figure 5.12 suggests that char swelling has occurred with a corresponding magnitude of approximately 0.2 mm in radius.

It has been observed from Figure 5.13 that the computed value of recession rate is very sensitive to the amount of heat radiated away from the surface. This is an expected situation, since the magnitude of convective heating rate is about an order of

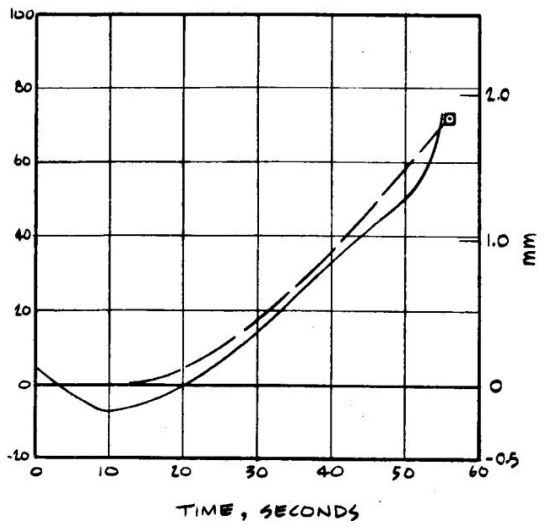

Figure 5.12: Throat recession (radius) vs. time for Test 1129 [3]. Solid line is throat diameter reconstructed from pressure decay, dashed line is inferred average recession.

magnitude smaller than those present in typical SRM's. This relatively low value of the driving potential causes the relative value of the re-radiation term $\epsilon_w \sigma T_w^4$ against convective heat flux to increase. Despite the uncertainties the overall agreement is good suggesting the implementation of surface energy balance method is successful. For the remaining data presented in this section, low char thermal conductivity value will be used as differences are quite insignificant.

Comparison of computed char depth and measured char depth is given in Figure 5.14. As there is no definitive quantitative method stated in [3] for the measurement of char depth, an illustration has been given as a comparison with the degradation parameter x.

The measured temperature data from thermocouples located within the nozzle insert and comparison with computed temperature values for their locations is given in Figure 5.15.

Judging from Figure 5.15, a good agreement has been obtained for the deepest thermocouple, TC3. The discrepancy starts to increase towards the closest thermocouple to surface, TC1. In [2] authors have considered a method based on a pre-specified liquid layer thickness coupled with equilibrium surface thermochemistry and a model for the silica-carbon reaction zone present towards the end of char, close to the heated

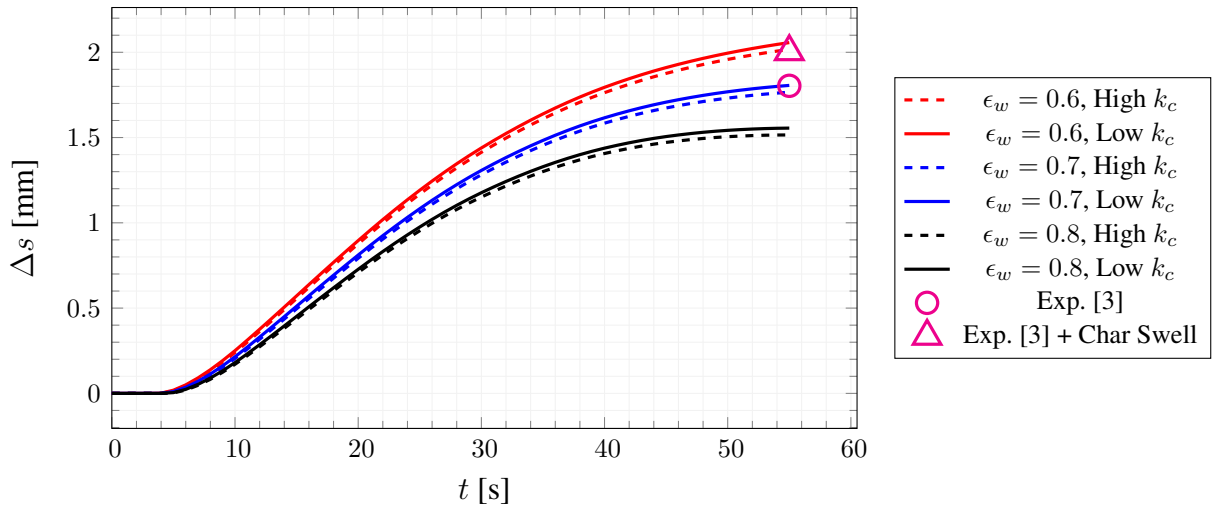

Figure 5.13: Comparison of measured throat recession for Test 1129 [3] and computed values for different values of char emissivity.

surface. With this method the temperature values inside the material can exceed 1996 K and would allow for aforementioned effect to pronounce. This rare experimental data illustrates that the temperature within silica-phenolic can exceed the melting temperature of SiO_2, and carbon-silica reactions may be required to be considered in detail for certain cases, which is not common in literature yet.

5.2 Verification of FLUENT Implementation

The simple validation case presented in Section 5.1.1 has been considered to verify the implementation of in-depth analysis capability in FLUENT. As discussed before C_{p} can only be defined in terms of temperature within FLUENT, hence the solution of the validation case has been repeated in KAYMAK with $C_{\text{p,v}} = C_{\text{p,c}}$ to allow comparison on equivalent grounds. Solution up to $t = 5$ s is performed with a timestep size of 1 ms in both softwares. The FLUENT solution has been carried out on the grid system shown in Figure 5.16 and the externally specified recession rate is supplied to the heated surface along with a constant temperature boundary condition of 2473 K. KAYMAK analysis was run with 60 cells.

The in-depth distribution of temperature and density are compared to those computed

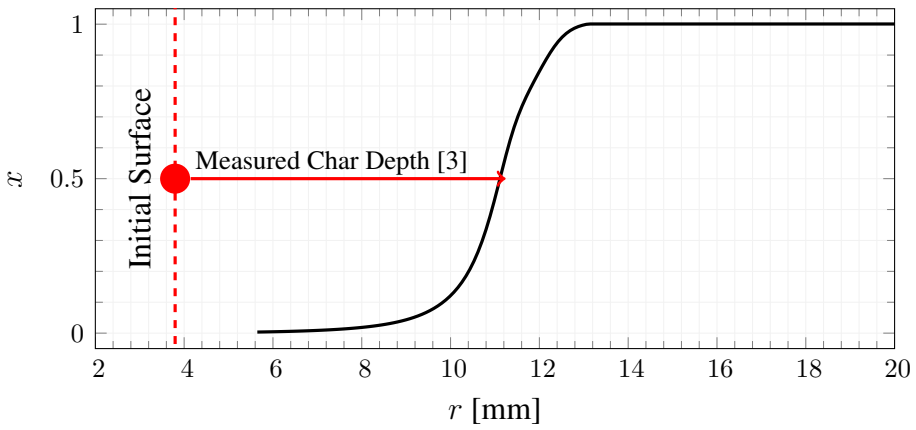

Figure 5.14: Comparison of computed and reported char depth in [3] for Test 1129.

by KAYMAK. Comparison of solutions are given in Figures 5.17 and 5.18.

While quite good agreement has been demonstrated in Figures 5.17 and 5.18 for both in-depth temperature and density profiles, certain discrepancies are present in the active decomposition zone. Since the numerical implementation of decomposition treatment and grid convection are identical in both, this minor difference is suspected to be related to the solution of energy equation, internal treatment of source terms and temporal integration scheme involving a dual-time iteration scheme. Exact reason is unknown. However since discrepancies are quite small, the implementation of in-depth analysis of charring in FLUENT is considered as successful.

5.3 Conjugate Analysis Coupled with Interior Ballistics and Experimental Results

A static firing test has been conducted with a small scale BEM (Ballistic Evaluation Motor) employing a silica-phenolic nozzle insert. The final values of recession and char depth among the nozzle axis are attempted to be reconstructed by the methods developed in this work. Pressure and thrust measurements obtained from the firing test are also attempted to be reconstructed with coupled interior ballistics analysis.

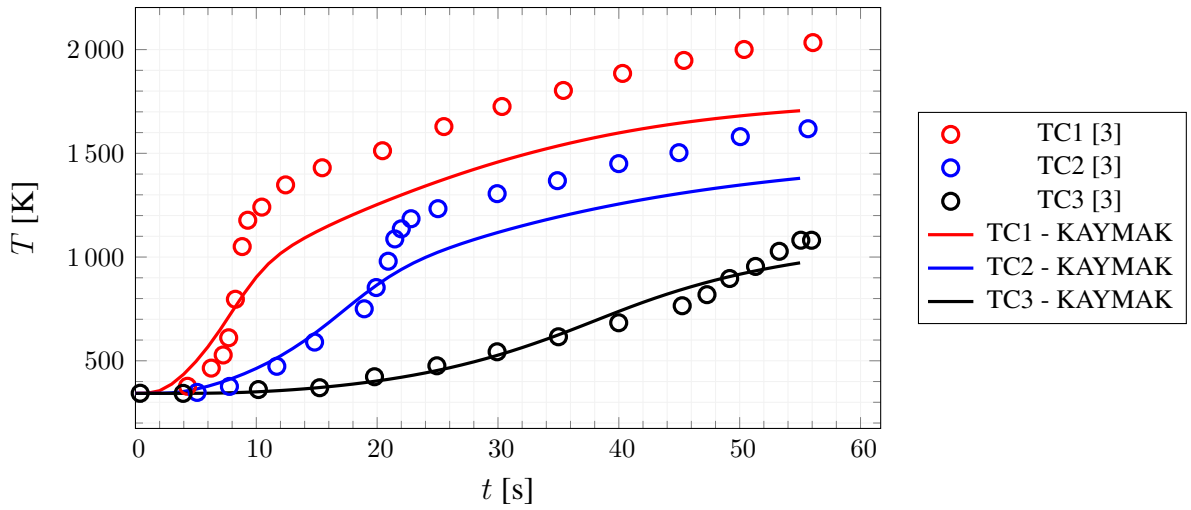

Figure 5.15: Comparison of computed and measured [3] in-depth temperature values. Given data is for $\epsilon_c = 0.7$ and low char thermal conductivity.

5.3.1 Definition of Test Article

The test article is a small scale test motor that contains approximately 600 grams of a typical non-aluminized composite solid propellant. Detailed properties of the propellant are not included here due to the sensitivity of information. Propellant grain is an axially symmetric grain with a circular port at all sections and has 45°conical sections at the beginning and end portions. The ratio of port area is large, leading to very low Mach numbers within port. Combined with a grain $\frac{L}{D}$ of approximately 2, it provides a very suitable case for zero dimensional interior ballistic treatment. The grain provides an approximately constant burn area throughout its regression within $\pm$ 2.5% of the mean value. Ignition is achieved by means of a pyrotechnic igniter located at the head-end of the motor. This configuration has been tested many times with different nozzle configurations and provides excellent repeatability in terms of interior ballistics performance. Firing is done on a static test bench, head-end pressure data and thrust data is acquired by means of high accuracy transducers. The measured head-end pressure will be treated as the total pressure within motor as it experiences negligible pressure drop within chamber and chamber conditions are nearly stagnant.

The nozzle consists of a thick walled steel housing that is threaded to motor case and houses a silica-phenolic insert whose geometry is given in Figure 5.19 and Table 5.4

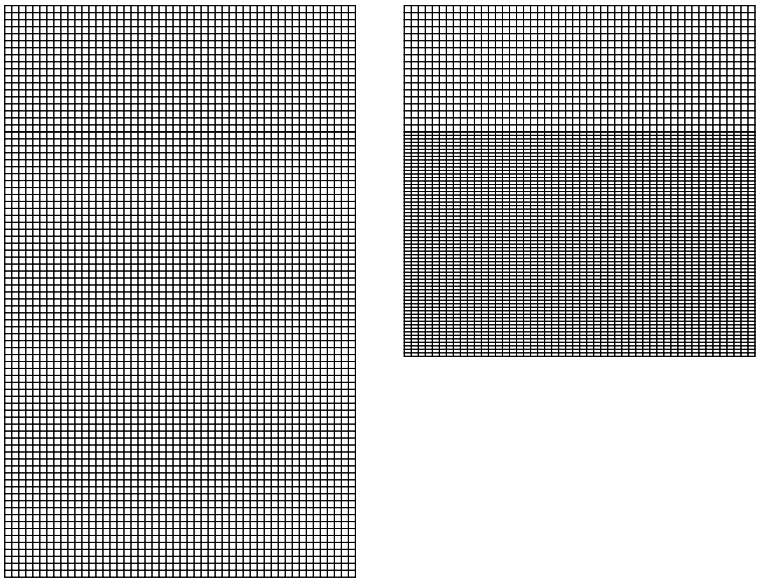

Figure 5.16: Grid system used in FLUENT. Initial grid (left) and final grid (right) at $t = 5$s. 64 cells in radial direction.

which forms the nozzle internal contour. The insert was machined from a cylindrical billet in which laying direction of silica cloth is perpendicular to its axis. Two sets of inserts has been machined successively with identical machining procedures and tools, and one of them is mechanically cut in half for inspection. It has been assumed that both of produced inserts are identical in terms of interior profiles. The throat diameter of the nozzle to be fired has been measured with an optical projection device to obtain a throat diameter value of 8.93 mm within at least 0.01 mm accuracy.

5.3.2 Silica-Phenolic Nozzle Insert Properties

The limiting issue for the comparisons presented in this chapter is the fact that there is a limited amount of information available related to the silica-phenolic nozzle insert that has been tested. While considered beyond the scope of this thesis, certain characterization efforts has been carried out to supply input data for analysis. Finally a set of data combined with those available in literature for the missing information has been used.

The measurement of virgin material density with a gas pycnometry device that uses

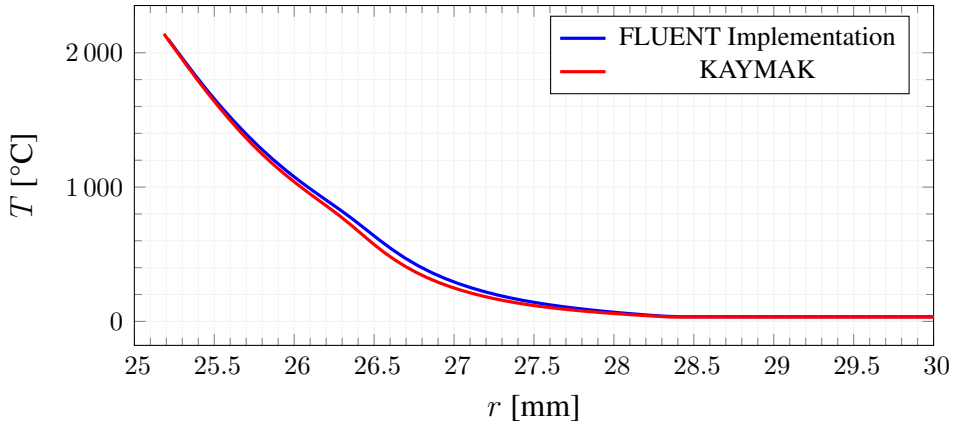

Figure 5.17: Comparison of in-depth temperature profiles at $t = 5$s.

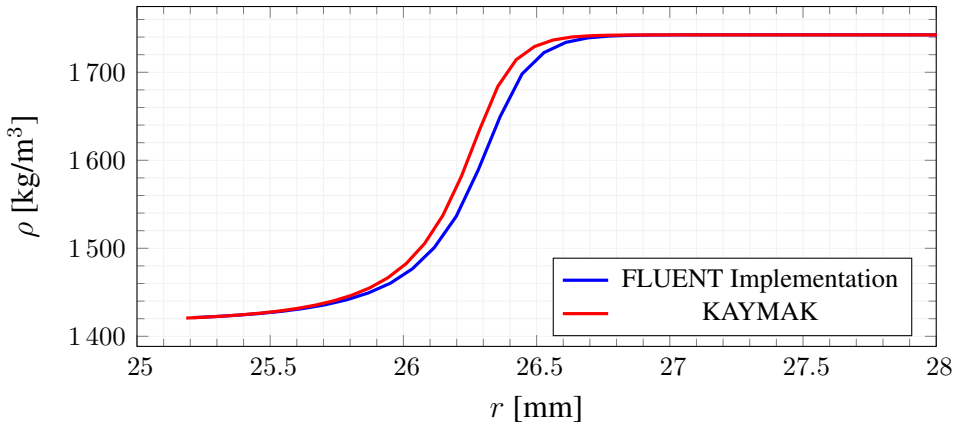

Figure 5.18: Comparison of in-depth temperature density at $t = 5$s.

inert-gas such as helium as a displacement medium yields a density value of 1816 kg/m^3. Based on this value, if Equation 2.31 is used to obtain the reinforcement density using the phenolic resin density $\rho_{0,\mathrm{A}} + \rho_{0,\mathrm{B}} = 1298.9$ kg/m^3 available in literature, the obtained results for reinforcement density almost exactly reproduces the value of the silica cloth used in production whose density is also independently measured as 2270 kg/m^3 with pycnometer. The result of this cross check can be considered as a sanity check for the value of resin density adopted from literature.

To obtain the bulk density of the test article, machined test article is weighed and a density value is calculated based on its volume. The obtained result is 1424 kg/m^3, which is significantly lower than than of the value obtained from pycnometer. The reason is believed to be the fact that pycnometer fills the possible porosity within

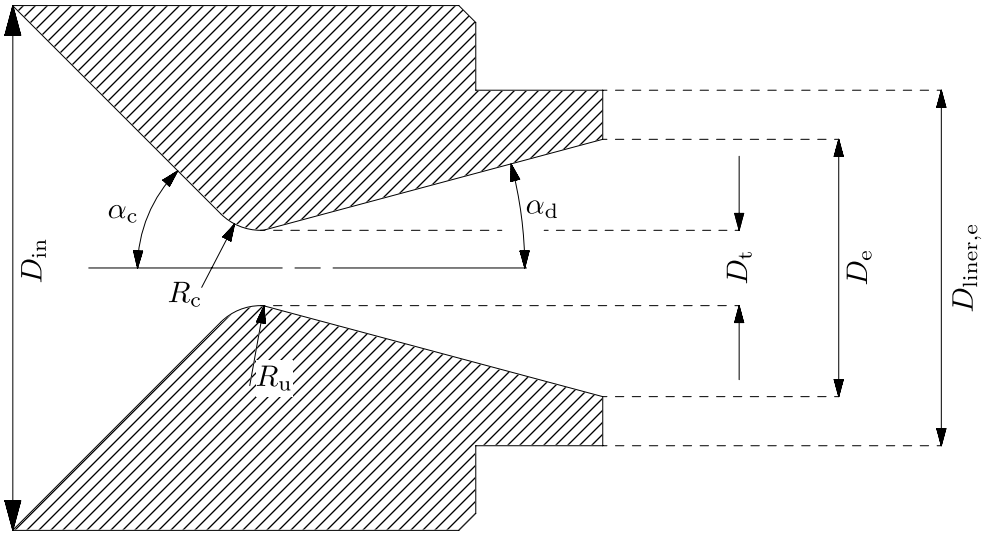

Figure 5.19: Cross section of nozzle insert and geometrical parameters.

Table 5.4: Geometrical parameters defining the nozzle geometry.

Parameter	**Explanation**	**Value**
D_{in}	Convergent section entrance diameter	66 mm
D_{t}	Throat Diameter	8.9 mm
D_{e}	Exit Diameter	30.4 mm
$D_{\mathrm{liner,e}}$	Diameter of liner at nozzle exit	42.7 mm
R_{c}	Throat Upstream Radius	6.675 mm
R_{u}	Throat Downstream Radius	2.225 mm
α_{c}	Convergent Half-Cone Angle	45°
α_{d}	Divergent Half-Cone Angle	15°

the material and gives the value of skeletal density. This suggests that there is a serious portion of void within the test article, possibly related to production process. Available data within literature for silica-phenolic materials with similar resin mass fractions report bulk density values about 1700 kg/m^3.

Following the method to derive the reinforcement density described in [3], a rather low value as 1501.85 kg/m^3 is obtained and has been used in analysis presented in this chapter. It has to be noted here that the value of char density is one of the primal factors deriving the recession rate of material. Higher virgin density obviously results as a higher char density, and higher char density results as lower recession rates when subjected to identical heat loads.

The result of 3 TGA tests performed on samples indicated weight loss values about $\%15$. The discrepancy is believed to be due to certain inhomogenities between samples. Since the phenolic resin kinetics model has been adopted from literature [1, 3], the weight loss amount has been compared against TGA data as a cross check. Since the sizes of TGA samples obtained directly from nozzle inserts are several milligrams and miniscule in size, possible porosity and in those samples are considered negligible and effective reinforcement density has been taken directly equal to the density of cloth to reconstruct TGA curves, that is 2270 kg/m^3. With these values, weight loss curves obtained from TGA tests are computationally reconstructed with kinetics data adopted from literature and compared in Figure 5.20.

While there is a considerable amount of discrepancy present in Figure 5.20, it has been considered accurate enough to be used in analysis. However, a better agreement in the final weight fraction was desired to increase confidence in the char density. Part of the discrepancy in lower temperature ranges can be attributed to presence of a certain amount of moisture in specimen as it was not preheated to remove moisture. The best agreement has been obtained for 5°C/min case. This effort has been directed to verify the applicability of kinetics data present in literature for the test article. Having done this comparison, it has been considered adequate to use the value of char density for the bulk material 1133.47 kg/m^3 that results from the resolution of below equation with literature data.

$$\rho_{\mathrm{c}} = \Gamma_V \rho_{\mathrm{r,B}} + (1 - \Gamma_V)\, \rho_R \tag{5.2}$$

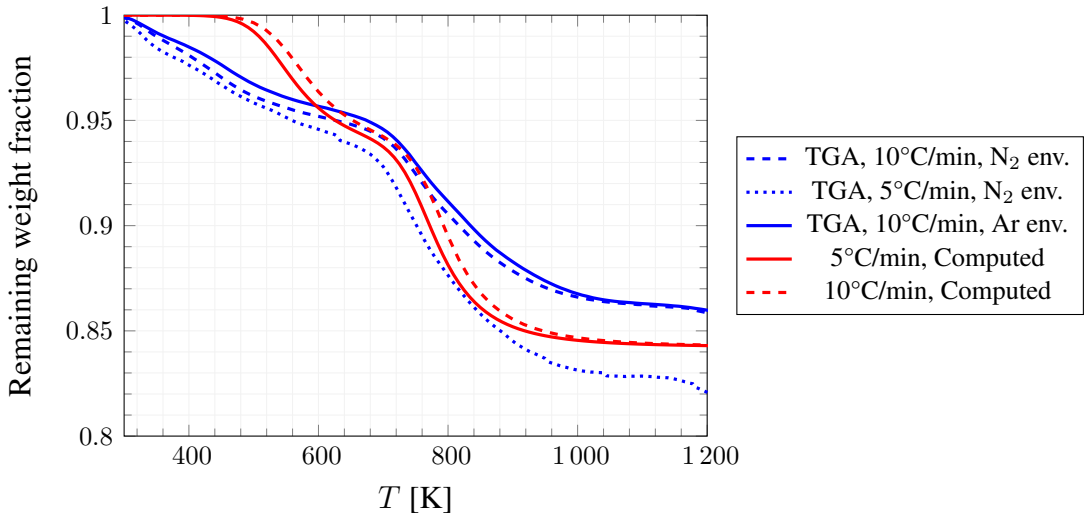

Figure 5.20: Comparison of weight loss curves obtained from TGA and computed by phenolic resin kinetics from literature.

Based on the data for the previously analyzed silica-phenolic materials, it has been assumed that the virgin thermal conductivity is independent of temperature and equal to the value given in Table 5.5. As this value was experimentally measured it is believed to be quite certain.

Since there is no available data regarding the specific heat capacity of virgin and charred material, the data for MXS-89 given in [3] has been used. The value for C_p is quite important since it is determines the effective heat of ablation through evaluation of char enthalpy. The enthalpy of formation values for SiO_2 in [3] and NASA CEA library are identical. However for the C_6H_6O resin molecule values given in two sources are significantly different, -1.0243 MJ/kg in NASA CEA library and -2.558 MJ/kg in [3]. The enthalpy of char is not affected, and virgin enthalpy is only slightly affected since it is dominated by the larger mass fraction of SiO_2.

For the extreme heat flux values present in the test conditions, the heat flux due to re-radiation is quite insignificant as contrast to the case investigated in Section 5.1.2. Same value that has been used in aforementioned section as $\epsilon_c = 0.7$ is used. The char thermal conductivity is also unknown. Based on the results obtained from early analysis, 2/3 of the values given in Figure 5.2 that has been adopted from [1] has been used. The factor 2/3 was derived from the ratio of the test articles measured virgin

Table 5.5: Properties for silica-phenolic nozzle insert

Parameter	Value	Source
Γ_M	0.35	Stated by producer
k_{v} at 21°C	0.46 W/m/K	Measured $\perp$ laying direction
ρ_{v}	1424 kg/m^3	See above discussion
ρ_{c}	1133.47 kg/m^3	See above discussion
H_{c} at 1996 K	-9.2682 MJ/kg	Computed as defined in Chapter 2.
ΔH_{melt}	0.16 MJ/kg	Obtained from NASA CEA library
ρ_R	1501.85 kg/m^3	See above discussion
Γ_V	0.3837	Computed with Equation 2.9
ϵ_c	0.7	Assumed
ϵ_v	0.35	Assumed
$C_{p,v}(T)$ and $C_{p,c}(T)$	-	See Figure 5.9
$k_c(T)$	-	See Figure 5.9 and above discussion.
H_{gas}	-	See Figure 5.10
ΔH_{pyr}	-	Computed as defined in Equation 2.5

state thermal conductivity and the virgin thermal conductivity given in Figure 5.2. Aside from the fact that the data adopted from [1] gave better agreements with test results rather than those adopted from [3], it was the most recently published source containing the sought information.

Following this discussion, the summary of silica-phenolic nozzle insert properties used in computations in the proceeding sections is given in Table 5.5.

5.3.3 Post-Firing Measurements

Initial measurement that has been conducted is the measurement of post-firing throat diameter with the optical projection device. Numerical results for post-firing throat diameter measurements is given in Table 5.6. After that the nozzle assembly has been cut in half with a mechanical saw approximately from its middle plane color optical

scanning has been done to investigate the char depth and extent of ablation in detail.

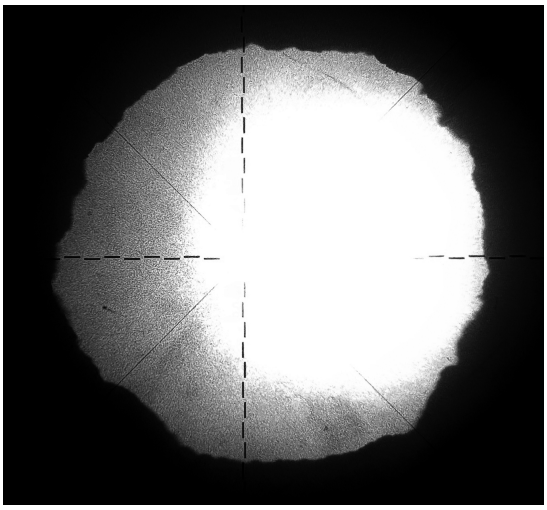

Figure 5.21: Post-firing optical projection of throat.

Table 5.6: Summary of post-firing throat measurements with optical projection.

Minimum Diameter	10.175 mm
Maximum Diameter	10.793 mm
Average Diameter	10.434 mm
Average Recession	0.752 mm

As shown in Figure 5.21, the resultant shape of throat is not symmetrical. This is a typical post-firing condition for a silica-phenolic nozzle and same phenomena is also shown in [3] with greater detail. Reason is probably due to unsymmetrical rate of ablation around the circumference of the throat. Another possible explanation is that the unsymmetrical appearance might be due to re-solidification of the molten SiO_2. A picture of entrance and exit sections of the post-firing condition of the nozzle is given in Figure 5.22.

The condition of exit section visible in Figure 5.22 shows remnants of melt layer flow. Sectional view of both unused and fired nozzles after they have been cut are given in Figure 5.23. An overall distribution of the extent of char can be observed as well as a possibly delaminated zone slightly downstream of the nozzle entrance.

Figure 5.22: Post firing condition of nozzle entrance (left) and exit (right). Left and right images are not within the same scale.

The planes generated on the color optical scanning shown in Figure 5.24 has been used to construct the post firing nozzle contours given in Figure 5.25.

As shown in Figure 5.25 the post-firing contours are almost identical for two selected cut planes. The theoretical CAD curve and pre-firing contour also match very well, with minor profile deviations along divergent part not exceeding 0.1 mm. The extent of ablation is about 10 mm upstream and 5 mm downstream of throat, and the apparent location of physical throat has shifted forward during firing.

5.3.4 Data Reduction

The goal of this section is to reconstruct the throat diameter history that best represents the experimental pressure-time curve. A previously developed method [66] by the author of this thesis allows to obtain the throat diameter history based on pressure and thrust measurements in static SRM firings. While the details regarding the derivation of this method will not be repeated here, it basically investigates the change in unit thrust per unit pressure. It has to be noted here that one of the assumptions related to this method is that there is a negligible change in nozzle thrust efficiency, it is not the case here. While the method works quite well for graphite nozzle inserts undergoing more conservative shape changes than investigated here, good insight related

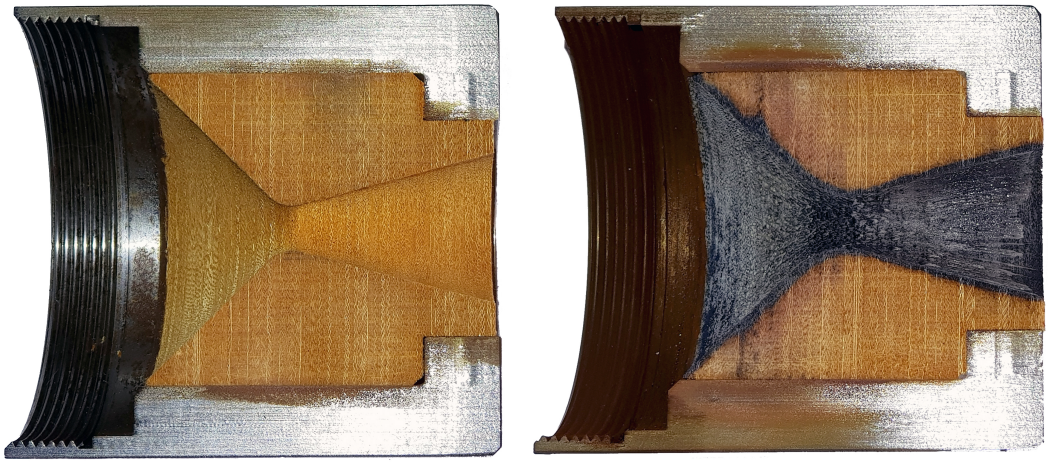

Figure 5.23: Sectional view of nozzles cut in half.

to the time dependent behavior of throat diameter can still be obtained with degraded numerical accuracy.

The burn rate of propellant vs. pressure is known at the firing temperature is known with a high amount of certainty. In fact, burn rate data used here has been obtained from the same motor configuration utilizing various graphite nozzle inserts to cover the required range of pressures. The required data for interior ballistic analysis related to propellant has been obtained by means of chemical equilibrium calculations with NASA CEA [57]. Previous experience has shown that for this configuration the observed average value of c^*, which can easily be measured for static firing tests, and theoretical equilibrium values match very well.

The obtained head end pressure-time and thrust-time curves are given in Figures 5.26 and 5.27 respectively. The suggested throat erosion rate employing the method in [66] produces the given output in Figure 5.28.

During initial reconstruction efforts, the initial spike present in Figure 5.28 was considered to be unphysical, however it has then realized that in fact a serious amount of throat recession already occurs before t =0.1 s, as suggested by the spike. The magnitudes suggested by the spike are very high for this kind of material, and initiation of melting ablation that quick is very much against the expectations. As the pressure-time curve suggests, the onset of throat recession starts around t =0.2 s and

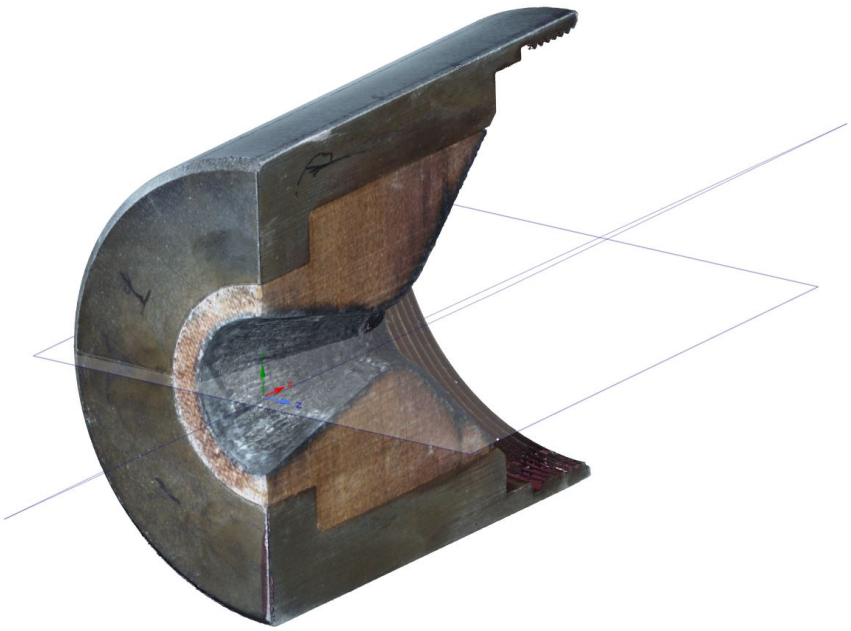

Figure 5.24: Planes used to construct post firing nozzle contour form optical scanning data.

then attains a quasi-steady recession rate around t =0.6 s. However the initial rapid recession is very much physical and most possibly related to the compression of the nozzle insert under pressure. This occurrence might be further related to the large void fraction discussed in the previous sections. Since this kind of phenomena is beyond the methods studied in this work, the effect of this initial spike was included in all following analysis by increasing the initial throat diameter to 9.17 mm. Based on this fact and investigating the approximate recession curve given in Figure 5.28, a simple throat recession rate linear interpolation lookup table was generated to reproduce the pressure-time curve via interior ballistic analysis. The pressure-time curve generated by this throat recession rate table is given in Figure 5.29. Reconstructed throat recession rate and diameter histories are given in Figure 5.30.

As can be observed from Figure 5.29, effect of throat recession is quite significant for this case in terms of interior ballistics, providing an excellent demonstration for the concepts discussed in Chapter 1.

The reconstructed data given in Figure 5.30 will be used as a reference for the analysis presented in proceeding sections. Previous discussion in this section has illustrated

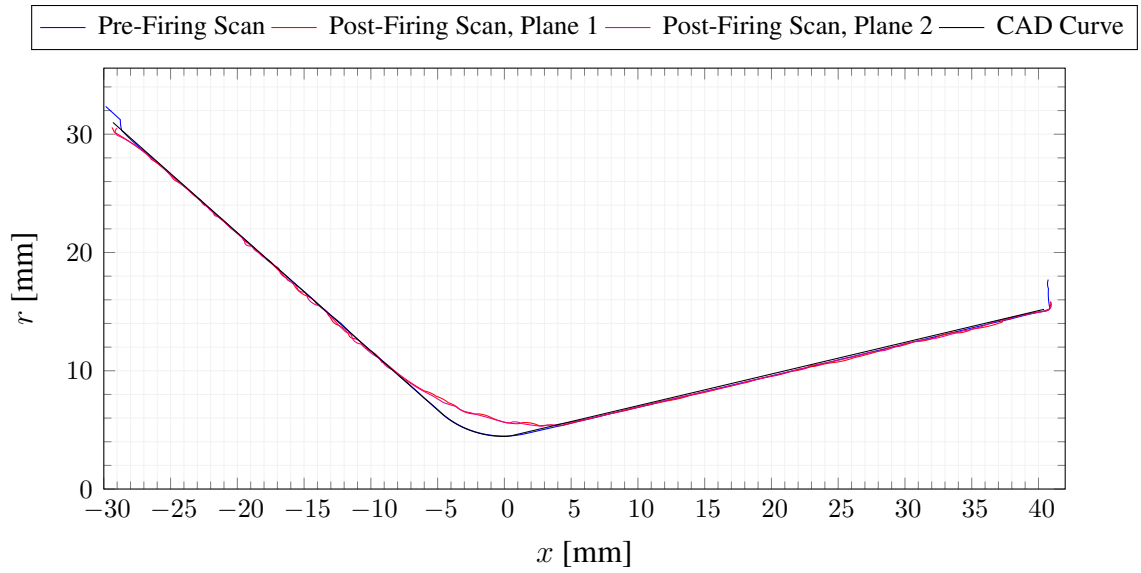

Figure 5.25: Constructed pre and post firing nozzle contours from optical scanning data along with theoretical CAD curve.

the presence of a quite large amount of uncertainty related to the employed material. Within this context, no special attempt has been carried out to inversely construct material data to produce better agreement. Instead main focus in proceeding sections is to capture the associated physical phenomena and demonstrate the differences between a simple analysis and a complex conjugate analysis.

5.3.5 Coupled Interior Ballistics Analysis with KAYMAK

Based on the findings of Section 4.3, a C_{Bartz} value of 0.7 is used for the results presented in this section. Although not significant in terms of produced pressure-time curve, the full liner thickness of 26.5 mm at the throat was specified in analysis. A grid system of 600 cells has been used with a time step size of 0.1 ms. Heat transfer coefficient was obtained with the implemented Bartz correlation, and value of λ was taken as 0.4 for blowing computations.

The resultant pressure-time curve is given in Figure 5.31. While the decay rate of chamber pressure due to throat recession has been captured within acceptable accuracy, the initiation time of ablation strongly disagrees with measurements. For SRM's with longer burn duration this transient portion might be negligible, however for this

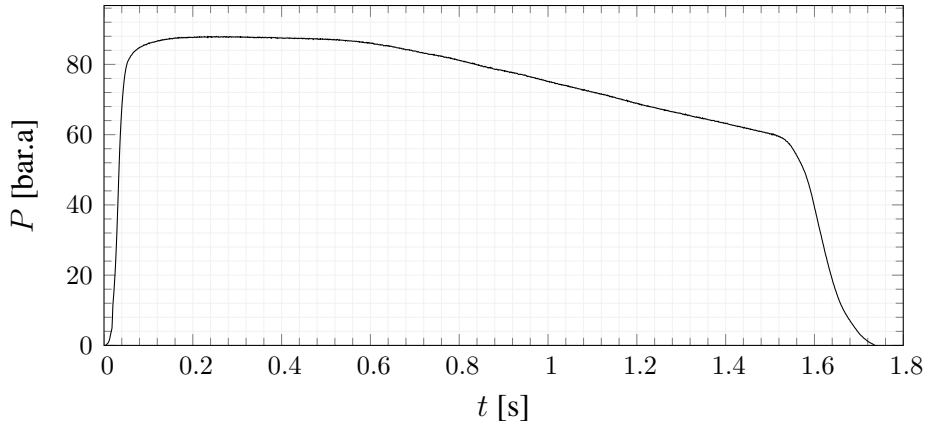

Figure 5.26: Head end pressure-time raw data.

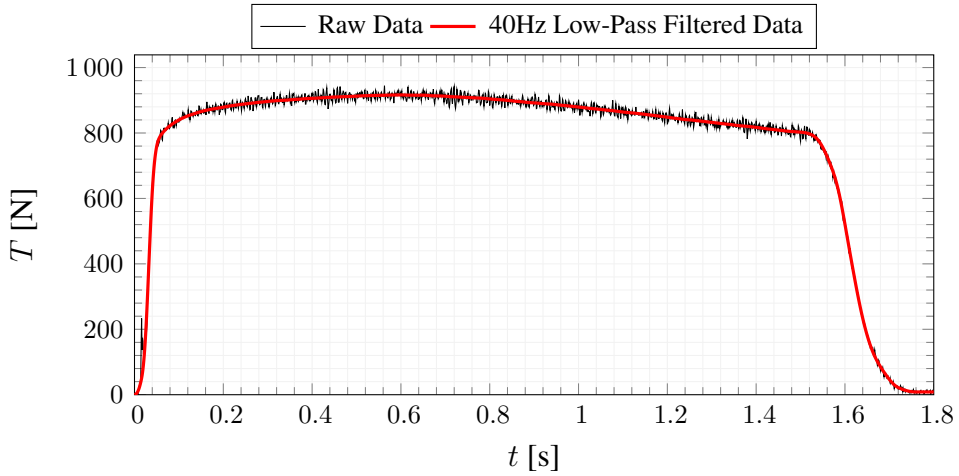

Figure 5.27: Raw and filtered thrust-time curves.

case capturing the transient is of primary importance. This is one of the expected fidelity increase from the CFD coupled analysis.

The computed throat recession rate and throat diameter history are compared to the reconstructed ones in Figure 5.32. The total recession is over predicted. However as discussed before there is a quite amount of uncertainty present in the material data, hence it is more reasonable here to compare the trends and physical phenomena instead of numbers. In that context, the decaying behavior following almost exactly the trend of pressure-time curve is not in agreement with the reconstructed values. Instead, the recession rate almost attains a steady rate about $t = 0.5$s. This is another point that is aimed to be captured in the CFD coupled analysis.

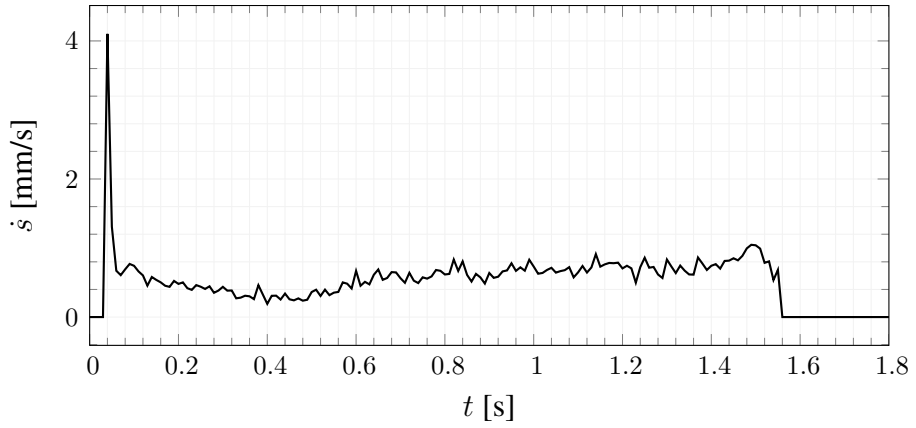

Figure 5.28: Approximate throat recession rate computed from pressure and thrust histories. Beginning and end padded with zeros.

5.3.6 Coupled Interior Ballistics Analysis with CFD Implementation

While this part consists of a relatively minor part within this work, it can be considered as the previous efforts are mainly to provide necessary inputs and verification before attempting a fully coupled CFD analysis.

As there is a great deal of uncertainty present related to the material data, no special attempt has been made here to produce exactly the same results by means of adjusting uncertain material properties, primarily char thermal conductivity, specific heat capacity, pyrolysis gas properties and emmissivities. Another point of concern is the rather large difference between the skeletal and bulk density values of the material. Instead of focusing on these uncertainties, capturing the relevant phenomena has been the main goal.

The computed pressure-time curve is given in Figure 5.33 along with measured data. Compared to the results provided in the previous section, serious improvement has been obtained. The initiation and build-up of ablation is captured much more effectively. As the discrepancy toward the end of burn duration suggests the magnitude of the recession rate is under-predicted.

Computed value of thrust is given in Figure 5.34 in comparison with measured data. Results are quite acceptable except the discrepancy present in the initial period of 0.5 s. This is most probably related to the aforementioned possible structural deformation

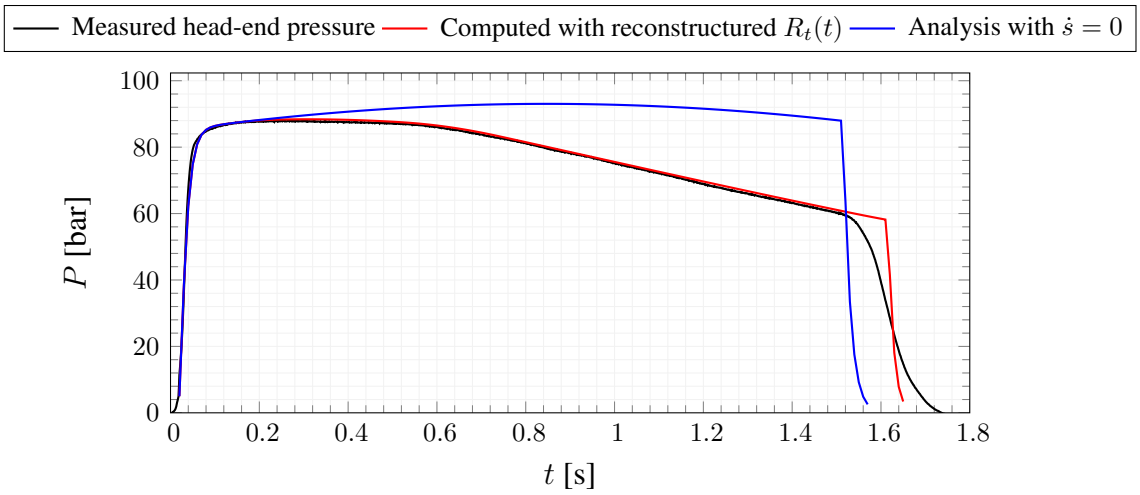

Figure 5.29: Measured head-end pressure-time curve, calculated pressure-time curve with reconstructed throat recession history and theoretical pressure-time curve for zero throat recession.

that occurred around the chamber-filling transient. Since the analysis was conducted with the adjusted throat diameter of 9.17 mm, the original geometry had to be deformed accordingly. This deformation was induced only on the throat and neighbor radius values were changed to match. The thrust coefficient efficiency of this small nozzle is very sensitive to the geometry in the vicinity of throat.

The computed valus of throat recession rate and diameter histories are given in Figure 5.35. The spikes in Figure 5.35 correspond to the instants where the physical location of throat has changed. This data was gathered by locating the point with minimum r during analysis. To illustrate this further, the history of maximum computed recession rate is also given in Figure 5.36. Note that this maximum value of recession rate occurs at slightly upstream of the physical throat location. There are three barely noticeable discontinuities present in Figure 5.36, and they correspond to the instants in which the moving average filter span has been increased from n_w =2 to n_w =4.

Much better agreement has been obtained then previous section, the initiation of ablation as well as the rate of increase of recession rate matches very well. Also the rate of throat recession attains an almost steady rate about $t = 0.5$s, which was one of the expectations from this analysis. The computed final value of throat diameter is 10.22 mm.

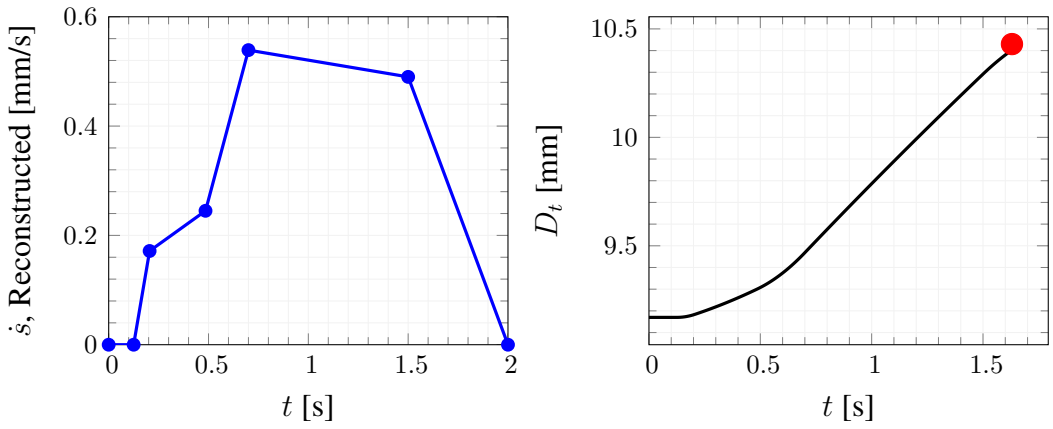

(a) Reconstructed throat recession rate.

(b) Reconstructed throat diameter history.

Figure 5.30: Reconstructed throat diameter and recession rate compared with measurements.

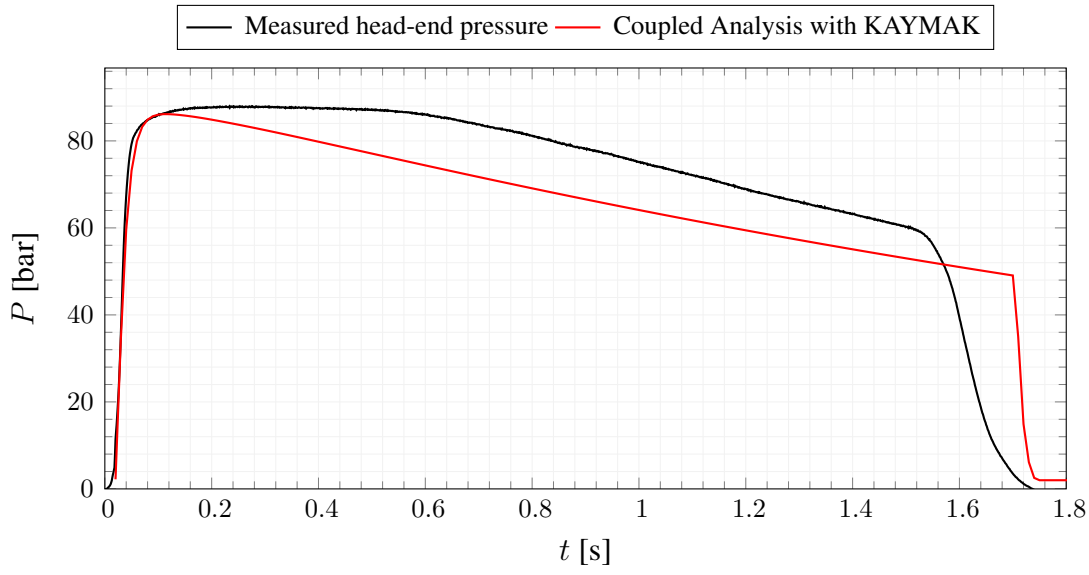

Figure 5.31: Comparison of results for head-end pressure.

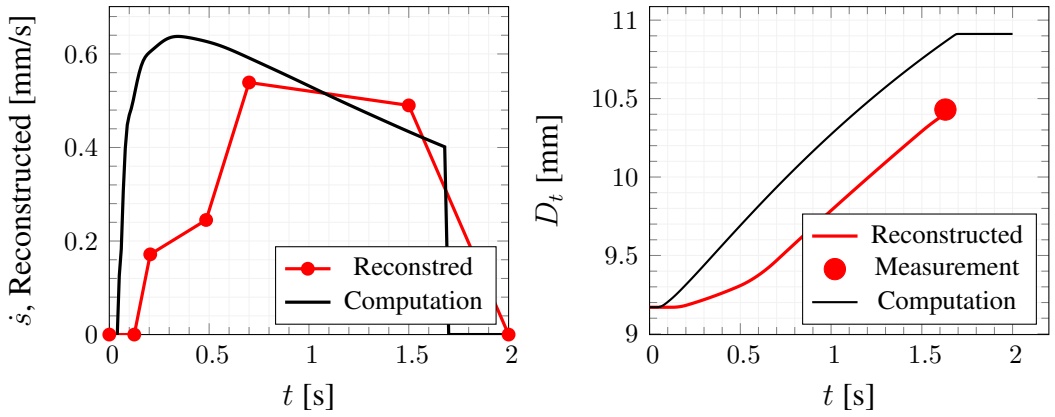

(a) Reconstructed throat recession rate.

(b) Reconstructed throat diameter history.

Figure 5.32: Reconstructed throat diameter and recession rate compared with measurements.

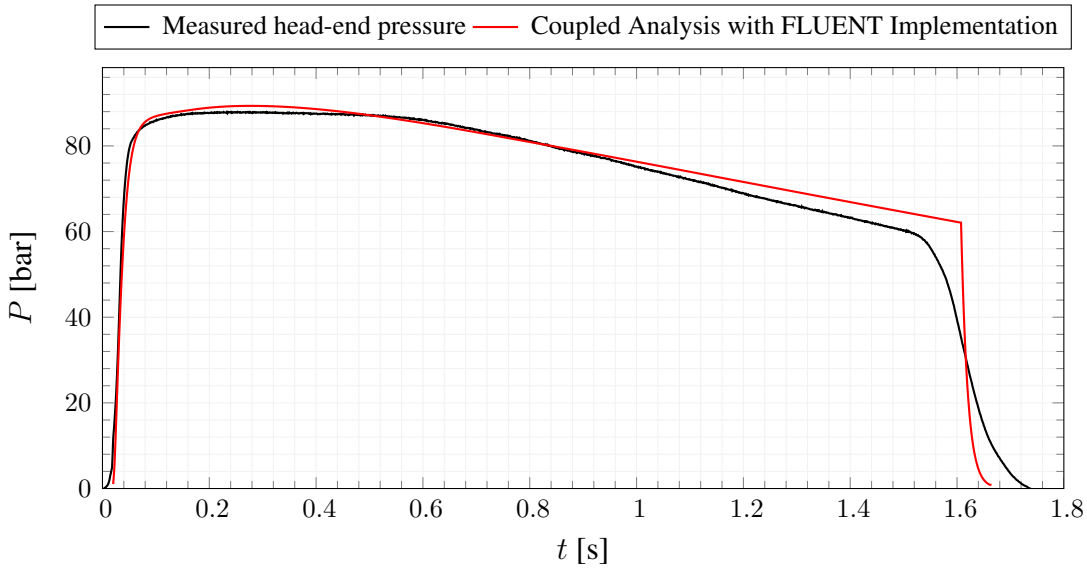

Figure 5.33: Comparison of results for head-end pressure.

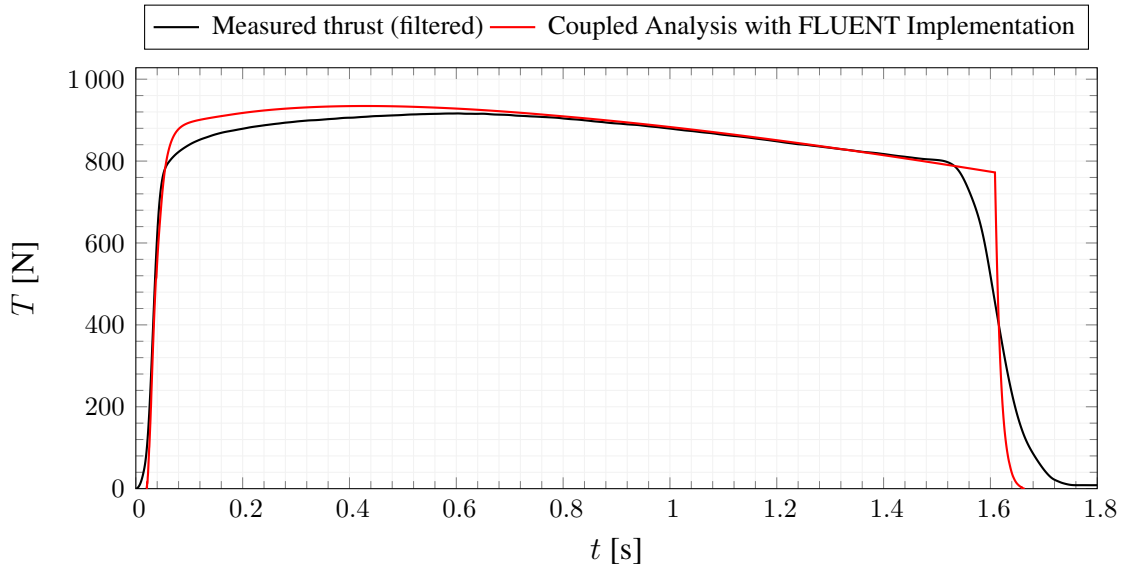

Figure 5.34: Comparison of results for thrust.

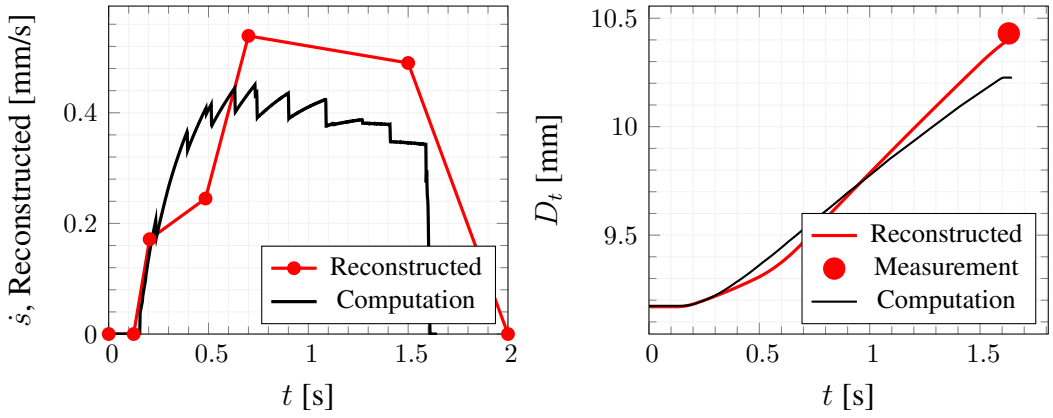

(a) Throat recession rate.

(b) Throat diameter history.

Figure 5.35: Computed throat diameter and recession rate compared with measurements.

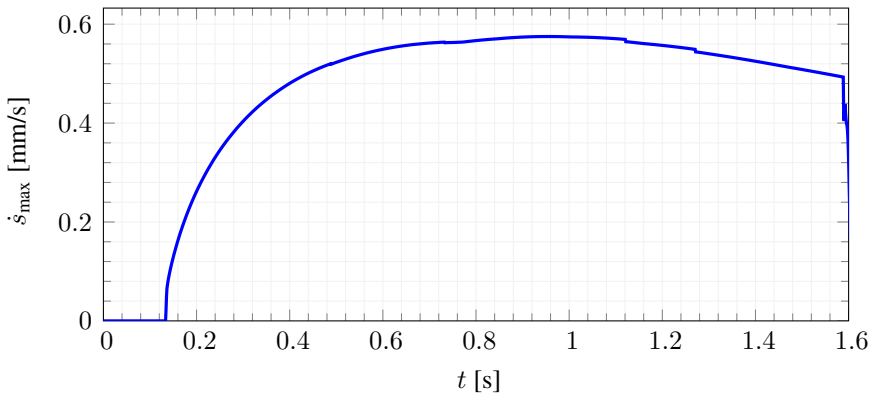

Figure 5.36: Value of maximum recession rate vs. time.

The final calculated nozzle contour compared with measured ones is given in Figure 5.37. Figure 5.38 contains the same data with emphasis on the extent of ablation. While difference in magnitudes are obvious, the extent of ablation has been captured well. As discussed in Chapter 4, the small bump about x =0.75 mm is caused by the local minima that is present in the heat flux distribution. While there are also bumps present in the measured contours, it is not possible to relate them and judge the physicality of the heat flux local minima. The bumps that are present in the measured contour are most probably due to local non-uniformities leading to uneven ablation, possible char swelling and molten material deposit.

The recession distribution along the axis of nozzle has also been computed by constructing a direction-aware minimum distance function and the results are given in Figure 5.39. It can be better here that the upstream extent of ablation has been captured very well but some discrepancy is present in the downstream portion. The negative total recession rate observed on the measured values are due to char swelling and/or deposit of molten material.

The char depth is also measured based on the color optical scanning data and results are given in Figure 5.40 in comparison with computed data. While the measurement method employed to measure the char rate is prone to uncertainties due to the inaccurate angled cut of nozzle, the trend illustrating the increase of char depth towards throat, decreasing rapidly at the regions of severe ablation is in agreement. The char depth line extracted from analysis results correspond to the iso-contour line of x =0.9.

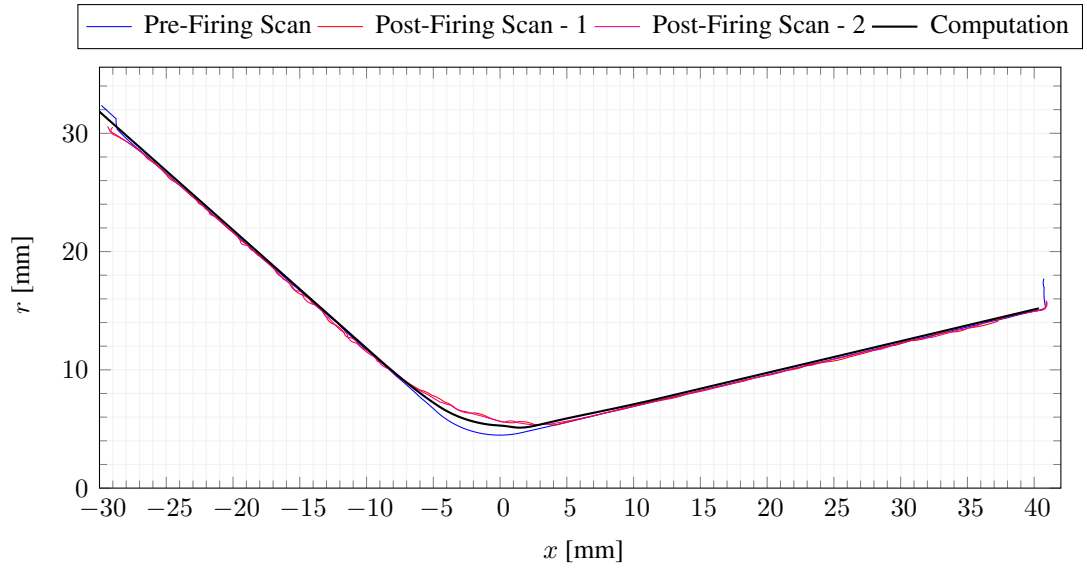

Figure 5.37: Constructed pre and post firing nozzle contours from optical scanning data along with theoretical CAD curve.

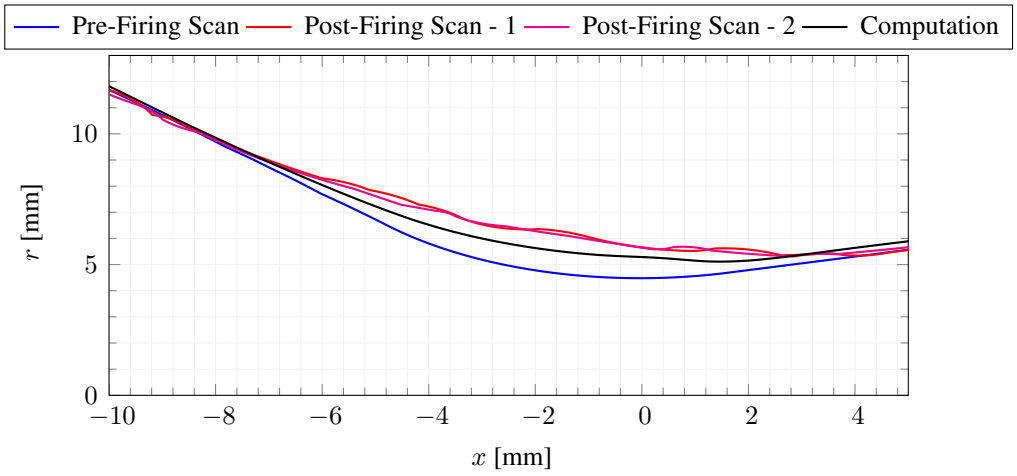

Figure 5.38: Constructed pre and post firing nozzle contours from optical scanning data along with theoretical CAD curve.

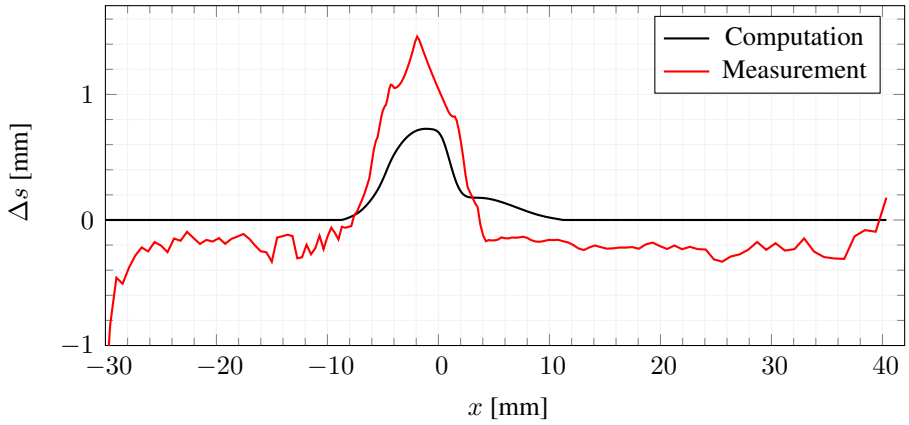

Figure 5.39: Computed axial distribution of regression compared with measurement. Negative values indicate char swelling and/or molten material deposit.

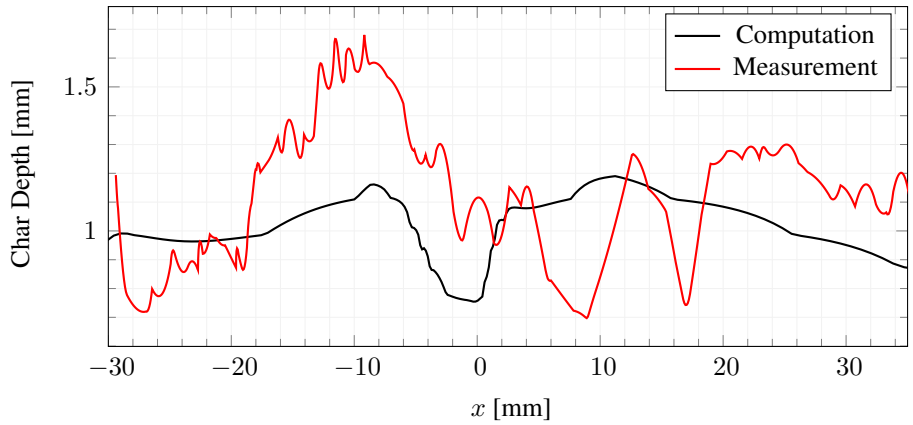

Figure 5.40: Computed axial distribution of char depth compared with measurement.

In Figure 5.41, Mach number distribution of the flowfield and degradation parameter distribution in the solid zone are given for four different evenly spaced instants. Growth and distribution of char layer is illustrated as well as the shape deformation. Another set of contour plots are given in Figure 5.42, illustrating the volumetric energy consumption rate in the decomposition zone and mass fraction of pyrolysis gas in the flowfield due to injection. In-depth progress of the reaction zone can be observed.

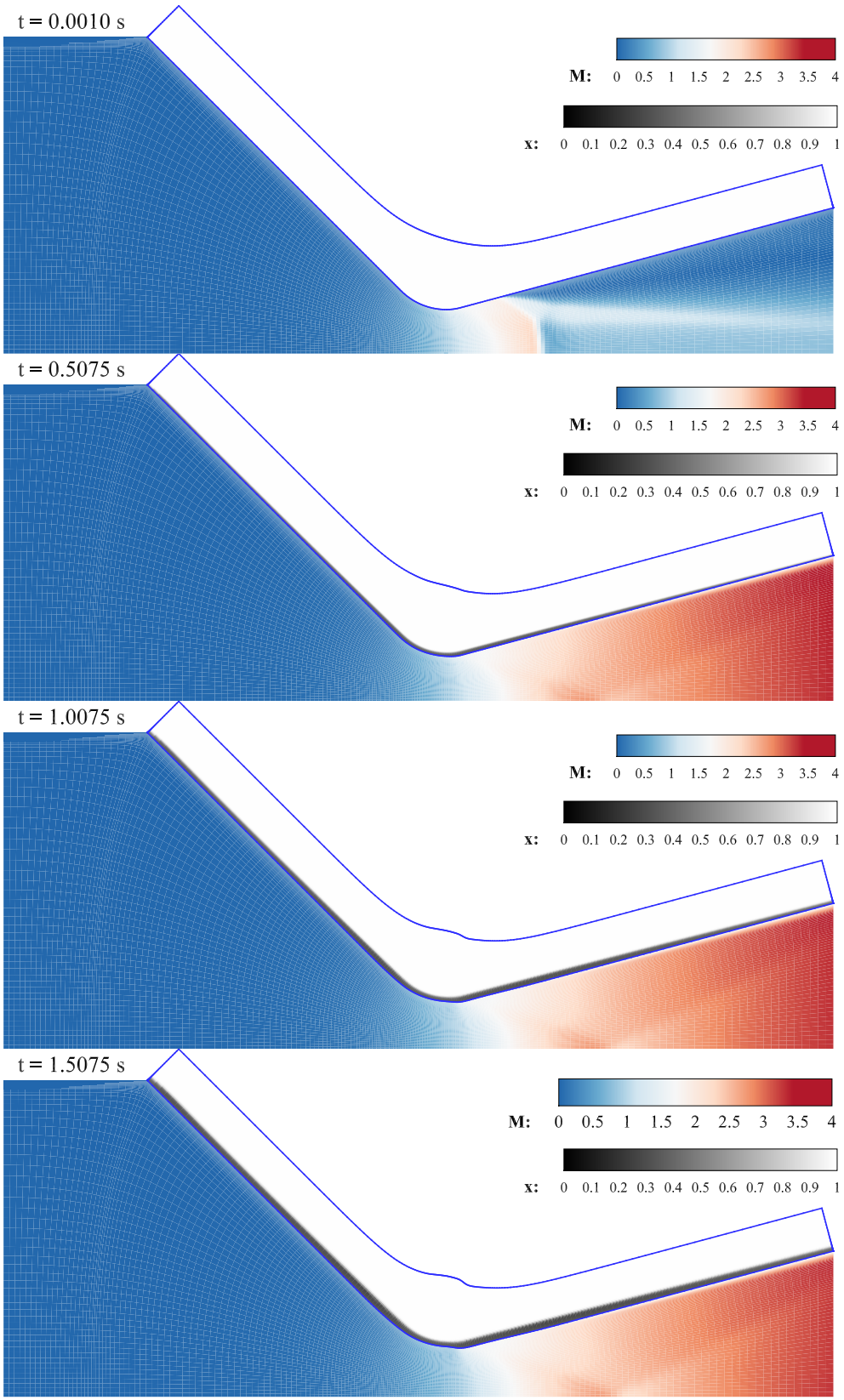

Figure 5.41: Illustration of Mach number distribution and char layer progress.

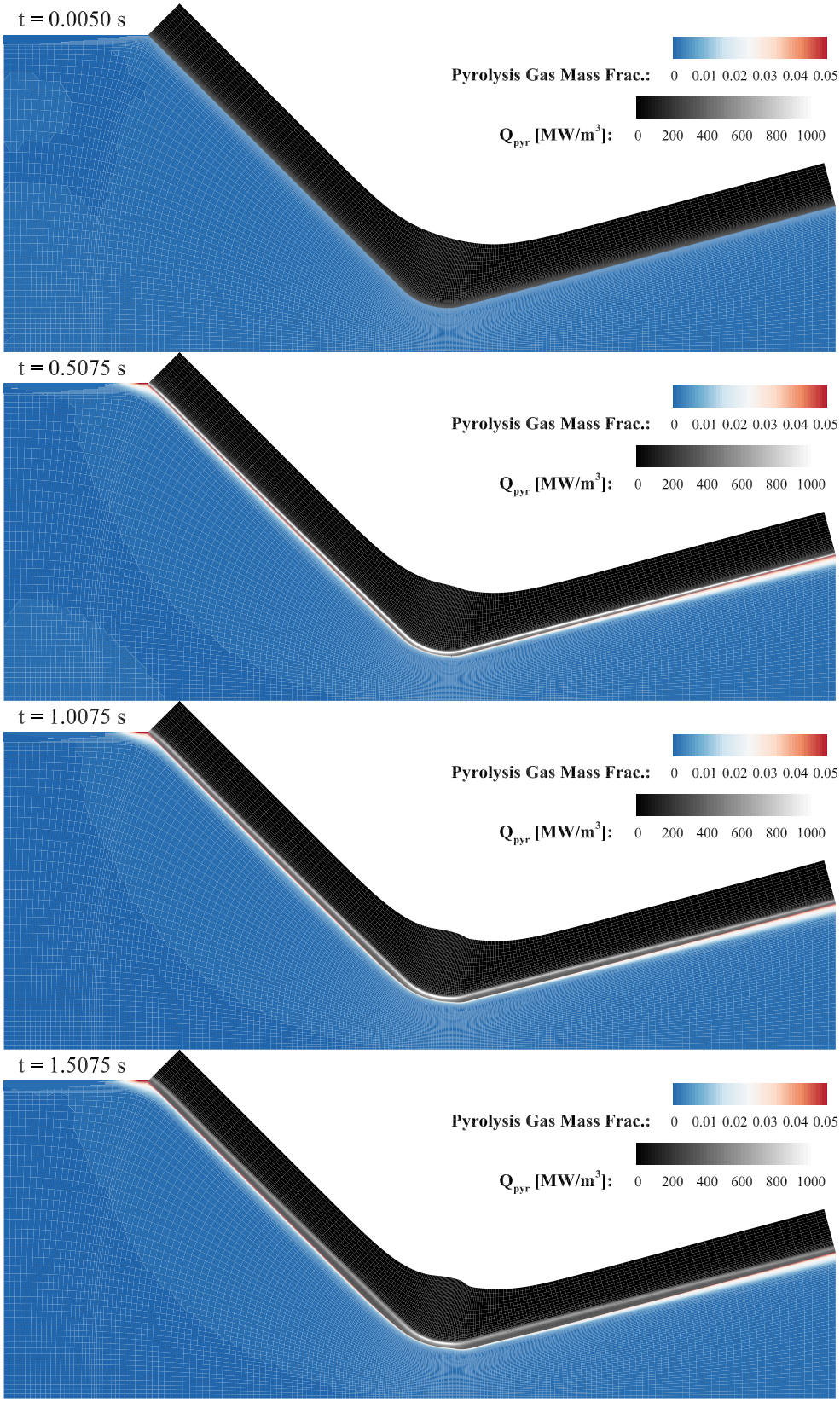

Figure 5.42: Illustration of pyrolysis gas mass fraction and decomposition zone progress.

CHAPTER 6

CONCLUSION

A detailed research regarding the analysis of charring ablators, silica-phenolic in particular, within the scope of SRM nozzles and interior ballistics is presented. Within this context, it has been demonstrated on a small scale test motor that the throat recession rate plays a vital role on interior ballistics considerations, and knowledge on this area is a great advantage during the design process.

To accomplish this task, two sets of analysis serving for different purposes are developed. While currently limited for melting ablation cases only, KAYMAK stands as a practical tool to estimate the required insulation thickness, recession rate and char depth within earlier design efforts. Another major point of usage is the inverse-estimation of certain parameters such as char thermal conductivity and emissivity based on reconstruction of test data. It is validated against literature with two very different cases.

As illustrated in Chapter 5, when it comes to capture the transient phenomena the fidelity offered by KAYMAK is clearly not sufficient. The implementation of melting charring-ablation analysis within FLUENT is comparable to state-of-art tools encountered in literature, and offers computationally affordable fully-coupled conjugate analysis possibilities. Certain investigations are carried out regarding the shape-change instability present in shape changing ablation simulations and a potential cause is proposed along with a potential elimination method. A boundary condition has been devised for the implementation of blowing within CFD environment and validated. While the lack of material characterization and uncertainty this introduces makes it impossible to assess the physical validity of the melting-ablation treatment used in this work, coupled interior ballistics simulation has illustrated that it is very

well capable of capturing most of the relevant physics involved.

Both KAYMAK and FLUENT Implementation are developed with potential future implementation of thermochemical ablation in mind to cover carbon-based material such as graphite, carbon-carbon and carbon-phenolic that are also common in SRM industry. This can be considered as a primary focus for possible future work. The usage of the developed tools are not limited to SRM analysis only. With minor modifications re-entry analysis are also possible. The lack of a porous media solution to approximate the motion of pyrolysis gas within the material can be considered as a major weakness of the current implementation and this is also a potential field of future work. This inclusion would also make it possible to remove the orthogonal structured grid limitation for the solid zone. With proper algorithms to compute nodal unit normal vectors, extension to 3D analysis is relatively straightforward. One major issue related to this point is the lack or parallelization for the current implementation, which can also be considered as a future work.

To conclude, hopefully the tools developed in this work would serve as a foundation to a tool set directed to analysis of ablation problems applicable to a wider range of materials with increased capabilities.

REFERENCES

[1] J. A. K. Riise, *Computer Code for Thermal Analysis of Rocket Motors*. Ms. thesis, NTNU, 2008.

[2] R. A. Rindal, D. T. Flood, and R. M. Kendall, "Analytical and Experimental Study of Ablation Material for Rocket Engine Application," tech. rep., VIDYA, 1966.

[3] R. A. Rindal, M. R. Wool, C. B. Moyer, and C. A. Powars, "Ablative Response of a Silica Phenolic to Simulated Liquid Propellant Rocket Engine Operating Conditions," tech. rep., Aerotherm Corporation, 1971.

[4] K. Fossumstuen, G. Raudsandmoen, and H. Wurtinger, "Design Verification Programme for an Air-to-Air Type Rocket Motor with CFRP Composite Case and Reduced Smoke Propellant," *AIAA / SAE/ASME/ASEE 29th Joint Propulsion Conference and Exhibit*, vol. AIAA 93-23, pp. 1–12, 1993.

[5] R. A. Thompson and P. A. Gnoffo, "Implementation of a Blowing Boundary Condition in the LAURA Code," *46th AIAA Aerospace Sciences Meeting and Exhibit*, vol. c, pp. 1–11, 2008.

[6] H. W. Emmons and D. C. Leigh, "Tabulation of the Blasius Function with Blowing and Suction," tech. rep., 1954.

[7] A. J. Amar, *Modeling of One-Dimensional Ablation with Porous Flow Using Finite Control Volume Procedure*. Ms. thesis, North Carolina State University, 2009.

[8] G. P. Sutton and O. Biblarz, *Rocket Propulsion Elements*. 7'th editi ed., 2001.

[9] R. L. Geisler, R. A. Frederick Jr, and M. Giarra, "Historical Overview and Solid Rocket Motor Fundamentals," *Encyclopedia of Aerospace Engineering*, pp. 1–8, 2010.

[10] J. R. Johnston, R. A. Signorelli, and J. C. Freche, "Performance of Rocket Nozzle Materials With Several Solid Propellants," *NASA Technical Notes*, p. 28, 1966.

[11] J. M. Robbins and R. W. Feist, "The China Lake Propulsion Laboratories," 1992.

[12] B. Laub, "Ablative Thermal Protection - an Overview," p. 21, 2003.

[13] G. W. Sutton, "The Initial Development of Ablation Heat Protection, An Historical Perspective," *Journal of Spacecraft and Rockets*, vol. 19, pp. 3–11, 1982.

[14] C.-L. Hsieg and J. D. Seader, "Surface Ablation of Silica-Reinforced Composites," *AIAA Journal*, vol. 11, pp. 1181–1187, aug 1973.

[15] M. Favaloro, "Ablative Materials," in *Kirk-Othmer Encyclopedia of Chemical Technology*, Hoboken, NJ, USA: John Wiley & Sons, Inc., dec 2000.

[16] L. Steg and H. Lew, "Hypersonic Ablation," tech. rep., General Electric Missile and Space Division, 1962.

[17] A. Turchi, *A Gas-Surface Interaction Model for the Numerical Study of Rocket Nozzle Flows over Pyrolyzing Ablative Materials*. Phd., Sapienza Universita Di Roma, 2011.

[18] J. W. Schaefer, T. J. Dahm, D. A. Rodriguez, J. J. Reese Jr, and M. R. Wool, "Studies of Ablative Material Performance for Solid Rocket Nozzle Applications," tech. rep., Aerotherm Corporation, 1968.

[19] R. A. Rindal, K. J. Clark, C. B. Moyer, and D. T. Flood, "Experimental and Theoretical Analysis of Ablative Material Response in a Liquid-Propellant Rocket Engine," tech. rep., Aerotherm Corporation, 1967.

[20] R. A. S. Beck, "Entry, Descent, and Landing Systems Short Course: Ablative Thermal Protection Systems Fundamentals," tech. rep., NASA Ames Research Center, California, 2013.

[21] J. A. Dec, *Three Dimensional Finite Element Ablative Thermal Response Analysis Applied To Heatshield Penetration Design*. Phd. thesis, Georgia Institute of Technology, 2010.

[22] J. Lachaud, T. E. Magin, I. Cozmuta, and N. N. Mansour, "A Short Review of Ablative Material Response Models and Simulation Tools," in *7th Aerothermodynamics Symposium*, pp. 3–11, 2011.

[23] C. B. Moyer and R. A. Rindal, "An Analysis of the Coupled Chemically Reacting Boundary Layer and Charring Ablator, Part II: Finite Difference Solution for the In-Depth Response of Charring Materials Considering Surface Chemical and Energy Balances," tech. rep., Aerotherm, 1968.

[24] R. J. Schoner, "User's Manual Aerotherm Charring Material Thermal Response and Ablation Program, Version 3," tech. rep., Aerotherm, 1970.

[25] R. M. Kendall, E. P. Bartlett, R. A. Rindal, and C. B. Moyer, "An Analysis of the Coupled Chemically Reacting Boundary Layer and Charring Ablator: Part I: Summary Report," tech. rep., Aerotherm, 1968.

[26] N. Mullenix, *Fully Coupled Model for High-Temperature Ablation and Reactive-Riemann Solver for its Solution*. Phd. thesis, University of Akron, 2010.

[27] D. R. Bartz, "A Simple Equation for Rapid Estimation of Rocket Nozzle Convective Heat Transfer Coefficients," *Journal of Jet Propulsion*, vol. 27, pp. 49–53, jan 1957.

[28] L. M. Howser and S. S. Tompkins, "Computer Program for the Transient Response of Ablating Axisymmetric Bodies Including the Effects of Shape Change," tech. rep., NASA, 1971.

[29] F. W. Matting, "Analysis of Charring Ablation with Description of Associated Computing Program," tech. rep., NASA, Washington DC, 1970.

[30] R. C. Bunker, J. F. Maw, and J. C. Vogt, "A 2-D Axisymmetric Charring and Ablation Heat Transfer Computer Code," tech. rep., Thiokol, 1985.

[31] R. E. Hogan, B. F. Blackwell, and R. J. Cochran, "Application of Moving Grid Control Volume Finite Element Method to Ablation Problems," *Journal of Thermophysics and Heat Transfer*, vol. 10, pp. 312–319, 1996.

[32] H.-K. Ahn, C. Park, and K. Sawada, "Dynamics of pyrolysis gas in charring materials ablation," in *36th AIAA Aerospace Sciences Meeting and Exhibit*, (Reston, Virigina), p. 11, American Institute of Aeronautics and Astronautics, jan 1998.

[33] T. Suzuki, K. Sawada, T. Yamada, and Y. Inatani, "Experimental and Numerical Study of Pyrolysis Gas Pressure in Ablating Test Piece," *Journal of Thermophysics and Heat Transfer*, vol. 19, pp. 266–272, 2005.

[34] J. H. Koo, D. W. H. Ho, and O. A. Ezekoye, "A Review of Numerical and Experimental Characterization of Thermal Protection Materials – Part I . Numerical Modeling," *42nd AIAA/ASME/SAE/ASEE Joint Propulsion Conference & Exibhit*, pp. 1–51, 2006.

[35] P. Baiocco and P. Bellomi, "A coupled thermo-ablative and fluid dynamic analysis for numerical application to solid propellant rockets," in *31st Thermophysics Conference*, (Reston, Virigina), American Institute of Aeronautics and Astronautics, jun 1996.

[36] D. Bianchi, E. Martelli, and M. Onofri, "Practical Navier-Stokes Computation of Flowfields with Ablation Products Injection," *European Space Agency, (Special Publication) ESA SP*, 2006.

[37] D. Bianchi, F. Nasuti, E. Martelli, and M. Onofri, "A Numerical Approach for High-Temperatures Flows over Ablating Surfaces," *39th AIAA Thermophysics Conference*, p. 11, 2007.

[38] A. J. Amar, B. F. Blackwell, and J. R. Edwards, "One-Dimensional Ablation with Pyrolysis Gas Flow Using a Full Newton ' s Method and Finite Control Volume Procedure," *39th AIAA Thermophysics Conference*, pp. 25–28, jun 2007.

[39] A. J. Amar, B. F. Blackwell, and J. R. Edwards, "One-Dimensional Ablation Using a Full Newton's Method and Finite Control Volume Procedure," *Journal of Thermophysics and Heat Transfer*, vol. 22, pp. 71–82, jan 2008.

[40] D. Bianchi, *Modeling of Ablation Phenomena in Space Applications*. Phd. thesis, University of Roma La Sapienza, 2007.

[41] D. Bianchi, F. Nasuti, and E. Martelli, "Coupled Analysis of Flow and Surface Ablation in Carbon-Carbon Rocket Nozzles," *Journal of Spacecraft and Rockets*, vol. 46, pp. 492–500, may 2009.

[42] A. F. Beerman, M. J. Lewis, R. P. Starkey, and B. Z. Cybyk, "Nonequilibrium Surface Interactions Ablation Modeling with the Fully Implicit Ablation and Thermal Response Program," *AIAA Aerospace Sciences Meeting and Exhibit*, vol. 46, pp. 1–19, 2008.

[43] A. Martin and I. D. Boyd, "Simulation of Pyrolysis Gas Within a Thermal Protection System," *40th Thermophysics Conference*, jun 2008.

[44] Y.-K. Chen, F. S. Milos, and T. Gökçen, "Validation of a Three-Dimensional Ablation and Thermal Response Simulation Code," *10th AIAA/ASME Joint Thermophysics and Heat Transfer Conference*, pp. 1–14, 2010.

[45] D. Bianchi, A. Turchi, and F. Nasuti, "Numerical Analysis of Nozzle Flows with Finite-Rate Surface Ablation and Pyrolysis-Gas Injection," *47th AIAA/ASME/SAE/ASEE Joint Propulsion Conference & Exhibit*, jul 2011.

[46] F. Nasuti and D. Bianchi, "Carbon-Carbon Nozzle Erosion and Shape-Change Effects in Full-Scale Solid-Rocket Motors," *Journal of Propulsion and Power*, vol. 28, pp. 820–830, 2012.

[47] M. E. Ewing, G. H. Richards, M. P. Iverson, and D. A. Isaac, "Ablation Modeling of a Solid Rocket Nozzle," in *5'th Ablation Workshop*, pp. 1–16, 2012.

[48] A. Ruffin, *Numerical Investigation of Nozzle Thermochemical Behaviour in Hybrid Rocket Motors*. Ms. thesis, Università di Padova, 2015.

[49] X. Chen, R. Liu, and H. Y. Du, "Erosion Study of Silica Phenolic Nozzles with Graphite Inserts in Solid Rocket Motors," *Advanced Materials Research*, vol. 1095, pp. 573–578, mar 2015.

[50] P. G. Cross and I. D. Boyd, "Two-Dimensional Modeling of Ablation and Pyrolysis with Application to Rocket Nozzles," *Journal of Spacecraft and Rockets*, pp. 0–0, oct 2016.

[51] P. G. Cross, *Conjugate Analysis of Two-Dimensional Ablation and Pyrolysis in Rocket Nozzles*. Phd. thesis, The University of Michigan, 2017.

[52] I. D. Boyd and P. G. Cross, "Conjugate Analysis of Rocket Nozzle Ablation," *47th AIAA Thermophysics Conference*, pp. 1–22, 2017.

[53] P. G. Cross and I. D. Boyd, "Conjugate Analyses of Ablation in the HIPPO Nozzle," in *2018 Joint Thermophysics and Heat Transfer Conference*, (Reston, Virginia), American Institute of Aeronautics and Astronautics, jun 2018.

[54] R. L. Potts, "Hybrid Integral/Quasi-Steady Solution of Charring Ablation," in *5th Joint Thermophysics and Heat Transfer Conference*, (Reston, Virigina), American Institute of Aeronautics and Astronautics, jun 1990.

[55] Y.-K. Chen, "Thermal Ablation Modeling for Silicate Materials," in *54th AIAA Aerospace Sciences Meeting*, (Reston, Virginia), pp. 1–25, American Institute of Aeronautics and Astronautics, jan 2016.

[56] S. Gordon and B. J. McBride, "Computer Program for Calculation of Complex Chemical Equilibrium Compositions and Applications, I. Analysis," tech. rep., NASA, 1994.

[57] B. J. McBride and S. Gordon, "Computer Program for Calculation of Complex Chemical Equilibrium Compositions and Applications II. Users Manual and Program Description," tech. rep., NASA, 1996.

[58] S. Martinelli, S. Ruffin, R. McDaniel, J. Brown, M. Wright, and D. Hash, "Validation Process for Blowing and Transpiration-Cooling in DPLR," *39th AIAA Thermophysics Conference*, p. 9, 2007.

[59] D. Cagliostro, H. Goldstein, and J. Parker, "Silica Reinforcement and Char Reactions in the Apollo Heat Shield," tech. rep.

[60] S. Deshpande, S. Pavithran, and V. Iyer, "A Finite Volume Model of Charring and Ablation," *Journal of Engineering Research and Studies*, vol. M, 2011.

[61] D. M. Smith, *A Comparison of Experimental Heat-Transfer Coefficients in a Nozzle with Analytical Predictions from Bartz's Methods for Various Combus-*

tion Chamber Pressures in a Solid Propellant Rocket Motor. Ms. thesis, North Carolina State University, 1970.

[62] J. Lachaud and N. N. Mansour, "A pyrolysis and ablation toolbox based on OpenFOAM," in *5th OpenFOAM Workshop*, pp. 1–4, NASA Ames Research Center, 2010.

[63] X.-L. Tong and E. Luke, "Turbulence Models and Heat Transfer in Nozzle Flows," *Turbulence Models and their Applications*, vol. 42, pp. 2391–2393, 2011.

[64] P. A. Gnoffo and C. O. Johnston, "A Boundary Condition Relaxation Algorithm for Strongly Coupled, Ablating Flows including Shape Change," in *42nd AIAA Thermophysics Conference*, 2011.

[65] B. W. Burrell, D. P. Crowley, M. A. DeSesa, and M. E. Ihnat, "The Post-Test Analysis of Ablative Materials," tech. rep., AVCO Government Products Group Space Systems Division, 1969.

[66] Ç. O. Alanyalıoğlu, "Simple and Accurate Method for Determination of Solid Rocket Motor Nozzle Throat History," *53rd AIAA/SAE/ASEE Joint Propulsion Conference*, pp. 1–8, 2017.